Precision cosmology with LSST : Developement of an unbiased cosmic shear estimator measured on galaxy images

Enya van den Abeele

Sorbonne Université

École doctorale n°560 : Sciences de la Terre et de l'Environnement et Physique de l'Univers de Paris (STEP'UP)

Laboratoire de Physique Nucléaire et de Hautes Énergies

Precision cosmology with LSST

Developement of an unbiased cosmic shear estimator measured on galaxy images

Présentée par **Enya Van den Abeele**

Thèse de doctorat de Cosmologie

Dirigée par **Pierre Astier**

Soutenue publiquement le 12 Septembre 2024 devant le jury composé de:

Martin Kilbinger	—	Rapporteur
Stéphanie Escoffier	—	Rapporteuse
Céline Combet	—	Examinatrice
Pierre-François Léget	—	Examinateur
Delphine Hardin	—	Présidente du jury
Pierre Astier	—	Directeur de thèse

C'est une bien faible lumière qui nous vient du ciel étoilé. Que serait, pourtant, la pensée humaine, si nous ne pouvions pas percevoir ces étoiles ?

- Jean Perrin

Acknowledgements

Ainsi s'achèvent ces trois années de thèse, à la fois riches en enseignements et en challenges, et dont le contenu scientifique est synthétisé dans ce manuscrit.

Mais une thèse ne se résume pas qu'à ses résultats, elle est aussi le fruit de l'expérience humaine qui l'accompagne, et je souhaite remercier ici toutes les personnes ayant contribué, de près ou de loin, à l'aboutissement de celle-ci.

Je souhaite en premier lieu remercier mon directeur de thèse, Pierre Astier, tout d'abord d'avoir accepté d'ouvrir ce sujet, puis d'avoir été mon mentor durant ces trois ans. Tu l'as souvent dit, ce n'était pas un sujet facile, et je suis très reconnaissante de la confiance que tu m'as accordée pour qu'on puisse l'explorer ensemble. Je te remercie pour ta disponibilité, pour les réponses à toutes (*toutes*) les questions que j'ai pu te poser, pour avoir pris au sérieux mes doutes quand j'en avais, et plus généralement pour tout le savoir que tu m'as enseigné. Je pense que l'on pourrait écrire une bibliothèque avec tout ce que j'ai appris durant cette thèse (en physique, mais aussi en histoire, en géographie, en œnologie, et bien d'autres sujets !). Merci également pour tes nombreuses relectures de ce manuscrit et les corrections que tu y as apporté. J'espère que nous pourrons continuer nos discussions à l'avenir, en cosmologie mais pas que, et aussi se retrouver sur les pistes de Moriond 2026 !

Je souhaite également remercier mon jury de thèse, dont j'ai eu la chance de pouvoir choisir chacun des membres : merci à mes deux rapporteurs, Martin Kilbinger et Stéphanie Escoffier, pour votre relecture attentive du manuscrit ainsi que pour tous vos commentaires (renforçant à la fois la clarté et la qualité de son contenu), Delphine Hardin pour avoir accepté d'être ma présidente de jury ainsi que pour ta relecture et tes conseils sur mon premier chapitre, Céline Combet pour avoir accepté d'être mon examinatrice, j'espère que nous continuerons à nous voir à l'occasion de futurs LSST-France, et pour finir Pierre-François Léget, d'abord de m'avoir proposé (avant d'accepter) d'être mon examinateur, mais aussi pour tout le reste, à savoir ton accompagnement et ton soutien sans faille depuis notre premier stage ensemble en 2018. Je suis reconnaissante d'avoir eu quelqu'un d'aussi attentif, honnête et disponible dans mon entourage durant ces trois ans, et je te remercie pour nos discussions (scientifiques ou personnelles) qui m'ont toutes beaucoup apporté. J'ai hâte de pouvoir continuer de travailler avec toi !

Ensuite, que serait le groupe weak lensing du LPNHE sans sa troisième protagoniste : Anna ! Il y a eu, de mon point de vue, un avant-après ton arrivée au labo : professionnellement, tu as été d'une grande aide dans la compréhension de mon sujet et de tous les problèmes que j'ai pu rencontrer, et je pense que Pierre peut également te remercier d'avoir été le filtre « anti-questions cons » quand je passais dans ton

bureau avant d'aller dans le sien ! Et plus personnellement, j'ai beaucoup de chance d'avoir pu échanger au quotidien avec une personne aussi gentille, drôle et encourageante. Merci d'avoir toujours trouvé les mots durant mes moments de doutes, si j'ai pu gagner en confiance en moi c'est en partie grâce à toi. J'espère que tu es prête à me voir débarquer à Grenoble, j'ai déjà très hâte de nos futures randonnées, car ce n'est que le début !

Je tiens également à remercier tout le groupe cosmo du LPNHE, qui est (objectivement) le meilleur groupe du labo. Merci à Jérémy pour tes conseils, pour nos discussions sur la thèse et l'après, mais surtout d'avoir choisi de m'embaucher pour les trois ans à venir, je pense que je ne pouvais pas mieux tomber pour mon premier post doc ! Merci à Seb pour ton aide en cette fin de thèse (qui fut aussi importante pour mon manuscrit que pour mon moral) ainsi que pour la tisane au romarin à l'OHP, merci à Nicolas et Marc pour vos visions de la vie et de la recherche, j'ai beaucoup apprécié discuter avec vous durant ces trois ans, merci à Laurent et Edo de m'accueillir (bientôt) aussi chaleureusement dans votre équipe, merci à Pauline pour ta gentillesse et tes retours toujours encourageants sur mon travail et mes présentations, merci à (anti) Pierre pour ta sympathie sans égal et pour m'avoir prêté ton bureau pendant la rédaction du manuscrit, merci à Sylvain pour ton aide dans mes problèmes de code et de transformée de Fourier, merci à Christophe sans qui je n'aurais pas pu faire cette thèse, et plus généralement merci à tous pour votre accueil chaleureux, les CROUS du mardi et les social drinks du jeudi, je suis ravie de savoir qu'on continuera à se côtoyer durant mes prochaines visites au labo !

Je souhaite aussi remercier les autres membres du LPNHE, à commencer par mon parrain Olivier, merci pour ton humour, pour tous les cafés que tu m'as payés, mais surtout pour avoir été une oreille attentive durant ma thèse, tous les futurs doctorants qui ne t'auront pas comme parrain ne savent pas ce qu'ils ratent ! Merci à Daniel pour nous avoir illuminé de ton optimisme et de ta bonne humeur depuis ton arrivée, merci à Jean-Philippe pour le template du manuscrit, et également merci aux trois piliers de l'ombre comme j'aime les appeler : Véra pour Moriond, le café, les pommades contre les piqûres d'abeilles et les photomontages incroyables, Karine pour avoir réglé tous mes problèmes informatiques, pour les encouragements durant l'écriture du manuscrit et pour les cartons qui ont sauvé mon déménagement, et Marjorie pour avoir géré toutes les missions quand personne ne comprenait rien ni à Etamine ni à Notilus, ainsi que pour m'avoir grandement aidée dans l'organisation de mon pot de thèse (en particulier dans le choix du champagne !).

Et que serait le LPNHE sans ses doctorants, à commencer par ceux de ma promo, parmi lesquels je suis heureuse d'avoir trouvé de véritables amis : Thierry (Titi), mon acolyte durant ces trois ans, à la fois au labo, en école d'été et en conférence, Guillaume (Guigui), « le petit prince de la biennale », collègue de bureau depuis 2021 mais grande découverte de l'année 2023, et Renaud (Rono), le subtile du groupe, connu pour son humour délicat, son charme et sa beauté (c'est une blague de particuliste). Merci d'avoir été là dans les hauts comme les bas, merci pour les fous-rires quasi quotidiens, merci d'avoir été les rayons de soleil de ma thèse, rien n'aurait été pareil sans vous, et j'espère suivre vos aventures encore longtemps. Merci à Leander d'avoir été une source inépuisable d'anecdotes drôles et insolites, je ne me suis jamais ennuyée avec toi, surtout quand tu servais l'eau au CROUS ou que tu préparais ton « gratuit », merci à Slava pour nos discussions sur les mangas, la politique, la linguistique et pour avoir agrandi ma bibliothèque de memes, merci à Tommaso pour ta joie de vivre et ta créativité lorsque tu racontes des histoires (surtout celle du trafic de sel à New York). Évidemment merci Artur d'avoir été une épaule et une oreille pendant cette thèse (vu que les miennes sont toutes petites...), mais j'aurai l'occasion d'en dire plus après. Merci à tous les autres doctorants et post-doctorants : Marion, Claire, Laura, Ugo, Line, Anaëlle, Paul, Dylan, Aloïs, Fotis, Pablo, Arsène, Lavinia, Romain, Ulysse, Claudia, Mahmoud, Yassine,

William, pour les bons moments partagés au bureau, au CROUS, à la cafet ou à la Bulle à Bière, et aussi aux anciens qui ont quitté le labo avant nous, je pense à Ariel, Viet, Georgios, Ting, Louis, Romain, Sara, Mykola, Vlada et Valentina. Un merci tout particulier à Julianna, la toute première doctorante que j'ai rencontrée, j'ai adoré partager mon bureau pendant un an avec toi, mais surtout je te remercie d'être devenue une fabuleuse amie avec qui tout est facile. En attendant de voir ce que l'avenir nous réserve, il nous reste beaucoup de brunchs et d'ateliers poterie à faire ensemble !

Je tiens à remercier tous mes amis, à commencer par la bande de joyeux lurons du M1 de Jussieu : Rayan, Gabriel, Artur (encore), Louise, Angelo, Timothée[2], Laura, Clément, JB, Dario, Hippolyte, Alex, Etienne, Lamya, Sanjay, Marie, et tous ceux rencontrés grâce à eux, en particulier Élodie, Tom et Laurine: quelle joie de vous avoir dans ma vie depuis plusieurs années déjà, d'avoir partagé l'expérience de la thèse avec certains d'entre vous (mais aussi des jeux *très* stupides *très* souvent au bar), et surtout de savoir que je peux compter sur chacun d'entre vous. Un merci spécial aux Harmoniques Sphériques, en particulier Timothée, Artur (toujours lui !) et Adrien pour m'avoir proposé de vous rejoindre, de m'avoir encouragée quand j'en avais besoin et d'avoir donné une autre dimension à ma dernière année de thèse. C'est une vraie chance de pouvoir jouer dans un groupe avec des gens qu'on apprécie autant, et j'espère qu'on deviendra tous des rock stars un jour.
Merci à mes amis du M2 AAIS : Emma, Alex, Nathan, Romain, Gaël, Paul, Maza, Lucas, Thomas, Corentin, heureusement que le Covid n'a pas eu raison de notre promo ! Merci pour toutes ces soirées passées ensemble et les nombreux débriefs sur nos thèses respectives, ça fait du bien de partager cette aventure avec des personnes dans le même bateau que nous !
Merci à mes copains d'école d'été : Madeleine, Chloé, Justine, Mathilde, Tristan, Raphaël, Tamara, avec qui j'ai bien ri à Euclid, à Cargèse, à Moriond et en dehors !
Merci à mes amis de CurieOsity, en particulier Mariette, avec qui j'ai vu grandir l'asso ces dernières années, et qu'on laisse maintenant entre de bonnes mains.
Merci aux « chimistes », qui me suivent depuis huit ans déjà : Pierre, Charlène, Mikaël, Anthony, Andrej, quand je repense à notre L1 j'ai l'impression que c'était hier. J'espère qu'on continuera à suivre nos évolutions pendant encore plusieurs années, avec au moins un check-up raclette annuel !
Merci à mes amis de plus longue date encore, qui sont toujours là malgré le temps qui passe : Sarah, Yanis, Valentin, Charlotte, votre présence m'est précieuse.

Merci à ma marraine, Valérie, pour avoir suivi mon évolution et m'avoir encouragée durant ces trois (que dis-je, ces vingt-six !) dernières années.

Enfin, merci à mes parents, sans qui je ne serais certainement pas là aujourd'hui. Merci Papa de m'avoir donné l'envie de tout comprendre et de tout remettre en question, c'est sans aucun doute ton goût pour les questions philosophiques et métaphysiques qui m'a amenée à la cosmologie. Merci Maman pour avoir donné un point de départ à mon aventure au LPNHE en m'incitant à aller à cette fête de la science 2018, et d'avoir remis mes pendules à l'heure pendant mes crises de syndrome de l'imposteur. Merci à tous les deux d'avoir toujours cru en moi, de m'avoir soutenue, et de continuer à le faire quelles que soient les directions dans lesquelles je décide de m'engager. Je pense que l'Univers n'aurait pas pu conspirer tout seul sans vous.

List of Figures

List of Tables

Résumé substantiel

Après les années 50, nombreuses sont les découvertes ayant façonné la cosmologie d'aujourd'hui. Parmi elles, on peut noter la découverte de la matière noire dans les années 70, puis celle de l'énergie noire en 1998, la compréhension de cette dernière étant la motivation de ce sujet de thèse. De ces observations résulte le modèle faisant pour l'instant consensus chez les cosmologistes : ΛCDM.

Afin de tester le modèle ΛCDM, et notamment de contraindre l'énergie noire, plusieurs sondes existent. L'une d'entre elles est l'effet de lentille gravitationnelle faible. Cet effet est un résultat direct de la relativité générale : l'espace et le temps sont liés en un seul ensemble, dit « espace-temps », dont la géométrie se voit distordue en présence de masse. Du point de vue d'un observateur, les sources d'arrière plan sur la ligne de visée apparaissent tordues à cause des distorsions de l'espace-temps provoquées par des objets massifs en avant plan (lentilles), les photons suivant la courbure. Cet effet peut être très fort et observable directement sur des images (*strong lensing*), ou plus faible et nécessitant une détection statistique. C'est ce deuxième régime, le *weak lensing*, qui nous intéresse. L'une des mesures du *weak lensing* est le *cosmic shear*, résultat de la distorsion de galaxies d'arrière plan par les structures à grande échelle. La mesure du *cosmic shear* permet de cartographier la distribution de toute la matière (en incluant la matière noire), et étudier cette distribution à plusieurs échelles de distances permet de de remonter à l'influence de l'énergie noire sur la répartition de la matière au cours du temps. Une telle analyse se fait en mesurant les fonctions de corrélations à deux points du *cosmic shear* dans différentes tranches de redshift (analyse tomographique), ces fonctions de corrélation étant directement reliées aux paramètres cosmologiques du modèle ΛCDM. Un historique des découvertes associées au *lensing* ainsi que son formalisme mathématique sont développés dans le Chapitre 2.

Ces dernières (et prochaines) années marquent un tournant pour la cosmologie : la construction de relevés de nouvelle génération tels qu'EUCLID et le Vera Rubin Observatory (anciennement LSST), cartographiant le ciel avec une couverture et une profondeur inégalées, ouvre la voie à l'ère de la cosmologie de précision. En particulier, le Vera Rubin Observatory est le premier télescope au sol conçu pour mesurer le *weak lensing*, ce qui en fera sa sonde la plus précise pour contraindre

les paramètres de l'équation d'état de l'énergie noire. Avec son miroir de 8.4m et sa caméra de 3200 mégapixels, on attend plusieurs milliards de galaxies observées à la fin du relevé. Cependant, malgré le design optique innovant et la statistique sans précédent de LSST, la mesure du *shear* est sujette à de nombreuses sources d'effets systématiques. Parmi elles, on retrouve les effets instrumentaux, la turbulence atmosphérique, les effets de sélection et de détection, la calibration de l'estimateur du *shear* ou encore le bruit de grenaille. Tous ces effets sont sources de biais à la fois multiplicatif et additif dans la mesure du *shear*, il est donc important de pouvoir contrôler leur valeur, tout en tenant compte de la statistique attendue du détecteur. Dans le cas de LSST, l'objectif est d'atteindre une limite de 10^{-3} sur la valeur du biais multiplicatif, et 10^{-4} pour le biais additif. L'ensemble des challenges autour de la mesure du *shear*, les sources de biais pouvant affecter sa mesure, ainsi qu'une description plus détaillée du télescope LSST sont développés dans le Chapitre 3.

Parmi les sources d'effets systématiques dans la mesure du *shear*, nous avons cité la méthode d'estimation de ce dernier. De nombreux estimateurs ont vu le jour depuis les années 90, mais aucun n'a fait l'objet d'un consensus dans la communauté.
Le développement de telles méthodes d'estimations se décline en plusieurs étapes : d'abord, la mesure des formes des objets observés (dans notre cas l'ellipticité des galaxies), puis la calibration de ces formes. Les ellipticités ne permettent pas à elles seules d'estimer le *shear* à cause des effets atmosphériques et instrumentaux venant s'ajouter aux images (décrits à travers la PSF), biaisant ainsi les mesures. Il existe différentes manières de déterminer les formes des sources : le *model fitting*, où un modèle de galaxie est ajusté par comparaison aux observations et minimisation des moindres carrés, et les méthodes basées sur les seconds moments, où la forme est directement mesurée sur l'image. Concernant la calibration, les procédures sont également variées, allant des simulations aux méthodes perturbatives. L'objet principal de cette thèse est le développement d'une nouvelle méthode d'estimation de *shear*, comportant des avantages notables par rapport aux méthodes de pointes déjà existantes. La mesure de forme se base sur les seconds moments, avantageux comparés au *model fitting* car aucune hypothèse n'est faite sur le profil des galaxies. La mesure des seconds moments renvoie directement à l'ellipticité observée de la galaxie, dite $\mathbf{e}$. La calibration de cette ellipticité est réalisée par une méthode perturbative où des variations de *shear* artificielles sont appliquées aux images. Une autre force de cette méthode réside dans le fait que ces variations ne sont pas apliquées à l'image originale, mais aux autres termes de l'estimateur, plus étendus et mieux résolus. À partir des seconds moments de ces images perturbées sont calculées les dérivées numériques de l'ellipticité par rapport au *shear*, permettant de définir le facteur d'auto-calibration $\mathbf{R}$. Les détails d'implémentation de cette méthode sont développés dans le Chapitre 4.

Ce nouvel estimateur a ensuite été testé sur des simulations - sans bruit -, où nous avons varié à la fois les profils de galaxies et de PSF, le tout à des ratios de tailles réalistes. Les profils de galaxies varient entre gaussiennes, profils composites avec bulbe et disque, et images issues d'un catalogue du télescope Hubble (*COSMOS*). Quelques soient les combinaisons, les estimations de *shear* montrent toujours un biais multiplicatif de l'ordre de 10^{-3}.

Les résultats de ces estimations sont disponibles dans le Chapitre 5.

On peut maintenant se poser la question : que se passe-t-il lorsque du bruit est ajouté dans l'image ? Le bruit de grenaille, causé par la variabilité de la détection des photons sur un senseur, est source d'effets systématiques dans la mesure de forme des objets, et donc fatalement dans celle du *shear*. En effet, la mesure de la position des objets est bruitée de façon corrélée avec l'ellipticité de la galaxie et le rapport signal sur bruit (SNR). Toutes les méthodes d'estimations de formes étant des fonctions non-linéaires de la position, le fait que la mesure de cette dernière soit bruitée introduit donc un biais (dit *noise bias*) dans l'estimateur. De nombreuses méthodes de correction des effets systématiques causés par le bruit ont été proposées durant les dernières décennies, comportant chacune leurs limitations. La procédure la plus courante est de calibrer ce biais à l'aide de simulations, qui comporte certains inconvénients : difficultés à séparer les variables dont le *noise bias* dépend (formes des galaxies et SNR), hypothèses limitantes sur les profils choisis pour créer les images, ou encore le temps de calcul souvent colossal pour réaliser les boucles sur ces simulations (pour avoir un biais contrôlé à 10^{-3}, il est nécessaire de réaliser des estimations sur des millions d'événements).
Dans ce contexte, le développement d'une correction du *noise bias* dépendant uniquement des propriétés des images serait très avantageux. La piste explorée dans ce manuscrit est celle de calculer la prédiction du *noise bias* de façon analytique à partir des dérivées secondes de l'expansion de Taylor de l'estimateur de formes des galaxies. Au delà de ses avantages computationnels, une telle méthode permet également de s'affranchir de toute hypothèse faite sur les profils des galaxies. En développant cette méthode, nous avons déterminé une formule analytique de la variance de la mesure de la position compatible avec la variance numérique calculée à partir de simulations. Il en est de même pour le biais du flux et de l'ellipticité $\mathbf{e}$ des galaxies. Concernant le facteur d'auto-calibration $\mathbf{R}$, la détermination d'une formule analytique du *noise bias* s'avère plus complexe, les seconds moments et le flux étant corrélés après l'introduction des variations de *shear* dans l'estimateur pour calculer les dérivées. Le développement de cette correction analytique et les perspectives envisagées pour son amélioration sont décrits dans le Chapitre 6.

Contents

Résumé

La découverte de l'accélération de l'expansion de l'Univers en 1998 bouleversa notre vision des phénomènes physiques qui gouvernent son évolution. La cause de cette accélération s'opposant à l'action attendue de la gravité est nommée « énergie noire » par les cosmologistes, et son origine reste encore aujourd'hui indéterminée. Plusieurs sondes cosmologiques permettent de contraindre l'énergie noire, notamment le cisaillement gravitationnel (*cosmic shear*), résultat d'un effet de lentille gravitationnelle faible sur des galaxies d'arrière plan causé par les structures à grande échelle. Sensible à la fois à la distribution de matière et à la géométrie de l'Univers, il est possible d'en faire un outil puissant pour contraindre l'équation d'état de l'énergie noire. La prochaine décennie marque l'entrée dans l'ère de la cosmologie de précision avec le développement de relevés de nouvelle génération tels que LSST. Ce télescope du Vera C. Rubin Observatory est le premier relevé au sol conçu pour les analyses de lentilles gravitationnelles faibles, notamment grâce à sa caméra de 3200 megapixels et son miroir primaire de 8 mètres, qui permettront d'imager le ciel avec à la fois une profondeur et une couverture spatiale inégalées. Au bout de 10 ans, LSST aura observé plusieurs milliards de galaxies, permettant ainsi de réaliser des mesures cosmologiques sans précédent, particulièrement avec le *cosmic shear* qui nécessite une détection statistique sur un grand nombre de sources. Cependant, la mesure du *shear* est quelque chose de complexe et associée à de nombreuses sources de systématiques, parmi lesquelles on retrouve la calibration de l'estimateur de formes des galaxies, ou le bruit de grenaille dans les images. En considérant la statistique prévue d'LSST, les différentes sources d'erreurs systématiques doivent être contrôlées au pour-mille afin d'atteindre la précision souhaitée sur l'équation d'état de l'énergie noire. C'est dans ce contexte que s'inscrivent les résultats présentés dans cette thèse. La première partie de ce travail a été de développer un estimateur non biaisé du cisaillement gravitationnel directement à partir des images de galaxies. Les avantages de cette nouvelle méthode sont multiples en comparaison aux méthodes de pointe comme Metacalibration (aujourd'hui état de l'art dans la mesure du *shear* sur des galaxies) : aucune hypothèse n'est faite sur le profil des sources (la mesure de forme se faisant à partir des seconds moments de la distribution de lumière) et aucune distorsion n'est appliquée à l'image de la galaxie, permettant à la fois d'éviter l'introduction de bruit corrélé dans les estimations ainsi que de réaliser des mesures de *shear* sur des images sous échantillonnées. La deuxième partie de ce travail s'articule autour de la correction du *noise bias*, causé par le bruit de grenaille dans les images. Le bruit introduisant un biais dans la mesure de forme, il biaise également les estimations de *shear*. Les méthodes usuelles de calibration de ce biais se faisant sur des simulations, elles sont sujettes à certaines limites, notamment les hypothèses choisies pour la modélisation des images ou le conséquent temps de calcul nécessaire à la réalisation de boucles Monte Carlo. Pour contourner ces limitations, nous nous sommes penchés sur le développement d'une correction analytique du *noise bias* à travers le calcul des dérivées du second ordre de l'estimateur de forme. Cette méthode donne des résultats très satisfaisants sur la correction de l'ellipticité des galaxies, ainsi que des résultats prometteurs sur la calibration du *shear*, nécessitant de plus amples investigations.

Abstract

The discovery of the accelerating expansion of the universe in 1998 turned our vision of the physical phenomena governing its evolution on its head. The cause of this acceleration, which opposes the expected action of gravity, is called "dark energy" by cosmologists, and its origin remains undetermined to this day. Several cosmological probes can be used to constrain dark energy, including cosmic shear, the result of a weak gravitational lensing effect on background galaxies caused by large-scale structures. Sensitive to both the matter distribution and the geometry of the Universe, it can be used as a powerful tool to constrain the equation of state for dark energy. The next decade marks the dawn of the era of precision cosmology, with the development of next-generation surveys such as LSST. This telescope at the Vera C. Rubin Observatory is the first ground-based survey designed for weak gravitational lensing analyses, thanks in particular to its 3200 megapixel camera and 8-meter primary mirror, which will image the sky with both unrivalled depth and spatial coverage. After 10 years, LSST will have observed several billion galaxies, enabling unprecedented cosmological measurements to be made, particularly with cosmic shear, which requires statistical detection on a large number of sources. However, shear measurement is complex and associated with many sources of systematics, including calibration of the galaxy shape estimator, and shot noise in the images. Considering LSST's expected statistics, the various sources of systematic error need to be controlled to the per mil level in order to achieve the desired accuracy on the dark energy equation of state. This is the background to the results presented in this thesis. The first part of this work was to develop an unbiased estimator of gravitational shear directly from galaxy images. The advantages of this new method compared with state-of-the-art methods such as Metacalibration are manifold: no assumptions are made about the source profile (the shape measurement is based on the second moments of the light distribution) and no distortion is applied to the galaxy image, making it possible both to avoid introducing correlated noise into the estimations and to perform shear measurements on undersampled images. The second part of this work focuses on the correction of noise bias, caused by shot noise in the images. Noise introduces a bias in the shape measurement, and therefore also biases the shear estimations. As the usual methods for calibrating this bias are based on simulations, they are subject to certain limitations, notably the assumptions chosen for image modelling or the consequent computation time required to carry out Monte Carlo loops. To overcome these limitations, we have turned our attention to developing an analytical correction for noise bias by calculating the second-order derivatives of the shape estimator. This method gives very satisfactory results for galaxy ellipticity correction, as well as promising results for shear calibration, but requires further investigation.

Preamble

Humans' questions about their place in the universe and the nature of the cosmos date back to ancient times. In Mesopotamia, the cosmos was represented as a flat earth resting on primordial waters, while the sky was solid and supported by mountains. The Egyptians imagined the sky as the goddess Nut, resting on Geb, god of the Earth. The sun was represented by the god Ra, crossing the sky by day and the underworld by night.
The concept of a spherical cosmos was first introduced by Pythagoras (6th century BC), with the Earth (also spherical !) at its center. Subsequently, Aristotle (350 BC) proposed a geocentric cosmic model in which the celestial bodies are represented by spheres moving circularly and concentrically around the Earth, itself immobile. The hypothesis of a heliocentric universe was first formulated by Aristarchus of Samos (280 BC). Still, this theory didn't gain ground until much later, in 1543, with Nicolaus Copernicus, who proposed a model including the Earth and all the planets known at the time. Hybrid models were also proposed at the same time, such as that of Tycho Brahe who, at the same time as Copernicus, proposed a model in which the planets revolved around the Sun, and the Sun around the Earth.

In 1609, Johannes Kepler published a new formalism describing the motions of the planets, which showed that their orbits were no longer circular but elliptical. Kepler also posed the following paradox (taken up by Heinrich Olbers in 1826): why is the sky black at night ? If the universe is static, homogeneous and infinite in time and space, our gaze should always rest on a star (no matter how distant), and the night sky should therefore be extremely luminous. It was only much later, in the 20th century, that this paradox was answered, when it was demonstrated that the universe was in fact dynamic and of finite age.

The law of universal gravitation formulated by Isaac Newton in 1687 made it possible to explain and predict the movements of celestial bodies. Newtonian mechanics held sway for a long time, until other theories were added at the end of the 19th century: James Maxwell's equations for electromagnetic waves suggested that the speed of light depended solely on the electrical and magnetic properties of the medium in which it propagated, and not on the reference frame of observation, as was thought at the time with Galilean transformations. In order to reconcile Maxwell's calculations with Newtonian mechanics, the hypothesis of a medium for light propagation was put forward: the *ether*. An experiment conducted by Albert Michelson and Edward Morley in 1887 to demonstrate the existence of this ether proved inconclusive. Hendrik Lorentz and Henri Poincaré subsequently laid the foundations of special

relativity by publishing calculations explaining the transformations between two observers in different reference frames. On this basis, Albert Einstein published a paper detailing his vision of special relativity in 1905: the laws of physics are the same for all inertial observers, the speed of light is constant in vacuum and independent of reference frame, and the notion of ether is no longer necessary.
Ten years later, in 1915, Einstein published his theory of general relativity, in which gravitation is no longer described by a force but by a curvature of space-time in the presence of matter or energy. This theory complements Newtonian mechanics, which alone cannot explain all the phenomena observed in the universe, including Mercury's perihelion advance. At the same time, he described the universe as finite, static, homogeneous and isotropic. Modern cosmology is emerging as a separate branch of physics: it is the science that aims to study the origins, structure and evolution of the universe.

Thereafter, one discovery followed another, starting with the expansion of the universe revealed by Edwin Hubble's observations in 1929, demonstrating the relationship between the speed of "nebulae" and the redshift of their spectra. The nature of these nebulae, and whether or not they belonged to our galaxy, gave rise to the "Great Debate" of the 1920s, which ended in 1924 with Hubble's observations of variable stars and Cepheids within these nebulae. By measuring the distance of these objects, he was able to prove their extra-galactic nature, thus advancing our understanding and vision of the universe beyond the Milky Way.
Another major observation came in 1965: the discovery of the Cosmic Microwave Background by Arno Penzias and Robert Wilson, predicted in 1948 by Ralph Alpher and George Gamow. The expansion of the universe and the discovery of this cosmological background were among the observations that led to the development of the Big Bang theory, originally proposed by George Lemaître in 1927.

Two other major discoveries added to cosmologists' concerns: dark matter and dark energy. The former was first introduced by Fritz Zwicky in 1933, following an anomaly observed in the measurement of the total mass of the Coma cluster. It was then confirmed by other observations, notably those of Vera Rubin in 1973, showing a "missing mass" in the arms of spiral galaxies, whose rotational velocity remains constant with distance from the galaxy center instead of decreasing.
The second followed the observation of the accelerating expansion of the universe in 1998 by Saul Perlmutter, Adam Riess and Brian Schmidt. Even though the expansion had been discovered 70 years earlier, it was bound to slow down (or even reverse) due to the gravitational attraction of all bodies in the universe. The contradictory result in 1998 gave rise to the concept of "dark energy" to represent the phenomenon at the origin of acceleration, opposing gravity.

Cosmological observations tend to show that dark matter and dark energy represent respectively 25% and 70% of the composition of the universe today, and in either case, their origin is still undetermined. The result of these discoveries is the cosmological model that is the community's consensus so far: the ΛCDM model. This model provides a coherent explanation for both small and large scale observations in the universe, with just six free parameters. The theory of general relativity, the expansion of the universe, dark energy and the ΛCDM model are described in Chapter 1.

There are several probes for testing the ΛCDM model and constraining dark energy, one of which is the weak gravitational lensing effect. This effect occurs when massive objects distort space-time, causing apparent distortion of background sources. Cosmic shear, one of the measures of weak lensing, enables us to study the distortion of background galaxies by large-scale structures. This makes it possible to map all matter, and to understand the influence of dark energy on the evolution of this distribution over time. A history of the discoveries associated with lensing and its mathematical formalism are developed in Chapter 2.

The arrival of new-generation surveys such as EUCLID and LSST marks a turning point in cosmology, thanks in particular to their unprecedented statistics. With its 8.4 meter mirror and 3200 mega-pixel camera, LSST is the first ground-based telescope specifically designed to measure weak lensing. The detection of several billion galaxies is expected after 10 years. However, measuring shear with LSST is subject to various systematic effects (instrumental, atmospheric, selection, etc.), creating multiplicative and additive biases that are crucial to control at specific thresholds. A more detailed description of the LSST telescope and the challenges involved in measuring shear are given in Chapter 3.

One source of systematic effects in shear measurement is the shear estimator in itself. Since the 90s, several estimators have been developed, without any real consensus being reached. Estimation of shear begins with measurement of object shapes (such as galaxy ellipticity), followed by calibration to correct for atmospheric and instrumental effects. Galaxy shapes can be determined by model fitting or by direct measurement on images (second moments). Calibration also varies from a method to another, often based on simulations or perturbative processes. This thesis presents a new shear estimation method based on second moments with a perturbative calibration, detailed in Chapter 4. This new estimator has been tested on noise-free simulations varying galaxy and atmospheric model profiles, and the results are given in Chapter 5.

Finally, it is important to take into account the impact of noise on shear measurements, particularly shot noise (caused by the variability of photon detection on a sensor), which introduces a bias into the measurement of object shapes. This bias is correlated with galaxy ellipticity and signal-to-noise ratio (SNR). All shear estimators are affected by this bias, and although several correction methods have been proposed, they have certain limitations (separation of variables, restrictive assumptions, long computation time). The approach explored in this thesis proposes to correct noise bias analytically, via the second derivatives of the shear estimator's Taylor expansion, without assumptions on galaxy profiles and with computational advantages. This correction method and promising initial results are developed in Chapter 6.

1

Cosmology

Contents

1.1 General Relativity

To understand our universe, we need a mathematical description of its geometry and evolution. General Relativity (GR) is a theory that depicts how gravitation affects the curvature of space-time induced by objects with mass and energy. In this section, we will define the principle concepts of general relativity that are needed to understand cosmology.

1.1.1 Metric

In general relativity, we consider that space and time are connected in our universe. It's important to note one aspect : desiring to establish a spacetime continuum inherently implies that the quantities of space and time are given the same physical dimension. By convention, we opt for the dimension of length for this equivalence. To obtain times in the usual dimension, we must introduce a conversion factor with the dimensions of velocity :

$$c = 2.99792458 \times 10^8 m.s^{-1} \tag{1.1}$$

This constant c is the speed of light in vacuum.

To describe the local geometry of spacetime, we use the *metric* tensor, that also represents the "gravitational potential" in the weak-field approximation :

$$g_{\mu\nu} = \begin{pmatrix} g_{00} & g_{01} & g_{02} & g_{03} \\ g_{10} & g_{11} & g_{12} & g_{13} \\ g_{20} & g_{21} & g_{22} & g_{23} \\ g_{30} & g_{31} & g_{32} & g_{33} \end{pmatrix} \tag{1.2}$$

In the Minkowski metric, i.e. a flat space metric, $g_{\mu\nu}$ is defined as follows :

$$g_{\mu\nu} = \begin{pmatrix} -1 & 0 & 0 & 0 \\ 0 & 1 & 0 & 0 \\ 0 & 0 & 1 & 0 \\ 0 & 0 & 0 & 1 \end{pmatrix} \tag{1.3}$$

By imagining the universe as mapped by a grid, the interval between two spacetime coordinates can be defined as the side of a cell. This infinitesimal line element is called ds :

$$\begin{aligned} ds^2 &= g_{\mu\nu} dx^\mu dx^\nu \\ &= -c^2 dt^2 + d\vec{x}^2 \end{aligned} \tag{1.4}$$

The Greek indices in these equations run over [0,3], and the Latin ones only over [1,3], as they represent the spatial counterpart.

1.1.2 The equivalence principle

The equivalence principle assumes that inertial and gravitational masses are identical. In other words, two bodies immersed in the same gravitational field and not subject to other external forces will fall simultaneously if released simultaneously.
This principle was reformulated by Albert Einstein (Einstein, 1908) within the general relativity framework, implying that the laws of physics are the same in a constant gravitational field and a uniformly accelerated frame of reference. This means that an inertial frame of reference (free fall) cannot be differentiated from a non-gravitational frame of reference. In GR, this kind of frame of reference must be locally a Minkowski space.

Numerous tests validating this principle have been conducted since Simon Stevin's first experiment in 1586 (involving the release of two lead balls of different masses). The most recent is the MICROSCOPE satellite mission (Touboul et al., 2022), which constrained the Eötvös parameter for a pair of test masses made of titanium and platinum alloys to an unprecedented accuracy of 1.5×10^{-15}.

1.1.3 Geodesic

Considering that gravity acts like a space-time deformation and not like a force in general relativity means that particles are following the shortest path in this curved space, which is not longer a straight line. This path is called *geodesic*, and we can derive its equation following the equivalence principle (Weinberg, 1972).
If we consider a free-fall coordinate system X^μ, a free-fall particle does not accelerate in the vicinity of an event point, and we can locally apply the following equation :

$$\frac{d^2X^\mu}{d^2X^0} = 0 \tag{1.5}$$

Using the multidimensional chain rule :

$$\frac{dX^\mu}{dX^0} = \frac{dx^\nu}{dX^0}\frac{\partial X^\mu}{\partial x^\nu} \tag{1.6}$$

Deriving a second time according to equation 1.5 and multiplying by $\frac{\partial x^\lambda}{\partial X^\mu}$ on both sides, we find the geodesic equation :

$$\begin{aligned} \frac{d^2x^\lambda}{d^2X^0} &= -\frac{dx^\nu}{dX^0}\frac{dx^\alpha}{dX^0}\left[\frac{\partial^2 X^\mu}{\partial x^\nu \partial x^\alpha}\frac{\partial x^\lambda}{\partial X^\mu}\right] \\ \frac{d^2x^\lambda}{d^2X^0} &= -\Gamma^\lambda_{\nu\alpha}\frac{dx^\nu}{dX^0}\frac{dx^\alpha}{dX^0} \end{aligned} \tag{1.7}$$

where $\Gamma^\lambda_{\nu\alpha}$ are Christoffel symbols, also called the affine connection coefficients. This equation is analogous of Newton's law of motion which describes the motion of particles in classical mechanics.

1.1.4 Einstein equations

A fundamental concept in general relativity is that the distribution of matter and energy in spacetime dictates the metric, shaping the geometry of spacetime accordingly. The metric and the content of the universe are linked through the Einstein equation (Einstein, 1915) :

$$G_{\mu\nu} + \Lambda g_{\mu\nu} = \frac{8\pi\mathcal{G}}{c^4} T_{\mu\nu} \tag{1.8}$$

where the left-hand side of the equation represents the geometry of the universe, and the right-hand side its energy content.
In this equation :

- $G_{\mu\nu}$ is the Einstein tensor : $G_{\mu\nu} = R_{\mu\nu} - \frac{1}{2} g_{\mu\nu}\mathcal{R}$, where $R_{\mu\nu}$ is the Ricci tensor and $\mathcal{R}$ the Ricci scalar. The Einstein tensor is a non-linear function of $g_{\mu\nu}$ and its derivatives. It describes the curvature of spacetime.

- Λ is the cosmological constant. It did not appear in Einstein's first calculations, but was later added with a precise value to match his idea of a static universe. We can move Λ on either side of the equation : if it appears on the left-hand side, it is interpreted as a universe's geometry modification, and therefore to general relativity ; on the right-hand side, it appears more like a new fluid that can be interpreted as a "vacuum energy density". More details about Λ are given in sections 1.3 and 1.5.

- $\mathcal{G}$ is the Newton's gravitational constant.

- $T_{\mu\nu}$ is the stress-energy tensor that represents the mass and energy distribution in spacetime. It contains density and flux components of both energy and momentum (see figure 1.1). Because $G_{\mu\nu}$ covariant derivative vanishes, Einstein Equations imply that $\nabla^{mu} T_{\mu\nu} = 0$, which is the conservation of energy and momentum.

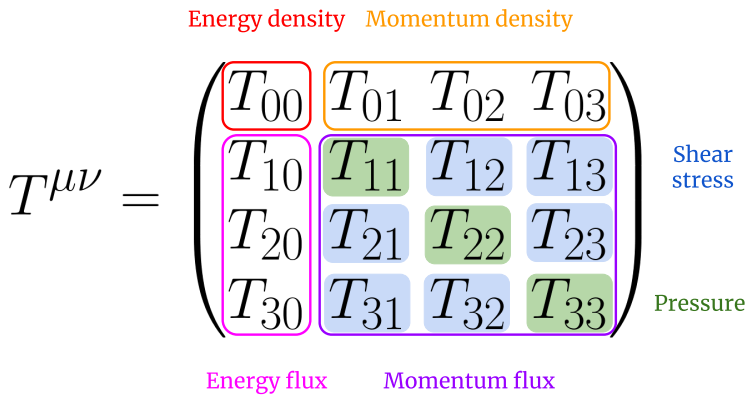

Figure 1.1: *Components of the stress-energy tensor.*

1.2 The cosmological principle

Even though we observe clustering and the undeniable significance of clumpiness in the cosmos, we can extend the Copernican principle (postulate that there is no privileged point of view in the universe) to encompass the entirety of the universe. At large scales, the universe is homogeneous and isotropic, i.e. its structure and characteristics remain the same everywhere and from any direction of observation.

1.2.1 Homogeneity

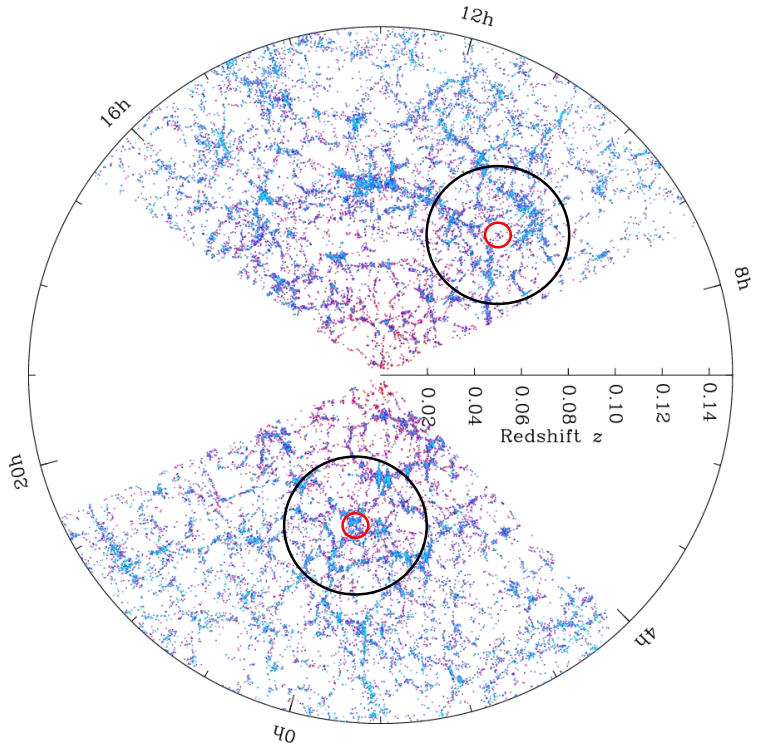

Figure 1.2: *The SDSS 3-dimensional galaxies distribution map. At small scales, the galaxy density of two different zones can be drastically different (red circles), but looking at larger scales, the density of galaxies is becoming increasingly uniform (black circles). Our galaxy is located at the center.*

Looking at the solar system or galaxy scale, the universe looks heavily inhomogeneous. But considering cosmological distances of the hundred of Megaparsec order, the object distribution becomes more and more uniform at large scales. As shown in figure 1.2, the galaxy distribution observed by the Sloan Digital Sky Survey (SDSS) 6th-year data release is compatible with the assumption of homogeneity for scales of $R \geqslant 70\ h^{-1}$Mpc (Sarkar et al., 2009).

1.2.2 Isotropy

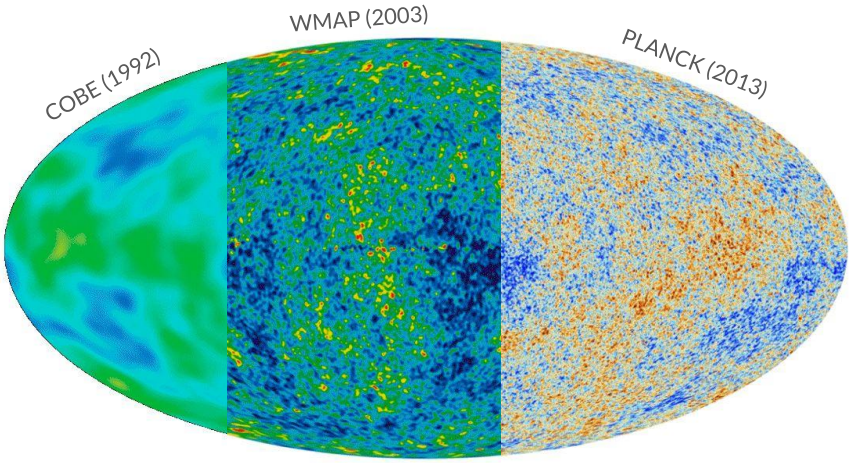

Figure 1.3: *Different maps taken over the years showing the CMB temperature fluctuations.*

For over thirty years, observations of the Cosmic Microwave Background (CMB, more details in section 1.6.1) by the Cosmic Background Explorer (COBE, Mather et al. (1990)), the Wilkinson Microwave Anisotropy Probe (WMAP, Spergel et al. (2007)) and the Planck telescope (Planck Collaboration et al., 2014) have confirmed that the large-scale structure of the universe remains the same regardless of the direction of observation. The latest CMB measurement made by Planck showed that its temperature fluctuation is subject to very small anisotropies, of the order of 10^{-5} at an angular scale of 0.01 rad (once subtracted the dipole, which is of the order of 10^{-3}).

1.3 A universe in expansion

1.3.1 Redshift

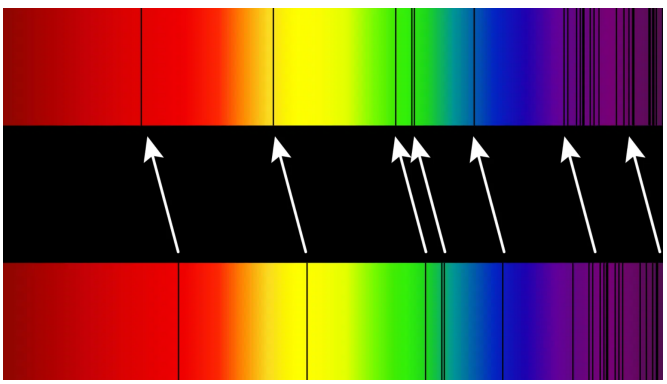

Figure 1.4: *Top : redshifted spectrum of a distant galaxy cluster*
Bottom : spectrum of the Sun (Credit : Georg Wiora)

Luminous objects in the universe like stars or galaxies are emitting electromagnetic radiation, enabling the determination of their chemical composition by looking at their absorption spectrum and their emission or absorption lines witnesses their chemical composition. For a given chemical specie, we expect its absorption (or emission) lines to be at very specific wavelengths in the spectrum.
When observing some astrophysical object's spectrum, one can in general detect a global shift of these absorption lines towards longer (redder) wavelengths, similar to a Doppler effect, that is called *redshift* (see figure 1.4). This shift is attributed to the universe's expansion, which increases the distance between two points at fixed coordinates (see figure 1.5). Except at low redshifts, the relation between redshift and recession velocity differs from the special relativity one. The difference can be attributed to gravitational effects.

In practice, the observed redshift is not only the result of the universe expansion, but also to the peculiar motions of galaxies (due to gravitational attraction in clusters, and more generally the peculiar motions in large-scale structures) (Davis et al., 2011). Peculiar velocities can introduce systematic errors in the cosmological parameters' estimation if they are neglected, especially for redshifts $\lesssim 0.5$ (Sugiura, Sugiyama, and Sasaki, 1999). The observed redshift z_{obs} can be expressed as follows :

$$(1 + z_{obs}) = (1 + z)(1 + z_{pec})(1 + z_{grav}) \tag{1.9}$$

with z the redshift only due to the universe expansion, z_{grav} the redshift due to density fluctuations, and z_{pec} the redshift due to peculiar velocity :

$$1 + z_{pec} = \sqrt{\frac{1 + v_{pec}/c}{1 - v_{pec}/c}} \tag{1.10}$$

where v_{pec} stands for the peculiar velocity. In the non-relativistic limit, we can approximate $z_{pec} \approx v_{pec}/c$.

Knowing the expected wavelengths of the various chemical species from laboratory measurements, the redshift can be determined as follows :

$$z_{obs} = \frac{\lambda_{obs} - \lambda_0}{\lambda_0} \tag{1.11}$$

where λ_{obs} is the observed wavelength and λ_0 the expected one.

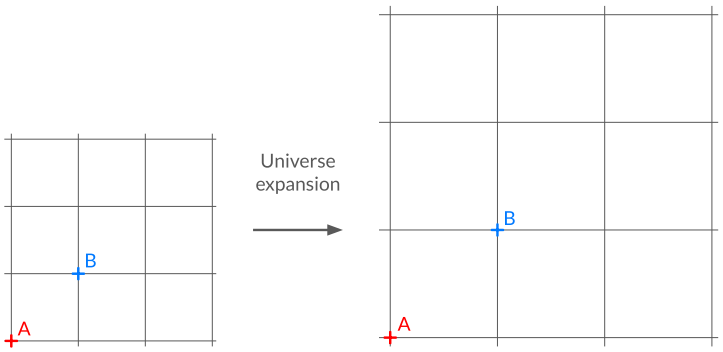

Figure 1.5: *The distance between two objects at fixed positions in spacetime increases because of universe expansion.*

1.3.2 Hubble-Lemaître law

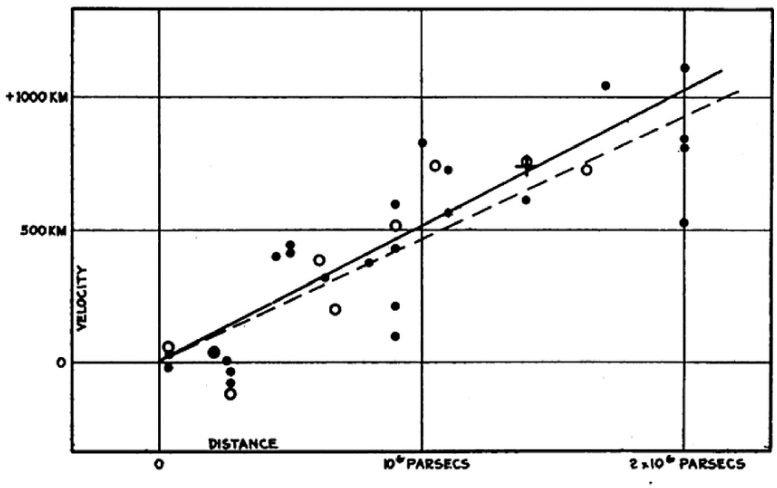

Velocity-Distance Relation among Extra-Galactic Nebulae.

Figure 1.6: *Hubble diagram from Hubble (1929)*

The relationship between the variation of a Cepheid's light and its absolute magnitude (period-luminosity relation) was first demonstrated by Henrietta Leavitt in 1912 (Leavitt and Pickering, 1912). As Cepheids are considered as standard candles, i.e. a source that has a known luminosity, they provide very accurate distance measurements. Building upon this initial result, Edwin Hubble was able to deduce a relationship between galaxy distances (still using Cepheids) and their redshift, now known as "Hubble-Lemaître's law" (Lemaître (1927), Hubble (1929)) :

$$cz = H_0 d \tag{1.12}$$

with H_0 the Hubble constant, which represents the inverse of a time and is usually expressed in $km.s^{-1}.Mpc^{-1}$ and d the distance in Mpc. The left-hand side term of

this equation can by interpreted as the apparent recession speed of the considered object.
This relation led to a fundamental conclusion in cosmology : galaxies seem to move away from each other at a speed proportional to their distance. In other terms, the universe is expanding.

The value of H_0 originally estimated by Hubble in 1929 was 500 $km.s^{-1}.Mpc^{-1}$ (see figure 1.6). The precision of its measurement evolved down to a value between 50 and 100 $km.s^{-1}.Mpc^{-1}$ towards the middle of the 20th century, and the most recent measurements are in agreement at around 70 $km.s^{-1}.Mpc^{-1}$. Until the end of the 2010s, H_0 was always measured directly (using standard candles), but new indirect measurement methods were developed in the last decade. Today, these two methods yield different values, giving rise to a cosmological tension :

- Direct measurement with standard candles (Cepheids and supernovas) : $H_0 = 73.0 \pm 1.0$ $km.s^{-1}.Mpc^{-1}$ (Riess et al., 2022)
- Indirect measurement with CMB : $H_0 = 67.4 \pm 0.5$ $km.s^{-1}.Mpc^{-1}$ (Planck Collaboration et al., 2020)

It is important to note that, despite these two values differing formally by 5σ, the discrepancy is less than 10%, which is a notable success of the cosmological model (see section 1.5).

1.3.3 Dark energy

During the 90s, other tracers emerged, notably type Ia supernovas (SNIa, more details are given in section 1.6.3), which are also standard candles. By studying SNIa, Saul Perlmutter's team (Perlmutter et al. (1999)), along with Adam Riess and Brian Schmidt (Riess et al. (1998), Schmidt et al. (1998)), found that their apparent magnitude at redshifts around 0.5 was weaker than expected in a matter-dominated universe, indicating that the universe's expansion was accelerating rather than slowing down. This unexpected finding suggested the presence of a mysterious force, later termed "dark energy", which opposes gravity and drives galaxies apart. Figure 1.7 shows two Hubble diagrams reporting the accelerating universe expansion, and thus the presence of dark energy.

The nature of dark energy remains undetermined, but several hypotheses are considered : the cosmological constant Λ introduced in section 1.1.4, a modification of the (geometrical) left-hand side of the Einstein equation (but only at large scales), or considering a fluid with the following equation of state (with the pressure p and density ρ) :

$$w = \frac{p}{\rho} \tag{1.13}$$

that can be interpreted as an addition to the right-hand side of the Einstein equation, representing the universe's content. The acceleration of the expansion starts from $w < -1/3$, its current value corresponding rather to values of w close to -1.

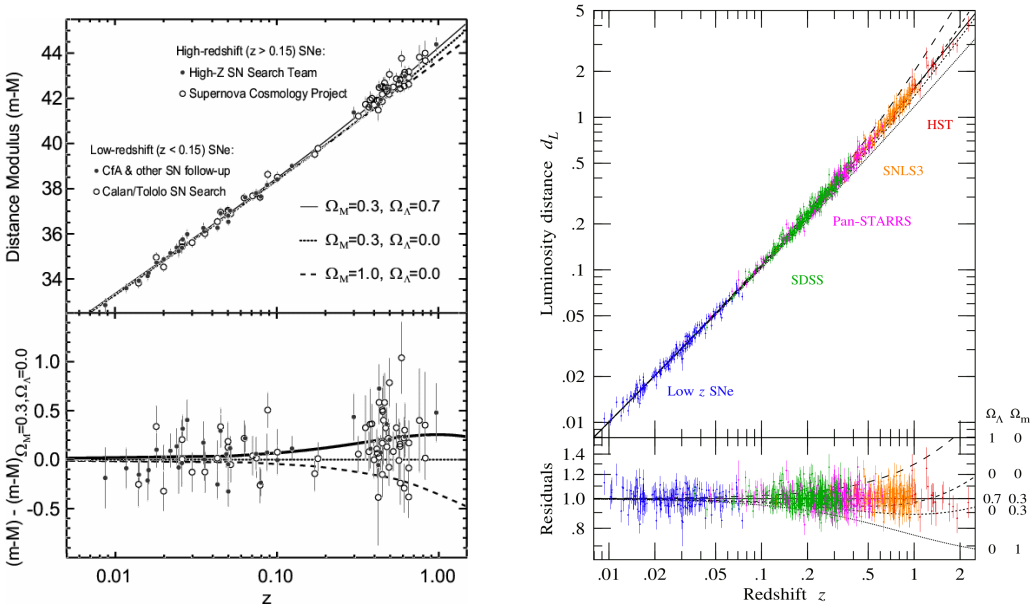

Figure 1.7: *Left : Hubble diagram from Perlmutter and Schmidt (2003)*
Right : Hubble diagram from Scolnic et al. (2018)

1.4 The Friedmann Lemaître Robertson Walker metric

Considering an isotropic and homogeneous universe in expansion, the Friedmann-Lemaître-Robertson-Walker (FLRW) metric is conventionally used to describe space-time geometry.

Analogously to equation 1.4, we can define FLRW's ds :

$$ds^2 = -c^2dt^2 + a^2(t)\gamma_{ij}dx^i dx^j \tag{1.14}$$

or in polar coordinates, usually chosen for its isotropic properties :

$$ds^2 = -c^2dt^2 + a(t)^2\left[\frac{dr^2}{1-kr^2} + r^2(d\theta^2 + \sin^2\theta\, d\phi^2)\right] \tag{1.15}$$

The coordinates system (r,θ,ϕ) is *comoving*, meaning that the coordinates of an object in the universe remain constant regardless of the expansion. The scale factor $a(t)$ denotes either a contraction or expansion of space, suggesting that the distance between two objects evolves with time. We can deduce the universe's evolution from the sign of the scale factor derivative with respect to the cosmic time t :

- $\dot{a}(t) > 0$: expanding universe
- $\dot{a}(t) = 0$: static universe
- $\dot{a}(t) < 0$: contracting universe

We can link the scale factor and the redshift through the following equation :

$$a(t) = \frac{1}{1+z} \tag{1.16}$$

This means that if we receive today the light emitted by a distant comoving object with a redshift of z, then the scale factor at the moment when the object initially emitted this light is a. It assumes that the emitter and receiver are comoving. As $z = 0$ at t_0, we have $a(t_0) = a_0 = 1$. The full proof of this relation can be found p.71 and p.72 of Peacock (1999).

The curvature is described by its factor k. This parameter is what describes the universe's geometry. One way of representing the curvature is to consider a triangle : on a flat surface with no curvature, the sum of the angles is 180°, but it is superior to 180° on a sphere (positive curvature) and inferior on a hyperboloid (negative curvature). This factor k can take only three different values : $+1$, 0, and -1 :

- k $= 1$: spherical universe
- k $= 0$: flat universe
- k $=$ -1 : hyperbolic universe

The expansion rate of the universe, also called the Hubble parameter, can be expressed as a function of $a(t)$:

$$H(t) = \frac{\dot{a}(t)}{a(t)} \tag{1.17}$$

Its current value is the Hubble constant, H_0, defined earlier in equation 1.12.

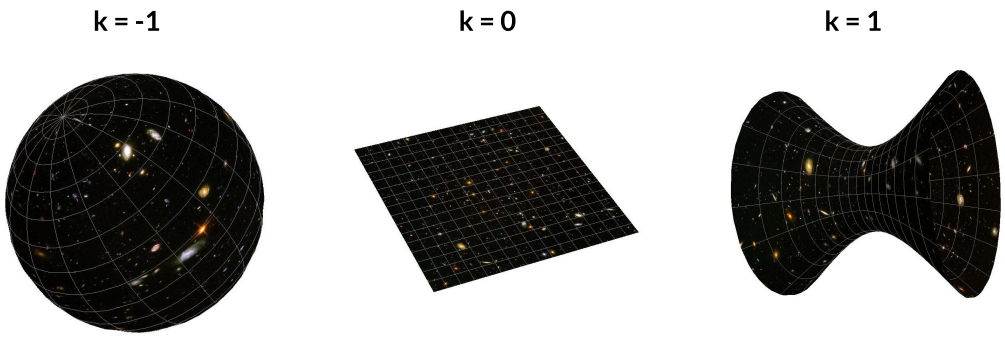

Figure 1.8: *Universe geometry depending on the curvature value.*

1.4.1 Cosmological distances

There are different ways of measuring distances in cosmology, depending on the observable under consideration.

Comoving distance

The comoving distance corresponds to the separation between two points considering a comoving coordinates system. By definition of such a system, this distance does not change with time. Taking the polar coordinates system defined above, the comoving distance is defined as follows :

$$\chi = \int \frac{dr}{\sqrt{1 - kr^2}} \tag{1.18}$$

the radial counterpart being the only one depending on k. We then have :

$$r = S_k(\chi) = \begin{cases} \sin(\chi) & \text{if } k = -1 \\ \sinh(\chi) & \text{if } k = +1 \\ \chi & \text{if } k = 0 \end{cases}$$

Recent measurements of k tend to strongly favor zero curvature (the latest being DESI Collaboration et al. (2024)). We will thus consider the case where $k = 0$ in the next section.
The comoving distance can be computed along the line of sight by integrating H over the redshift between a source located at a fixed z_0 and the observer :

$$\chi(z) = \frac{1}{a_0} \int_0^{z_0} \frac{cdz}{H(z)} \tag{1.19}$$

Angular diameter distance

The angular diameter distance of an object is defined by the ratio between its size D and its apparent angle θ. It is related to the comoving distance through :

$$D_A = \frac{D}{\theta} = a(t) S_k(\chi) = \frac{a_0 S_k(\chi)}{1 + z} \tag{1.20}$$

Considering a flat universe, it becomes :

$$D_A = \frac{1}{1 + z} \chi(z) \tag{1.21}$$

Luminosity distance

In a flat space, the flux of a source received by an observer writes :

$$F = \frac{L}{4\pi D_L^2} \tag{1.22}$$

where L is the apparent luminosity of the source and D_L the distance separating the source and the observer.
The luminosity distance therefore reads :

$$D_L = \sqrt{\frac{L}{4\pi F}} \tag{1.23}$$

and can be linked to the comoving distance through :

$$D_L = (1+z)a_0 S_k(\chi) \tag{1.24}$$

and to the angular diameter distance via the reciprocal relationship :

$$D_L = (1+z)^2 D_A \tag{1.25}$$

At low redshift ($z \ll 1$), D_L and D_A converge to similar values, leading to the Hubble-Lemaître law defined in 1.3.2 :

$$D_A(z) \simeq D_L(z) \simeq \frac{cz}{H_0} \tag{1.26}$$

1.4.2 Friedmann equations and solutions

Similar to dark energy, we can consider that the universe is made up of perfect fluids whose equations of state depend on their pressure and density. Assuming an isotropic and homogeneous universe, p and ρ are only time-dependant, the stress-energy tensor is now :

$$T_{\mu\nu} = \text{diag}(-\rho c^2, p, p, p)$$

We can define two different equations from the Einstein equation and the stress-energy tensor :

$$\left(\frac{\dot{a}}{a}\right)^2 = H^2(t) = \frac{8\pi\mathcal{G}}{3}\rho - \frac{kc^2}{a^2(t)} + \frac{\Lambda c^2}{3} \tag{1.27}$$

$$\frac{\ddot{a}}{a} = \dot{H}(t) + H^2(t) = -\frac{4\pi\mathcal{G}}{3}\left(\rho + 3\frac{p}{c^2}\right) + \frac{\Lambda c^2}{3} \tag{1.28}$$

where the first equation 1.27 comes from the temporal (00) component in $G_{\mu\nu}$ and $T_{\mu\nu}$, and the second 1.28 from the spatial (ij) components. They are called the Friedmann equations.

By deriving 1.27 with respect to time, then replacing $\dot{H}$ and H^2 by their expressions from 1.28, we obtain the *energy conservation equation* :

$$\begin{aligned} \dot{\rho} &= -3H\left(\rho + \frac{p}{c^2}\right) \\ &= -3\frac{\dot{a}}{a}\left(\rho + \frac{p}{c^2}\right) \end{aligned} \tag{1.29}$$

Under the assumption that the universe's expansion follows an adiabatic process, we can also find this result through thermodynamics. Considering a perfect gas equation

of state $p = wc^2\rho$, with w constant, we can simplify equation 1.29 and then integrate it :

$$\rho(t) = \rho_0 \left(\frac{a}{a_0}\right)^{-3(1+w)} \tag{1.30}$$

where $\rho_0 \equiv \rho(t_0)$ and $a_0 \equiv a(t_0)$. This equation defines the density evolution of the universe's components. In flat space, for a single component, the scale factor solution is :

$$a(t) \propto t^{\frac{2}{3(w+1)}} \tag{1.31}$$

In the special case where $w = -1$, the scale factor grows exponentially. Considering a universe in expansion, we can identify several special cases where the Friedmann equation can be easily solved, designated by w :

- When $w = 0$: $\begin{cases} \rho \propto a^{-3} & ; p \simeq 0 \\ a \propto t^{\frac{2}{3}} \end{cases}$

  which represents a **matter-dominated** universe

- When $w = 1/3$: $\begin{cases} \rho \propto a^{-4} & ; p \propto \rho/3 \\ a \propto t^{\frac{1}{2}} \end{cases}$

  which represents a **radiation-dominated** universe

- When $w =$ -1 : $\begin{cases} p \propto -\rho \\ a \propto e^{t\sqrt{\Lambda/3}} \end{cases}$

  which represents a **dark energy-dominated** universe

The universe has gone through these three phases in its history : the radiation era for $z \gtrsim 3000$, when relativistic particles were dominating the energy budget ; the matter era for $3000 \gtrsim z \gtrsim 0.5$ with non-relativistic particles whose thermal agitation speed is negligible compared to c ; and the dark energy era for $z \leq 0.5$. For all of these eras, the scale factor first derivative $\dot{a}(t)$ was positive, so the universe was always expanding. However, considering the second derivative $\ddot{a}(t)$, the expansion was decelerating during radiation and matter era ($\ddot{a}(t) < 0$) and is now accelerating during the dark energy era ($\ddot{a}(t) > 0$).

Using the critical density, defined for a universe with no spatial curvature ($k = 0$) :

$$\rho_c = \frac{3H_0^2}{8\pi\mathcal{G}}, \tag{1.32}$$

we can express the *current* density of the different components as follows :

$$\begin{aligned} \Omega_i &= \frac{\rho_i}{\rho_c} \\ \Omega_k &= -\frac{kc^2}{H_0^2 a_0^2} \end{aligned} \tag{1.33}$$

The first Friedmann equation 1.27 can be rewritten :

$$H^2(t) = H_0^2 \left[\Omega_r a^{-4} + \Omega_m a^{-3} + \Omega_k a^{-2} + \Omega_\Lambda\right] \tag{1.34}$$

where index r represents radiation, m matter, k curvature and Λ cosmological constant. Today, for $a(t_0) = 1$, this expression becomes even simpler :

$$\Omega_r + \Omega_m + \Omega_k + \Omega_\Lambda = 1 \tag{1.35}$$

The value of Ω_i depends on the Hubble constant H. Therefore it is often useful to quote observational results in terms of $\omega_i = \Omega_i h^2$ (where h the reduced Hubble constant $h = H_0/(100 kms^{-1}Mpc^{-1})$), which results in the *physical* density parameters.

1.5 ΛCDM model

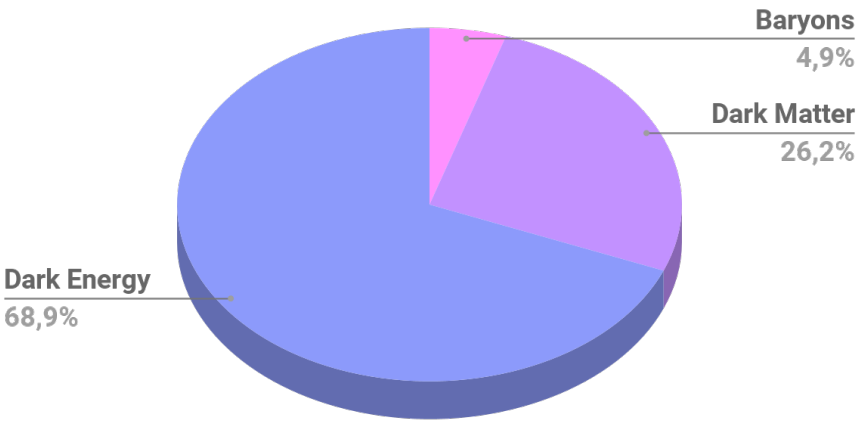

Figure 1.9: *Proportions of baryons, dark matter and dark energy today according to Planck*

The ΛCDM model is the most widely accepted in cosmology due to its simplicity in explaining the features of the observable universe. Its denomination comes from the cosmological constant Λ used to describe dark energy, and CDM for "Cold Dark Matter", which are the two major components of the universe, representing 95% of its content today (see figure 1.9).

The **baryonic matter** depicts every constituent of the atoms found in the universe (protons, neutrons, electrons), in other words, what we call "ordinary" and "observable" matter. Baryons are sensitive to both gravitational and electromagnetic interaction, this is why we can detect and interact with them.

Firstly suggested by Fritz Zwicky in 1933 (Zwicky, 1933) after he observed excessive galaxy velocities in the Coma cluster, concluding that the dynamical stability of these structures could not be based solely on their luminous mass, dark matter is

introduced in the model to account of gravitational effects observed in large-scale structures (galaxy rotation curves problem (see section 3.1.2.c), gravitational lensing (see chapter 2)), yet remains unidentified today. The "cold" dark matter stands for non-baryonic particles, non-relativistic, collisionless (interacts with other particles only through gravitation) and dissipationless (does not emit photons to lose energy and cool down). An hypothesis a for baryonic dark matter candidate was formulated by Paczynski (1986), considering Massive Compact Halo Objects (MACHOs) such as black holes, neutron stars or white dwarfs. A summary of the experiments used to test the MACHOs hypothesis is given in Tisserand et al. (2007). This hypothesis has now been largely abandoned in favor of non-baryonic dark matter candidates such as WIMPs (Weakly Interactive Massives Particles) and axions (which are stable, neutral, and very low-mass elementary particles).

Parameter	**Description**	**Value** (according to Planck 2024)
$\Omega_b h^2$	The baryon density	0.0223 $\pm$ 0.0001
$\Omega_c h^2$	The dark matter density	0.120 $\pm$ 0.001
t_0	The age of the universe	13.801 $\pm$ 0.024 Gyr
$\ln(10^{10} A_s)$	The curvature fluctuation amplitude	3.043 $\pm$ 0.014
n_s	The scalar spectral index. It represents the slope of Δ^2_R. If $n_s = 1$, this means that density fluctuations have an identical spectrum on any scale	0.965 $\pm$ 0.004
τ	The reionization optical depth. The fit usually concerns $e^{-\tau}$ which is the fraction of CMB photons scattered between their emission and their detection.	0.054 $\pm$ 0.007

Table 1.1: *ΛCDM independent parameters and their numerical values according to Planck Collaboration et al. (2020).*

The ΛCDM model can be described by six free and independent parameters, listed in table 1.1.
We can define other parameters derived from the six previous ones, such as H_0 or σ_8, the latter being the standard deviation of the density fluctuation in an 8 h^{-1} Mpc radius sphere. It allows to identify matter inhomogeneities in different parts of the universe.
This model also includes other parameters set at some assumed values : the total density $\Omega_T = 1$, the equation of state of dark energy w = -1, or the CMB temperature $T_{CMB} = (2.7255 \pm 0.0006) K$ (Fixsen, 2009).

1.6 Cosmological probes

The ΛCDM model was determined from empirical observations, following the discoveries of the CMB and the accelerated expansion using Type Ia supernovas. Today, these probes and others are combined to test and validate (or invalidate) ΛCDM. In this section, we will introduce several cosmological probes and see how their interesting complementarity can be used to constrain different cosmological parameters.

1.6.1 Cosmic Microwave Background

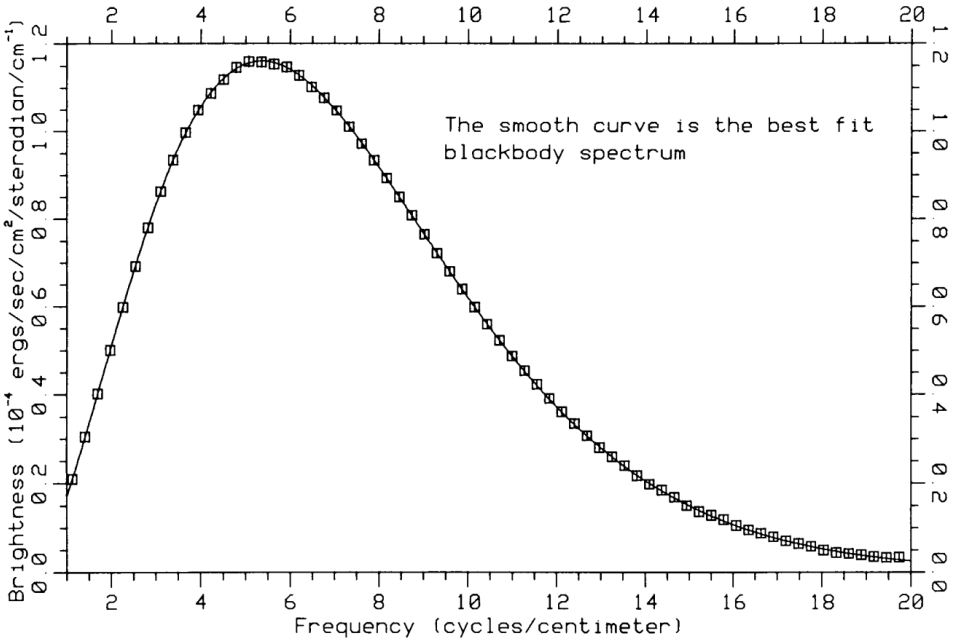

Figure 1.10: *CMB spectrum taken by the FIRAS instrument (each box is a measure point with an assumed error of 1%) compared to a black body (solid line). The figure is from Mather et al. (1990).*

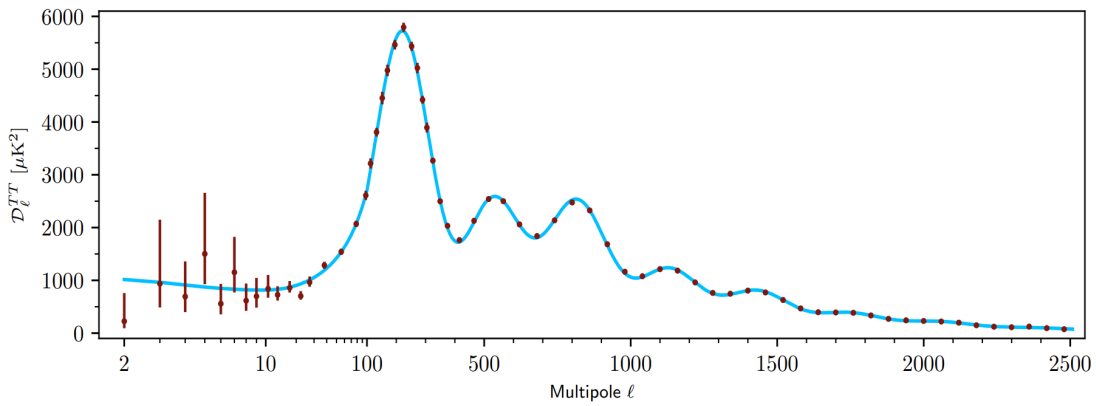

Figure 1.11: *CMB temperature angular power spectrum (from Planck 2020a)*

In its earliest moments, the universe was much hotter and denser than it is today. Above a certain temperature, protons and electrons are dissociated, forming a hot plasma. Thanks to expansion, the universe gradually expanded and cooled, until it reached a temperature of around 3000K, at an age of 380,000 years. At this point, electrons were able to bind to atomic nuclei (creating atoms), and photons, so far exchanged only between electrons, were able to be released and circulate in space. This phenomenon, called *recombination*, left a visible imprint on the universe, called the Cosmic Microwave Background (CMB).
Building on Lemaître's work, Georges Gamow, Ralph Alpher and Robert Herman published models of the Big Bang and predicted the existence of the CMB (Gamow (1948), Alpher and Herman (1950)). The first observation of the CMB was made in 1964 by Arno Penzias and Robert Wilson, through an excess temperature measured by their radio antenna (Penzias and Wilson, 1965). Several successive observation missions have been carried out to characterize it and measure its anisotropies, in particular COBE (1992), WMAP (2003), and Planck (2013).

Measuring the CMB temperature anisotropies gives us information about the original plasma density, the overdensities being linked to the hotter spots in the spectrum. These density fluctuations provide informations about the current density fluctuations of large-scale structures.
According to its electromagnetic spectrum taken by the COBE Far Infrared Absolute Spectrophotometer (FIRAS), we can see that the CMB looks like a perfect black body (see figure 1.10). CMB temperature was measured using FIRAS data and gives : $T_{CMB} = (2.7255 \pm 0.0006)K$ (Fixsen, 2009).
Observable peaks in the temperature angular power spectrum (figure 1.11) correspond to acoustic oscillations (see more in section 1.6.2). The position and height of these peaks tells us about the composition of the universe, and therefore about cosmological parameters : we can separate $\Omega_m h^2$, $\Omega_b h^2$ and A_s from the peaks' amplitude, and their positions also depend on $\Omega_m h^2$ and $\Omega_b h^2$ because of the speed of sound.

1.6.2 Baryonic Acoustic Oscillations

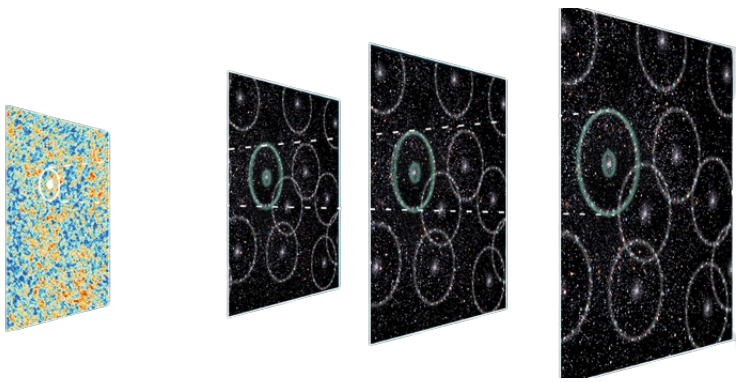

Figure 1.12: *Schematic representation of Baryon Acoustic Oscillations (Credit : ESA and the Planck Collaboration)*

Observed peaks in the CMB spectrum (see previous section) reveal the imprint of acoustic wave propagation in primordial plasma, called "Baryonic Acoustic Oscillations" (BAO). Although globally homogeneous, this initial plasma is subject to slight variations in density. In regions of higher density, gravitational forces are stronger, leading to baryons and photons attraction. Interactions between baryons and photons create an energy that fights gravitation, and this conflict generates oscillations that propagate as spherical waves in the plasma. The position of these perturbations was frozen at the time of recombination, and today we observe these ripples thanks to regions of greater galaxy and cluster density (see figure 1.12). As these ripples are no longer evolving other than through the effects of gravitation and expansion, we can use BAO pattern as a standard ruler to constrain dark matter and dark energy. This characteristic length corresponds to the comoving sound horizon scale r_d at the epoch at which baryons were released from photons. It is observed as a peak in the spatial correlation of anisotropies in the CMB temperature, in the positions of galaxies, or more generally, in the matter density. Considering typical CMB anisotropy amplitude of $\sim$0.01 rad, it corresponds to an "excess" of galaxies at at a comoving distance of 150 Mpc, in other words a 1% excess augmentation in the regions 150 Mpc away from the initial overdensities

1.6.3 Type Ia supernovas

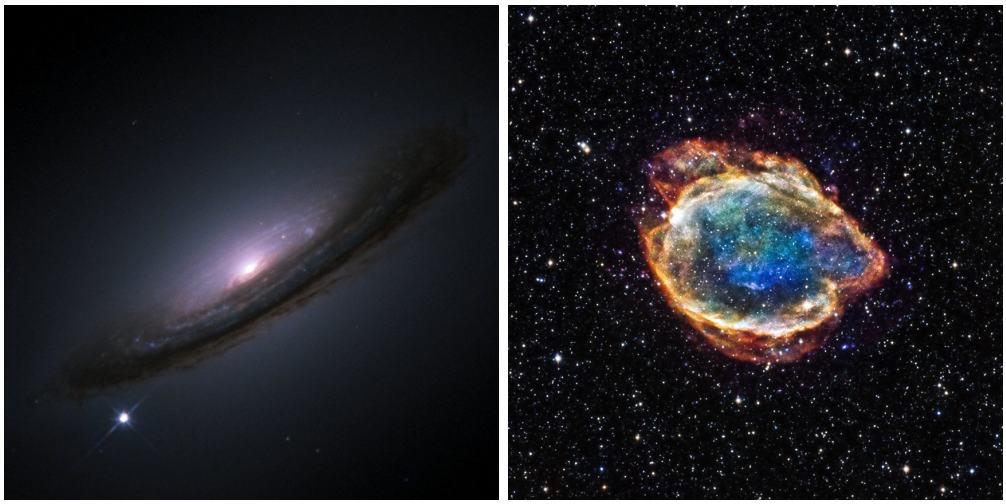

Figure 1.13: *Left : Supernova 1994D in the galaxy NGC 4526 (High-Z Supernova Search Team/HST/NASA)*
Right : Supernova remnant G299 combined X-ray and Infrared images (Chandra Telescope)
X-ray : NASA/CXC/U.Texas/S.Post et al.
Infrared : 2MASS/UMass/IPAC-Caltech/NASA/NSF

A supernova is the explosion of a star at the end of its life, resulting in a sudden increase in its luminosity. Depending on the progenitor and the type of reaction leading to the explosion, there are different categories of supernovas, one of which is known as *thermonuclear* (or Type Ia) supernova. In this particular case, the system is usually made of two massive stars, one of them being a white dwarf and the other

probably a red giant. As the white dwarf has a stronger surface gravity, it progressively accretes hydrogen and helium from the red giant, which is then heated to form carbon. The white dwarf's mass thus increases until it reaches a certain limit (called the Chandrasekhar mass limit), at which point the electron degeneracy pressure is no longer sufficient to maintain the star's gravitational equilibrium, leading to its collapse and explosion. Other type Ia supernova formation processes have been proposed, notably systems involving the merging of two white dwarfs. Type Ia supernovas occur in all types of galaxies, at a rate of 1 or 2 events per millennium, and their apparent luminosity is several billion times higher than the Sun. The matter blown up after the star's explosion produces a remnant, generally in the form of a shell or nebula (see figure 1.13).
The special feature of SNIa is their characteristic light curve, with a spectrum dominated successively by elements between oxygen and calcium at the peak, then by nickel, cobalt, and iron during the decay in brightness. Because we can consider SNIa as a "standard candle", its luminosity and distance from the observer can be linked through the following relation :

$$D_L = \sqrt{\frac{L}{4\pi F}} \tag{1.36}$$

with L the luminosity, F the total flux and D_L the luminosity distance (defined in 1.4.1).
Several algorithms have been developed to model the properties of SNIa, *SALT2* among others (Guy et al., 2007), which used spectro-photometric information from a large dataset, including samples from SNLS. Given these parameters, one can develop a distance estimator to perform cosmological estimations. Today, distances measured from SNIa exhibit a $\sim 7\%$ precision. The first estimation of w with an uncertainty around 0.1 was made by Astier et al. (2006), where Ω_m and w were measured, and another notable one having been produced in 2018 by Scolnic et al. (2018), combining Pan-STARRS and Pantheon SNIa for the cosmological parameters analysis.
A combination of several SNIa datasets using different redshift samples was made by Betoule et al. (2014), making an intercalibration between the SDSS and SNLS surveys.

However, the low-z samples currently available contain few SNIa and are subject to significant instrumental calibration problems, in addition to the intercalibration required to combine them. A new experiment named ZTF (Zwicky Transient Facility, Bellm et al. (2019)), an optical time-domain survey with a 47 square-degree field of view, has collected thousands of SNIa, allowing its catalogs to be used in the future without the need for cross-calibration between several low-z surveys. Concerning cosmology, SNIa observations at low redshift are needed to constrain dark energy, since its effect is most visible in the recent universe. Furthermore, the constraining power of the Hubble diagram primarily depends on its redshift lever arm.

1.6.4 Weak Lensing

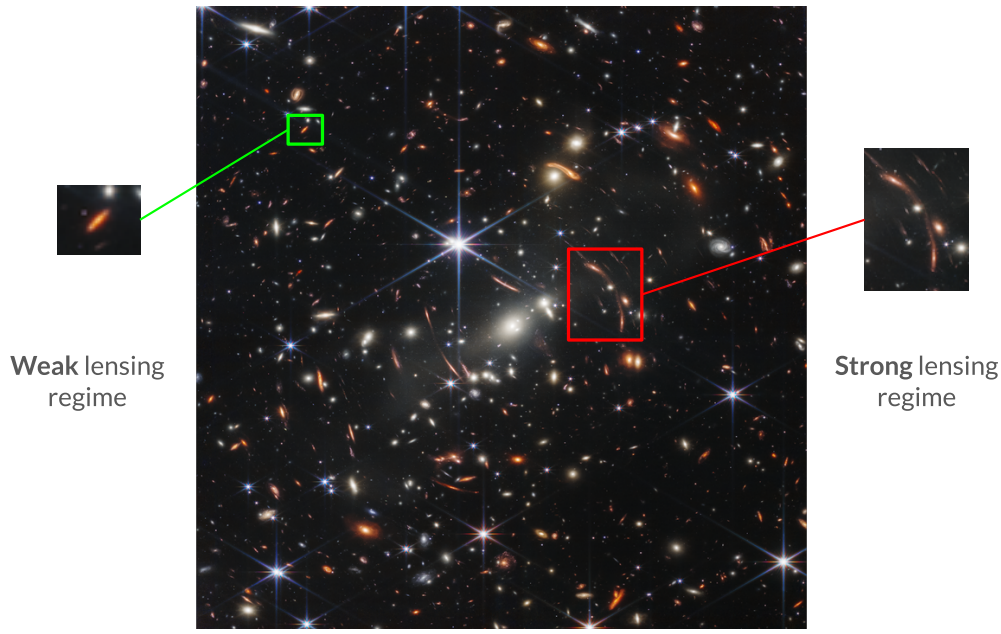

Figure 1.14: *Two regimes of gravitational lensing (galaxy cluster SMACS 0723 from James Webb Spatial Telescope)*

Photons are always following the shorter path (*geodesic*) between two points in the universe. If space-time is flat, this geodesic is straight, but when space-time is curved in the presence of gravitational potential, the geodesic becomes also curved, following the distortion. If an observer is looking at a source (usually a galaxy) located in the background of a cluster that lies between them on the line of sight, the galaxy will appear *distorted* from the observer's point of view. This effect of background shapes' observed distortion is called "gravitational lensing". A full chapter is dedicated to this subject as it is the main topic of this thesis (see chapter 2).

Gravitational lensing can be divided into two categories : *strong* and *weak* lensing (see figure 1.14). Strong lensing is usually caused by very massive structures as galaxy clusters, where the mapping between the source plane and the image plane is not one to one, and where one source can produce multiple images. On the other hand, weak lensing has several regimes of its own that are described right after. They are both investigated in cosmology to characterize the matter distribution in the universe, and its evolution with expansion.

Different regimes of weak lensing

Depending on the nature of the lens, the term of weak lensing actually encompasses several distinct measurements, where the distortion effect can vary in intensity:

- **Galaxy cluster lensing** : Background galaxy shapes distortion by a foreground galaxy cluster. Both strong and weak lensing can be observed in this regime. The distortion effect can be up to 10%. Galaxy cluster lensing is a useful tool to count the clusters and determine their mass, as it is sensitive to all the matter (baryonic and dark matter).

- **Galaxy galaxy lensing** : Occurs when the background galaxy shapes are distorted by an individual galaxy in the foreground. It can sometimes lead to strong lensing, but not as often as the galaxy cluster lensing. The shear signal amplitude depends on the angular distance. Just like cluster lensing, galaxy-galaxy lensing is a suitable probe to understand quantities related to mass, such as mass density profiles, mass-to-light ratios and galaxy mass evolution.

- **Cosmic shear lensing** : Corresponds to the coherent alignment of background galaxy shapes by large-scale structures. The distortion is very subtle, from 0.1% to 1% at redshift $z \sim 1$. Because of its sensitivity to both matter and expansion, the cosmic shear is a powerful tool to understand and constrain dark matter and energy. It is the main focus of this thesis.

1.7 Combining probes : ΛCDM and beyond

Despite the very consistent cosmological constraints achieved using the ΛCDM model, the nature of dark energy dynamics remains insufficiently examined. Furthermore, some tensions have arisen within this model, notably the "H_0 tension" (see section 1.3.2) and the "σ_8 tension". If these tensions cannot be explained by systematic errors, they will be the sign of new physics beyond ΛCDM.

We can mention two different cosmological models (among others) :

- w**CDM** : the dark energy is described by a constant equation of state but not fixed at w = -1 (just like the cosmological constant in ΛCDM)
- $w_0 w_a$**CDM** : the dark energy is described by the following equation of state :

$$w(a) = w_0 + w_a(1 - a)$$

  with w_0 corresponding to its current value and w_a to its time dependence through the scaling factor a. This is a purely phenomenological description aimed at describing most of the dynamical dark energy models.

As some probes are complementary, it is interesting to combine them for higher-precision cosmological estimates. This makes it possible to validate or invalidate a model with greater significance.
Measuring BAO at different redshifts gives us information about the energy content of the universe (Ω_K, Ω_m, Ω_Λ...), and also the $H_0 r_d$ product. The CMB full spectrum informs us about all the cosmological parameters (assuming a model), and we can determine the angular scale of acoustic fluctuations (noted θ^*, directly linked to r_d)

through the position of its first peak. As SNIa are also sensitive to distances, and thanks to their standard candle quality, they can be used to constrain the expansion rate, and so the dark energy. With BAO, these are two quantities directly linked to the geometry of the universe. Measuring r_d with BAOs is equivalent to measuring the SNe luminosity. Both are observed at different redshifts to measure cosmology through the relationship between distance and cosmological parameters.

Regarding the Ω_m and Ω_K constraints measurement, combining BAO and CMB breaks downlifts degeneracies present in each of the two probes (see figure 1.15). This result - and all the following ones - is from the DESI (Dark Energy Spectroscopic Instrument) first year of observations analysis (DESI Collaboration et al. (2024), named D24 after).

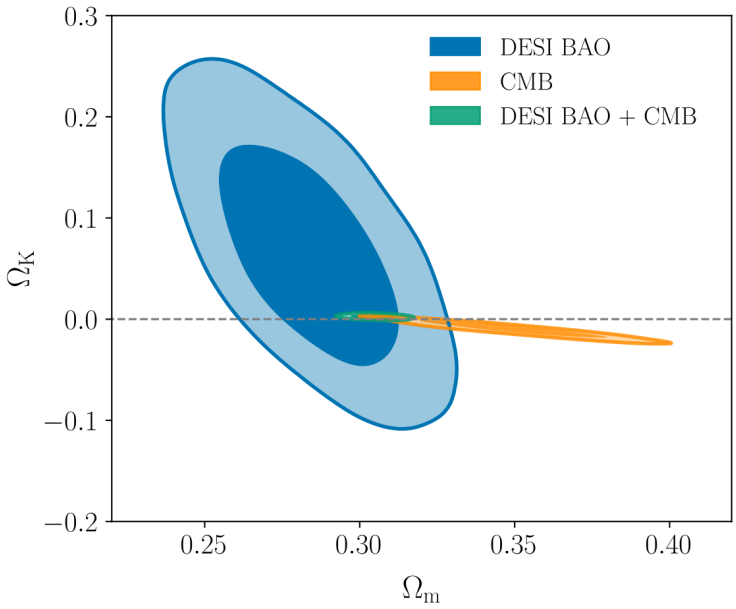

Figure 1.15: *68% and 95% marginalized posterior constraints in the Ω_m-Ω_K plane from DESI BAO (blue), CMB (orange) and DESI+CMB (green). Credits : Arnaud de Mattia*

Concerning dark energy, we can test both wCDM and $w_0 w_a$CDM models using combinations of BAO, CMB and SNIa. For wCDM, the combination of all probes give the following constraint on dark energy equation of state : w = -0.997 $\pm$ 0.025 (see figure 1.16). Note that even if introducing a cosmological constant in the Einstein equation (ΛCDM) and introducing a dark energy component with a constant equation of state parameter w=-1 are mathematically equivalent, measuring w=-1 does not imply that ΛCDM is valid.

When considering a time-varying equation of state for dark energy, the results become more surprising. The combination of BAO, CMB and SNIa seem to favor solutions with $w_0 > -1$ and $w_a < 0$ (see figure 1.17), and the tensions with ΛCDM remain at $\sim$2.5σ for BAO+CMB+PantheonPlus, and rises to $\sim$3.9σ for BAO+CMB+DESY5.

However, even if these results suggest a deviation from ΛCDM, it is important to examine all sources of possible systematic error that could bias the result. In particular, low-redshift SNIa are important for better constraining dark energy. But Pantheon+ (Brout et al., 2022), Union3 (Rubin et al., 2023) and DESY5 (DES Collaboration et al., 2024) share mostly the same (few) low-redshift events, whose instrumental calibration is uncertain. A joint analysis of DESI's BAO, CMB and high-z SNIa samples combined with ZTF's low-z SNIa could provide more robust constraints, as the latter are less prone to calibration problems.

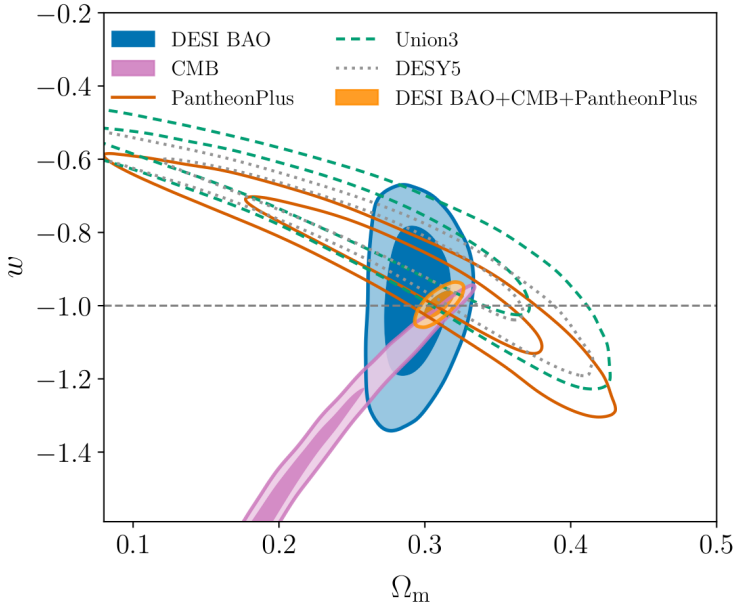

Figure 1.16: *68% and 95% constraints for Ω_m and w in flat wCDM (D24).*

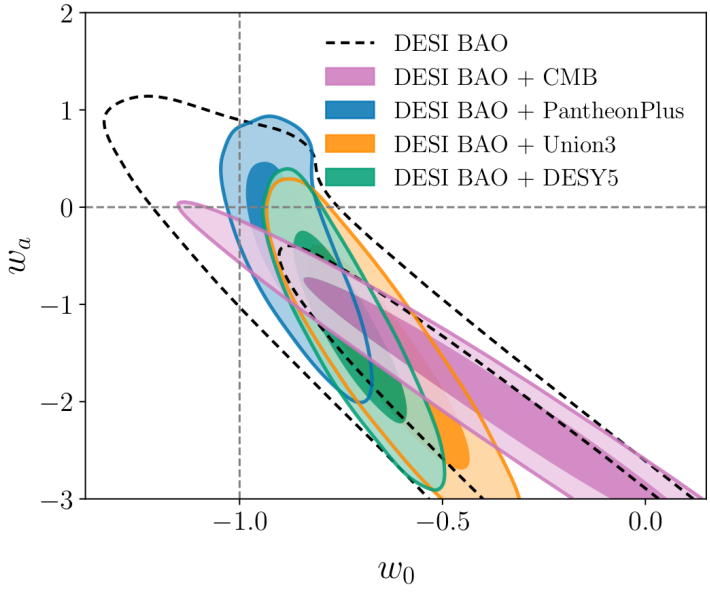

Figure 1.17: *68% and 95% marginalized posterior constraints in the w_0-w_a plane for the flat $w_0 w_a$CDM model (D24).*

Finally, as cosmic shear is marginally sensitive to the universe's geometry but rather to the matter distribution, it is very convenient to constrain the matter-related parameters Ω_m and σ_8. It is usually combined with Planck results which are sensitive to all the cosmological parameters.
Here we will present cosmological constraints performed with cosmic shear with two different surveys : The *Dark Energy Survey* (DES), a wide-area survey using the Blanco Telescope at the Cerro Tololo Inter-American Observatory in Chile, and *Hyper Suprime-Cam* (HSC), an extensive astronomical survey using the Subaru Telescope at the Mauna Kea Observatory in Hawaii.

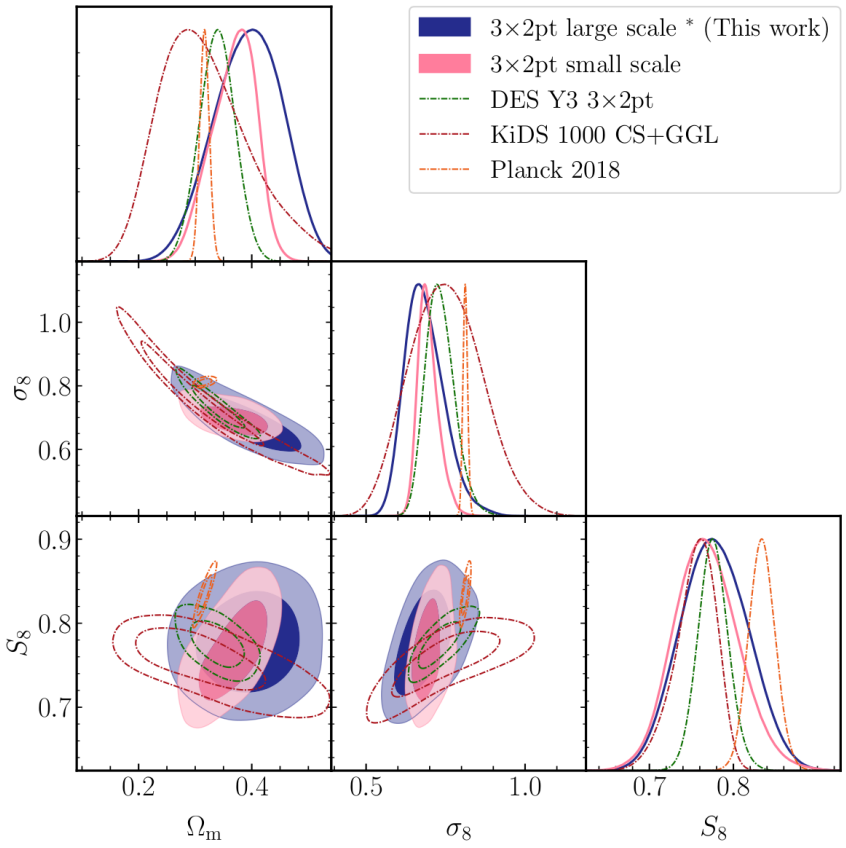

Figure 1.18: *Cosmological constraints from HSC Y3 large-scale 3x2pt combined with HSC Y3 small-scale 3x2pt (Miyatake et al., 2023), Planck 2018 (Planck Collaboration et al., 2020), DES Y3 3x2pt (Amon et al., 2022) and KiDS 1000 (Heymans et al., 2021).*

It is interesting to compare the results of DES and HSC first and third-year analyses. The results of cosmological constraints on Ω_m, S_8 (defined as $S_8 \equiv \sigma_8(\Omega_m/0.3)^{0.5}$ and usually better constrained than σ_8) and w are given in Table 1.2. In both cases, it is important to note that the observed area in Y3 was more than three times higher than in Y1 (for instance, the observed area was 136.9 deg^2 in HSC Y1 (Mandelbaum et al., 2018) and 433.48 deg^2 in Y3 (Li et al., 2022)). These results show that the uncertainties associated to Ω_m and S_8 estimations are similar in Y1 and Y3 for both analyses. As we would expect the uncertainty to decrease with $\sqrt{N}$, we can therefore conclude that uncertainties are dominated by systematic effects (and not by statistics).

	Ω_m (ΛCDM)	S_8 (ΛCDM)	w (wCDM)
DES Y1	$0.260^{+0.065}_{-0.037}$	$0.782^{+0.027}_{-0.027}$	$-0.95^{+0.33}_{-0.39}$
DES Y3	$0.290^{+0.039}_{-0.063}$	$0.759^{+0.023}_{-0.025}$	$-0.98^{+0.32}_{-0.20}$
HSC Y1	$0.332^{+0.050}_{-0.096}$	$0.823^{+0.032}_{-0.028}$	/
HSC Y3	$0.256^{+0.056}_{-0.044}$	$0.769^{+0.031}_{-0.034}$	/

Table 1.2: *Cosmological parameters estimations performed in DES Y1 (Troxel et al., 2018), DES Y3 (Secco et al. (2022), Amon et al. (2022)), HSC Y1 (Hamana et al., 2020) and HSC Y3 (Sugiyama et al., 2023) at 68% CI. The constraints on Ω_m and S_8 are done considering fiducial ΛCDM model, while w is estimated for wCDM.*

For the wCDM model (where w is allowed to vary), DES found $w = -0.95^{+0.33}_{-0.39}$ in Y1 and $w = -0.98^{+0.32}_{-0.20}$ in Y3 (Abbott et al., 2022). The conclusion is the same as above, the constraints on w and its uncertainty have not been significantly improved between Y1 and Y3. The wCDM model was also tested in HSC Y1 analysis, but their cosmic shear 2PCFs alone did not provide any useful constraints. Moreover, no dark energy measurements were carried out in the Y3 analysis.
Figure 1.18 shows the constraints on Ω_m, σ_8 and S_8 from the HSC Y3 results.
The prior on the shear bias (see section 3.3.3) is up to 1% in HSC Y1 and Y3, and a bit more than 1% in DES Y1 and Y3.

Both DES and HSC suffer from shear calibration issues, including PSF modeling (which represents the response of the imaging system to a point source, see section 3.2), and from photometric redshift uncertainties. Especially in HSC Y3, the two last redshift bins are left free in the fit (using large priors for their uncertainty) because of photometric redshift issues. The fitted central value measured from galaxies in those bins is very different from the expected value, leading to a high uncertainty ($\Delta z \sim 0.1$, while it is more around 0.01 and 0.02 in DES). Even if calibrations using spectroscopic redshifts were performed in both of these analyses, some systematics remain.

Even if cosmological constraints with cosmic shear are progressing, they still face challenges and difficulties, which need to be controlled for next generation surveys analyses.
Some goals are to be achieved to ensure better constraints with cosmic shear :

- To lower the bias on shear estimation from 1% to 0.1% by improving shape measurement and calibration algorithms (section 4) and correct bias introduced by the presence of shot noise in the images (section 6),
- Refine the accuracy of PSF models from 0.3% to 0.1% by taking more account of physical effects in the PSF modeling (the PIFF package by Jarvis et al. (2021) could be a solution),
- To achieve a better accuracy in photometric redshifts measurements (lower the systematic uncertainty to 0.001) through more spectroscopic calibrations.

In the next two chapters, we will develop the gravitational lensing (and cosmic shear) formalism, the challenges we face when measuring galaxy shapes, and all the sources of bias affecting shear estimations.

2

Gravitational lensing

Contents

2.1 Introduction

The first calculation of the deflection of a light ray by the attraction of a celestial body was done in 1801 (and published in 1804) by Johann Georg von Soldner (Soldner, 1921).

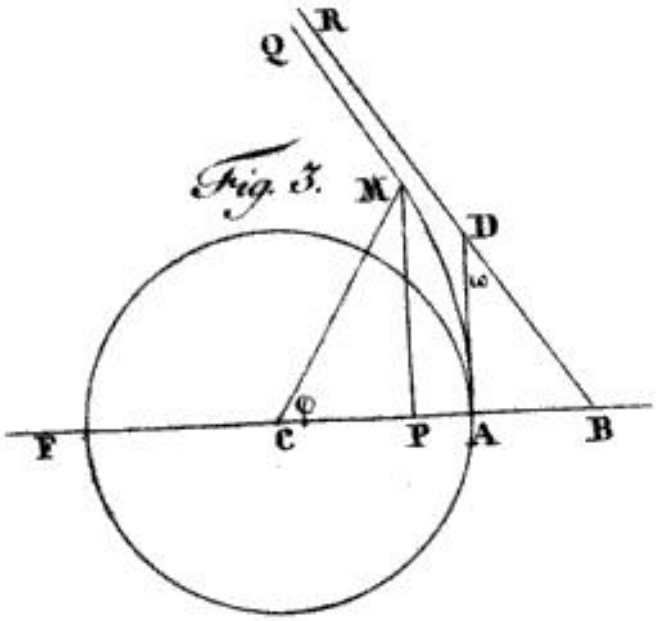

Figure 2.1: *Deflection of light rays passing close to a massive body (Johann Georg von Soldner)*

Only using the equivalence principle, Einstein calculated the same value as Soldner in 1911. He revised however his calculation in 1915 while developing his theory of general relativity, realizing he missed half of the correct value. The "gravitational lens" denomination was also introduced by Einstein but in 1936, when he published his work about light deflection.

Then, the first direct observation of light rays deflection was done a few years later by Arthur Eddington. To test Einstein's prediction of general relativity, he decided to conduct an experiment during the eclipse of May 29th 1919 to observe the deflection of starlight by the Sun. At the end of the experiment, he found that the observed cluster (the Hyades cluster, made up of 300 to 400 stars) was offset by 1.75 arcseconds from its usual position (Eddington, 1919), the value predicted by Einstein for light rays grazing the surface of sun.
In 1924, Orest Khvolson published an article about gravitational lenses mentioning the "halo effect" we can observe when the source and the lens are perfectly aligned along the line of sight from an observer point of view (Chwolson, 1924). This effect is now known as the Einstein ring.

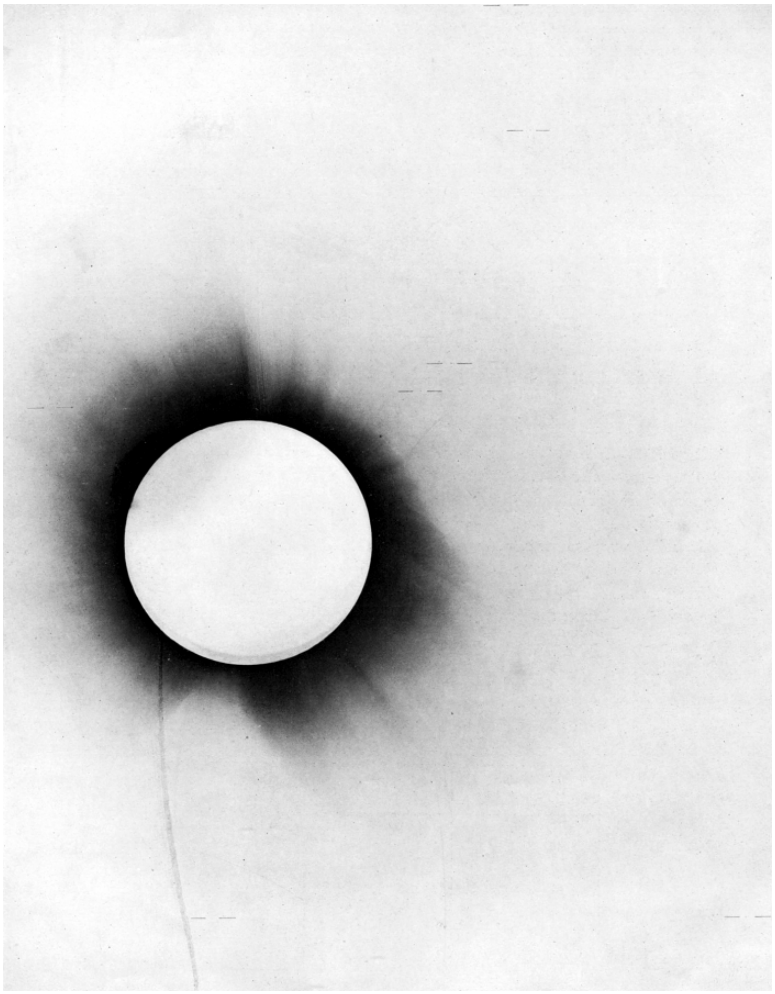

Figure 2.2: *Photograph taken by Eddington during the 1919's eclipse*

Following Einstein's work, and after the discovery that the observed "nebulae" were actually galaxies, Fritz Zwicky was the first to consider the hypothesis that galaxies could act as gravitational lenses, given their size and mass (Zwicky, 1937).

After another hypothesis formulated independently in 1963 by Klimov, Liebes and Refsdal that quasars could be a great light source for gravitational lensing (Klimov (1963), Liebes (1964), Refsdal (1964)), the first object detected thanks to the effect of gravitational lensing was the "Twin QSO" in 1979. It is a quasar whose image is doubled by the effect of the foreground galaxy YGKOW G1 gravitational potential (see figure 2.3). The first observation of an object lensed by a galaxy cluster was performed by Genevieve Soucail and her team at the Toulouse observatory in 1987 (Soucail et al., 1987). In the picture presented in their article, we can see a blue arc near the Abell 370 cluster, reminiscent of a gravitational lensing effect (see figure 2.4). This image represent what is known as a "strong lensing" effect, when the distortion is visible to the naked eye. However, most of the gravitational lensing effects are coherent, not visible (very faint) and require statistical detection, that is what we call the "weak lensing" regime (more details are given in section 2.3).

Figure 2.3: *Twin quasar (two blue images) lensed by YGKOW G1 (yellow spot in the middle), credit : ESA/Hubble & NASA*

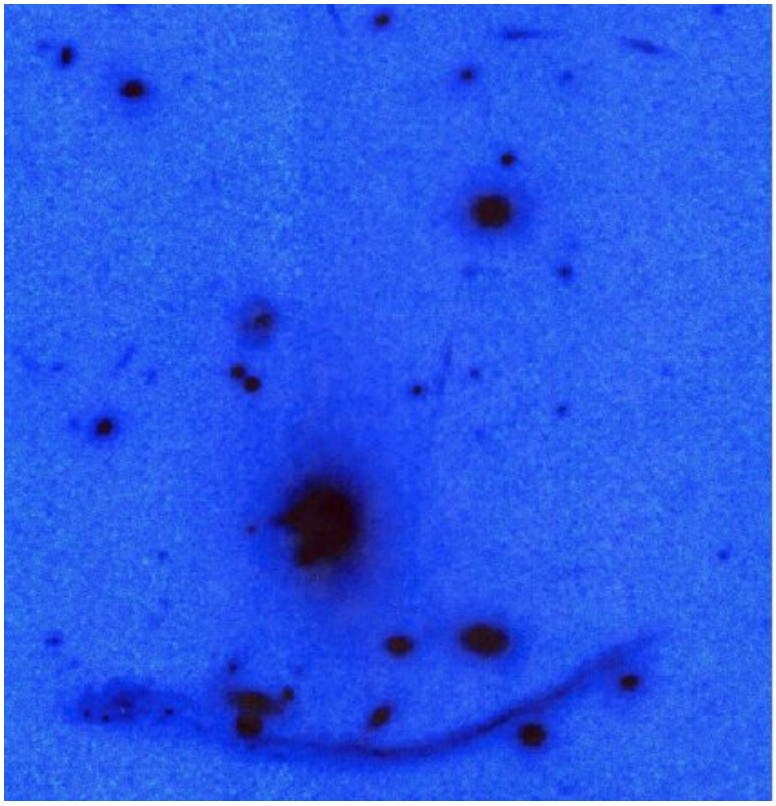

Figure 2.4: *First lensing observation on a galaxy cluster (Abell 370)*

It will take until the 90s to observe the coherent alignment of background galaxies from the Deep CCD Field Surveys centered on foreground clusters, recognized as the first weak lensing detection (Tyson, 1990). The existence of weak gravitational shear by large-scale structures (by measuring coherent galaxy distortions) was demonstrated in the 2000s (Bacon, Refregier, and Ellis (2000), Kaiser, Wilson, and Luppino (2000), Van Waerbeke et al. (2000), Wittman et al. (2000)).
The weak lensing was more recently studied with several surveys such as KiDS (*The Kilo-Degree Survey*, Hildebrandt et al. (2017)), DES (*The Dark Energy Survey*, Troxel et al. (2018)) and Subaru (Hamana et al., 2020).

The study of weak lensing will take a new turn with the arrival of data from Euclid and LSST, next-generation surveys ushering in the era of precision cosmology (more details about LSST are given in section 3.3.1).

2.2 Light deflection by a gravitational field

In this section, we will describe how light rays behave passing through the gravitational potential of massive bodies. The deflection of light can be described in many ways, taking different approximations and assumptions. We will first develop the theory of light deflection in a general way, then explain the linearization of these equations in the case of weak lensing, and then finish with a description of cosmic shear.

2.2.1 The deflection angle

According to General Relativity, photons propagate along null geodesics in the universe. In the perturbed Minkowski metric, the light ray travel time can be expressed as :

$$t = \frac{1}{c}\int (1 - \frac{2\Phi}{c^2}) dr \tag{2.1}$$

integrating along the light path in physical coordinates dr. The gravitational potential Φ is negative because of its normalization chosen such as it vanishes at infinity.
Because a gravitational potential acts like a propagation medium (in the optical sense), we can define its *refraction index* :

$$n = 1 - \frac{2\Phi}{c^2} \tag{2.2}$$

We can now apply the *Fermat's principle* which ensures that a light ray always takes the path between two points where the optical path τ is minimal :

$$\delta\tau = \delta \int_A^B \frac{c}{n} dt = 0 \tag{2.3}$$

Given these equations, integrating 2.1 along the light path directly leads to the deflection angle :

$$\hat{\boldsymbol{\alpha}} = -\frac{2}{c^2}\int \boldsymbol{\nabla}_\perp \Phi dr \tag{2.4}$$

which is the gradient of the potential taken perpendicular to the light path. This is twice the classical prediction in Newtonian dynamics because there are equal perturbations in both temporal and spatial components in the perturbed Minkowski metric. This deflection angle depends on the mass distribution of the lens and on the impact parameter of the source.

Assuming that typical deflection angles are small (the order of the arc second or less), we can use the *Born approximation* and take the integration path as a straight line. Considering a light ray propagating along the z axis and passing a lens with a mass M with an impact parameter ξ (see figure 2.5), we can integrate the deflection angle :

$$\hat{\alpha} = -\frac{2}{c^2}\frac{\partial}{\partial \xi}\int dz \frac{\mathcal{G}M}{\sqrt{\xi^2 + z^2}} = \frac{4\mathcal{G}M}{\xi c^2} \tag{2.5}$$

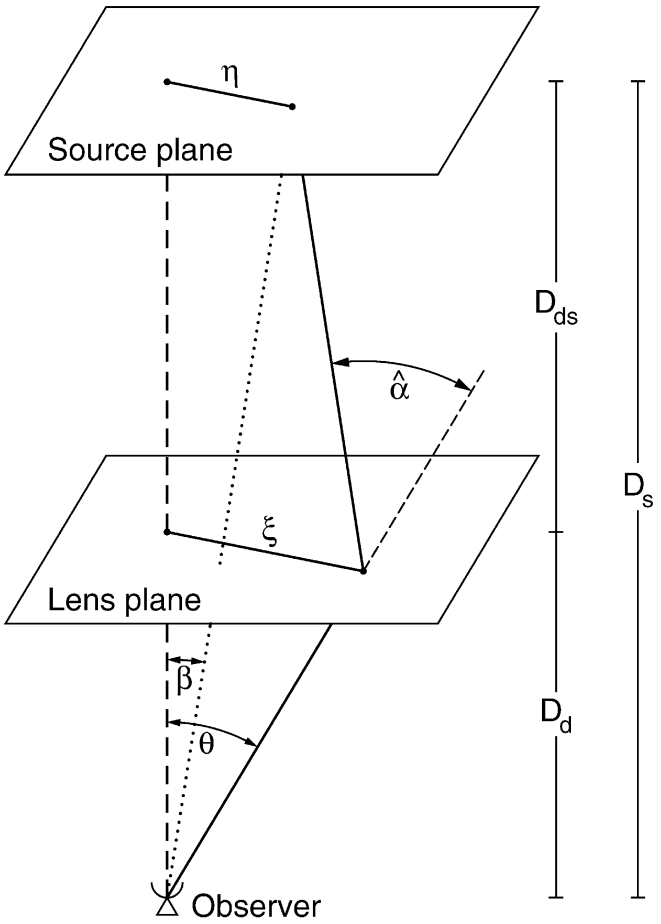

Figure 2.5: *Gravitational lens system from Bartelmann and Schneider (2001)*

2.2.2 The lens equation

We may now wonder how to rely the true position of a source and its observed position on the sky. The figure 2.5 shows a gravitational-lens system, where β is the angle between the source and the optical axis, θ the angle between the optical axis and the image, η the two-dimensional position of the source and ξ the impact parameter of the lens. The source and lens plans are perpendicular to the line of sight which connects the observer and the source.
We have :

$$D_S\boldsymbol{\beta} = D_S\boldsymbol{\theta} - D_{DS}\hat{\boldsymbol{\alpha}} \tag{2.6}$$

Note that this equation holds because D_S and D_{DS} are *angular diameter distances* (defined in 1.4.1), which are defined in a way that the Euclidean intercept theorem (also known as Thales theorem) remains true in a curved space-time.
We can introduce the reduced deflection angle :

$$\boldsymbol{\alpha} = \frac{D_{DS}}{D_S}\hat{\boldsymbol{\alpha}} \tag{2.7}$$

and then define the *lens equation* :

$$\boldsymbol{\beta} = \boldsymbol{\theta} - \boldsymbol{\alpha} \tag{2.8}$$

We can interpret this equation in the following manner : by satisfying the lens equation, an observer will see a source with a true position $\boldsymbol{\beta}$ at angular position $\boldsymbol{\theta}$. If the lens equation has more than one solution for a fixed β, the lens will produce several observed images of the source. That last effect occurs in the case of "strong" lensing.

2.2.3 The lensing potential

We assume the *thin lens* approximation, so all the distances involved in the system (D_D, D_S and D_{DS}) are considered far greater than the thickness of the lens. This assumption holds in real-life conditions : the size of a cluster is typically of the order of Mpc, while the distances considered between an observer, a source and a lens are of the order of Gpc.

According to equation 2.4, the reduced deflection angle can be rewritten as a gradient of a 2D potential :

$$\boldsymbol{\alpha} = \boldsymbol{\nabla}_\perp \left[\frac{2}{c^2}\frac{D_{DS}}{D_S}\int \Phi dz \right] \tag{2.9}$$

taking a light ray that propagates parallel along the z axis and integrating over the lens depth.
It is convenient to introduce quantities as functions of the angular position on the celestial sphere to describe gravitational lensing, because one actually measures angles on the sky.
We can replace $\boldsymbol{\nabla}_\perp$ by $\boldsymbol{\nabla}_\theta$ thanks to a change of variable :

$$\boldsymbol{\nabla}_\perp = D_D^{-1}\boldsymbol{\nabla}_\theta \tag{2.10}$$

In the small-angle approximation, the perpendicular separation from the line of sight is $D_D\theta$.
We can then re-express the reduced deflection angle from equation 2.9 to :

$$\boldsymbol{\alpha} = \boldsymbol{\nabla}_\theta \Psi \tag{2.11}$$

where Ψ is the *lensing potential* :

$$\Psi = \frac{2}{c^2}\frac{D_{DS}}{D_D D_S}\int \Phi dz \tag{2.12}$$

Most of the imaging properties of gravitational lenses are contained in the lensing potential.

While considering the cosmic shear regime, we are not anymore in the case of one thin lens distorting the background galaxy shape. The lensing potential is now caused by an ensemble of large-scale structures, equations 2.9 and 2.12 should be rewritten as follows :

$$\boldsymbol{\alpha} = \boldsymbol{\nabla}_\perp \left[\frac{2}{c^2}\int \frac{D_{DS}}{D_S}\Phi dz\right] \tag{2.13}$$

$$\Psi = \frac{2}{c^2}\int \frac{D_{DS}}{D_D D_S}\Phi dz \tag{2.14}$$

as we also integrate the distances over redshift.

The next section introduces in detail the weak lensing formalism, and we will then use the deflection angle and the potential as defined in equations 2.13 and 2.14.

2.3 Weak lensing

2.3.1 Linearised approximation : the amplification matrix

We can locally linearise the lens mapping when the gravitational potential is weak, i.e. $\frac{\Phi}{c^2} \ll 1$.
Given the lensing potential, the lens equation can be rewritten as follows :

$$\boldsymbol{\beta} = \boldsymbol{\theta} - \boldsymbol{\nabla}_\theta \Psi \tag{2.15}$$

and its Taylor expansion gives :

$$\delta\boldsymbol{\beta} \simeq \boldsymbol{A}\delta\boldsymbol{\theta} \tag{2.16}$$

where A is the inverse amplification matrix, a Jacobian matrix that describes the mapping between the lensed coordinates θ of the image and the unlensed coordinates β of the source.

$$A_{ij} = \frac{\partial\beta_i}{\partial\theta_i} = \delta_{ij} - \psi_{ij} \tag{2.17}$$

where the potential derivatives are taken at the center of the image.

$$\psi_{ij} = \frac{\partial^2\Psi}{\partial\theta_i\partial\theta_j} \tag{2.18}$$

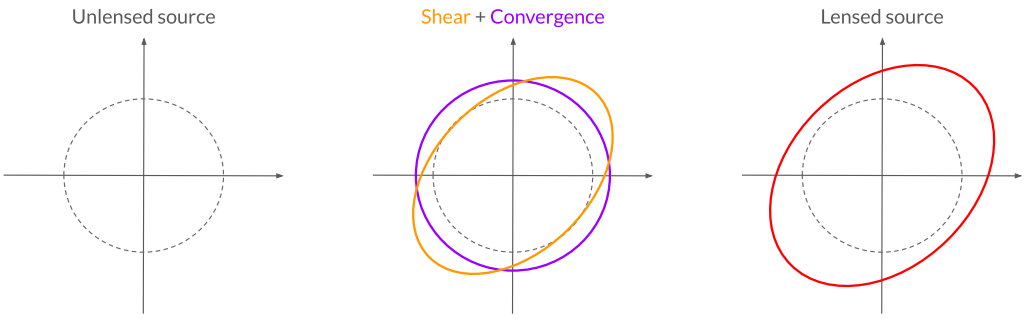

Figure 2.6: *Shear and convergence effect on a lensed source.*

The physical interpretation of the matrix A can be seen as the linear approximation of the image distortion introduced by lensing. We can give another definition of A in terms of the shear components and the *convergence* κ (an isotropic magnification of the source) :

$$A = \begin{pmatrix} 1 - \kappa + \gamma_1 & \gamma_2 \\ \gamma_2 & 1 - \kappa - \gamma_1 \end{pmatrix} \tag{2.19}$$

where κ and the shear are defined as second derivatives of the potential Ψ :

$$\kappa = \frac{1}{2}(\psi_{11} + \psi_{22}) \tag{2.20}$$

$$\gamma_1 = \frac{1}{2}(\psi_{11} - \psi_{22}) \tag{2.21}$$

$$\gamma_2 = \psi_{12} \tag{2.22}$$

The shear is more generally defined as :

$$\gamma_i = \gamma e^{2i\phi} \tag{2.23}$$

with $\gamma = \gamma_1 + i\gamma_2$ and ϕ being the orientation of the galaxy major axis. An example of γ_1 and γ_2 is given in figure 2.7. The distortion applied to an ellipse by the shear is invariant by a rotation of 180° (or π), making the shear a spin 2 quantity. A schematization of shear distortion and convergence is given in figure 2.6.

In the weak lensing limit, and especially considering lensing by large-scale structures (cosmic shear), the distortion applied in images is very weak, and we consider that we can factor out $(1 - \kappa)$, as it only affects the size of the source but not the shape. We can then define another convention for the shear, called the *reduced shear*:

$$g = \frac{\gamma}{1 - \kappa} \tag{2.24}$$

which has the same distortion properties as γ.

The shear is an interesting quantity because it is statistically observable: on average, galaxies are circular, unless some distortion elongates them locally in a coherent way. All shear indicators rely on some measure of the apparent galaxy ellipticity. On the other hand, convergence alters apparent brightness and size, and is in general not measurable, in particular in the weak lensing regime, because unlensed observables are unknown. However, convergence and shear fields are related and we now detail the relation between convergence field and lenses.

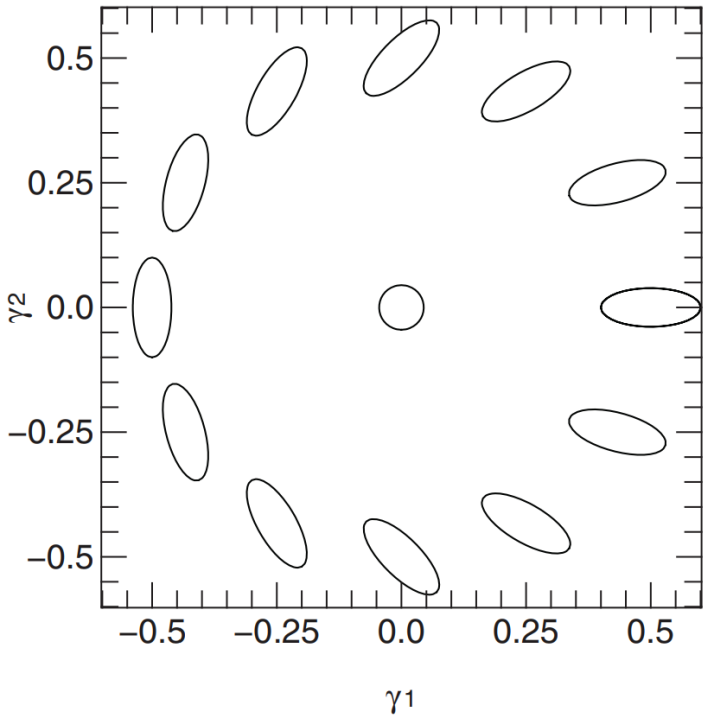

Figure 2.7: *Ellipticity distortion as a function of γ_1 and γ_2. Source : Martin Kilbinger (Kilbinger, 2015)*

2.3.2 Convergence

The distortion of light rays due to weak lensing can be expressed through the convergence κ. We can define κ through the divergence of the reduced deflection angle:

$$\kappa = \frac{1}{2}\boldsymbol{\nabla}_\theta \boldsymbol{\alpha} \tag{2.25}$$

It is also related to the lensing potential through equation 2.20. Invoking Poisson's equation :

$$\boldsymbol{\nabla}_{\boldsymbol{\theta}}{}^2\psi = 4\pi\mathcal{G}a^2\rho\delta \tag{2.26}$$

where δ represents the dimensionless *density contrast*, which describes local relative density variations.

We can calculate the Laplacian of ψ :

$$\begin{aligned}\boldsymbol{\nabla}_\theta \boldsymbol{\alpha} = \boldsymbol{\nabla}_\theta^2 \psi &= \frac{2}{c^2}\int a^2\delta \frac{D_D D_{DS}}{D_S}\boldsymbol{\nabla}_\perp \Phi dD_S \\ &= \frac{8\pi\mathcal{G}}{c^2}\int \frac{D_D D_{DS}}{D_S}\rho dD_S\end{aligned} \tag{2.27}$$

that leads naturally to the convergence :

$$\kappa = \frac{4\pi\mathcal{G}}{c^2}\int a^2\delta\frac{D_D D_{DS}}{D_S}\rho dD_S \tag{2.28}$$

Note that ρ is not the entire mass density, but its fluctuation around its cosmological mean value $\overline{\rho}$ (identical to the critical density 1.32 in case of a flat universe). We can describe the relation between these two quantities and the density contrast : $\rho = \overline{\rho}(\delta + 1)$. We can define $\overline{\rho}$ in terms of the cosmological parameters :

$$\begin{aligned}\overline{\rho} &= \frac{3H_0^2}{8\pi\mathcal{G}}\Omega_m a^{-3} \\ &= \overline{\rho}_0 a^{-3}\end{aligned} \tag{2.29}$$

By inserting 2.29 into the definition of the convergence, we can re-express κ as follows:

$$\kappa(z) = \frac{3}{2}\left(\frac{H_0}{c}\right)^2 \Omega_m \int \frac{\delta}{a}\frac{D_D D_{DS}}{D_S}dD_S \tag{2.30}$$

The relation between convergence and density contrast is essential for understanding structure evolution. In order to get the mean convergence of multiple sources, we have to average the equation 2.30 over the source galaxy distribution $n(z)$:

$$K = \int_0^{z_{lim}} n(z)\kappa(z)dz \tag{2.31}$$

where $n(z)$ is obtained with photometric redshifts and z_{lim} is the limiting redshift of the galaxy sample. It is worth noting that $\int n(z)dz = 1$.

By going into Fourier space, and using the equations 2.20, 2.21 and 2.22, it is possible to link the shear and convergence statistics :

$$\tilde{\gamma_1}(\boldsymbol{\ell}) = \frac{\ell_1^2 - \ell_2^2}{\ell^2}\tilde{\kappa}(\boldsymbol{\ell}) \tag{2.32}$$

$$\tilde{\gamma_2}(\boldsymbol{\ell}) = \frac{2\ell_1\ell_2}{\ell^2}\tilde{\kappa}(\boldsymbol{\ell}) \tag{2.33}$$

which leads to :

$$\tilde{\gamma_1}^2(\boldsymbol{\ell}) + \tilde{\gamma_2}^2(\boldsymbol{\ell}) = \tilde{\kappa}^2(\boldsymbol{\ell}) \tag{2.34}$$

This equation shows the relation between shear and convergence power spectra, which is essential to link the lensing effect to the cosmological parameters (see section 2.3.4).

2.3.3 Power spectrum and correlation function

The two-point correlation function (2PCF) of the convergence is given by :

$$\langle \kappa(\zeta)\kappa(\zeta+\theta)\rangle \tag{2.35}$$

where ζ is the angular position.
Assuming that the convergence complies to the homogeneity and isotropy principles, the 2PCF is considered invariant under translation and rotation. In Fourier space, the 2PCF is linked to the convergence power spectrum P_κ with :

$$\langle \widetilde{\kappa}(\ell)\widetilde{\kappa}^*(\ell')\rangle = (2\pi)^2\delta_D(\ell-\ell')P_\kappa(\ell) \tag{2.36}$$

with δ_D the Dirac delta function and ℓ the 2D wave vector (Fourier conjugate of θ). The density power spectrum P_δ is given by the square of equation 2.30 in Fourier space. We can then write P_κ in terms of P_δ :

$$P_\kappa(\ell) = \frac{9}{4}\Omega_m^2\left(\frac{H_0}{c}\right)^4 \int_0^{z_{lim}} \frac{q^2(z)}{a^2(z)} P_\delta\left(\ell, z\right) dz \tag{2.37}$$

where q is the *lensing efficiency function* :

$$q(z) = \int_z^{z_{lim}} n(z_D)\frac{D_D - D_S}{D_D} dz_D \tag{2.38}$$

where z_D means that we look at redshifts between the observer and the lens.

We can decompose the shear field into a gradient part (E-mode) and a curl part (B-mode). At first order, gravitational lensing is only inducing E-mode power, and detecting B-modes or mixes of E and B-modes is a sign of systematics (note that not all systematics cause B-modes). These B-modes can be caused by several sources : higher order terms in relation between shear and reduced shear or shape estimator (Krause and Hirata, 2010), selection bias (Wyithe, Winn, and Rusin, 2003), intrinsic alignment (Crittenden et al., 2002) or PSF correction residuals. The last three effects are described in more details in section 3.3.3.

In order to understand correlations between two sources affected by the same lens, we need to define the shear two-point correlation function. This quantity gives the average shear effect between two points as a function of the angular distance between those two points. It is directly related to the convergence power spectrum through the integral :

$$\xi_\pm(\theta) = \frac{1}{2\pi}\int d\ell\ell J_{0/4}(\ell\theta)P_\kappa(\ell) \tag{2.39}$$

where J_n is the n-th order Bessel function of the first kind.

We saw earlier that the shear is a two component quantity (see equations 2.21 and 2.22), and it is convenient to define them into a *tangential* and a *cross* component:

$$\begin{aligned}\gamma_t &= -\Re(\gamma e^{-2i\phi}) \\ &= -\gamma_1\end{aligned} \tag{2.40}$$

$$\begin{aligned}\gamma_\times &= -\Im(\gamma e^{-2i\phi}) \\ &= -\gamma_2\end{aligned} \tag{2.41}$$

where ϕ represents the resulting elliptical image's major axis orientation, and the second equality in each equation represents the special case where $\phi = 0$. The cross-component is obtained by a rotation of $+\pi/4$ with respect to the tangential component.
We can then define three two-point correlators from these new shear components : $\langle\gamma_t\gamma_t\rangle$, $\langle\gamma_\times\gamma_\times\rangle$ and $\langle\gamma_t\gamma_\times\rangle$. Because of the assumption of a parity-symmetric universe, the shear field is statistically invariant under a mirror transformation, therefore the $\langle\gamma_t\gamma_\times\rangle$ term vanishes. Measuring $\langle\gamma_t\gamma_\times\rangle$ not consistent with zero is a sign of systematic errors.

The two components of the shear 2PCF are defined as :

$$\xi_+(\theta) = \langle\gamma_t\gamma_t\rangle(\theta) + \langle\gamma_\times\gamma_\times\rangle(\theta) \tag{2.42}$$

$$\xi_-(\theta) = \langle\gamma_t\gamma_t\rangle(\theta) - \langle\gamma_\times\gamma_\times\rangle(\theta) \tag{2.43}$$

The shear 2PCF can be estimated using galaxy ellipticities, and is linked to cosmology through its relation with the convergence power spectrum (see equation 2.39).

2.3.4 Relation between cosmic shear and cosmological parameters

The shear two-point correlation functions are sensitive to the cosmological parameters through their relation to the convergence. We see that the distances and the universe's matter content are linked in equation 2.28. Because the density contrast δ allows to describe the matter density fluctuations and their evolution with redshift, it can be used to predict the rate of structure evolution in general relativity.
Therefore, the relation between the universe's geometry and its content predicted by general relativity can be tested using the cosmic shear dual sensitivity to both distance and matter distribution.
To constrain dark energy through cosmic shear, we need to study the evolution of observables with redshift. Hence, we need to perform tomographic analyses by measuring the cosmic shear 2PCF at different photometric redshift bins.

Figure 2.8 shows the shear 2PCFs of HSC Y3 shear analysis (Li et al., 2023), where all the redshift bins' auto and cross-correlations are included. The cross-correlations provide information because the distortions applied to the ellipticities of galaxies located at different z on the line of sight are correlated by the matter located between the nearest galaxy and us.
We see that these 2PCFs values increase with the redshift, which is expected because the lensing effect is higher when photons travel through more matter. Small angular

scales are removed because of strong non-linearities in the density contrast evolution, and the large scales are also removed because significant B-modes were found in $\xi_{\pm}$.

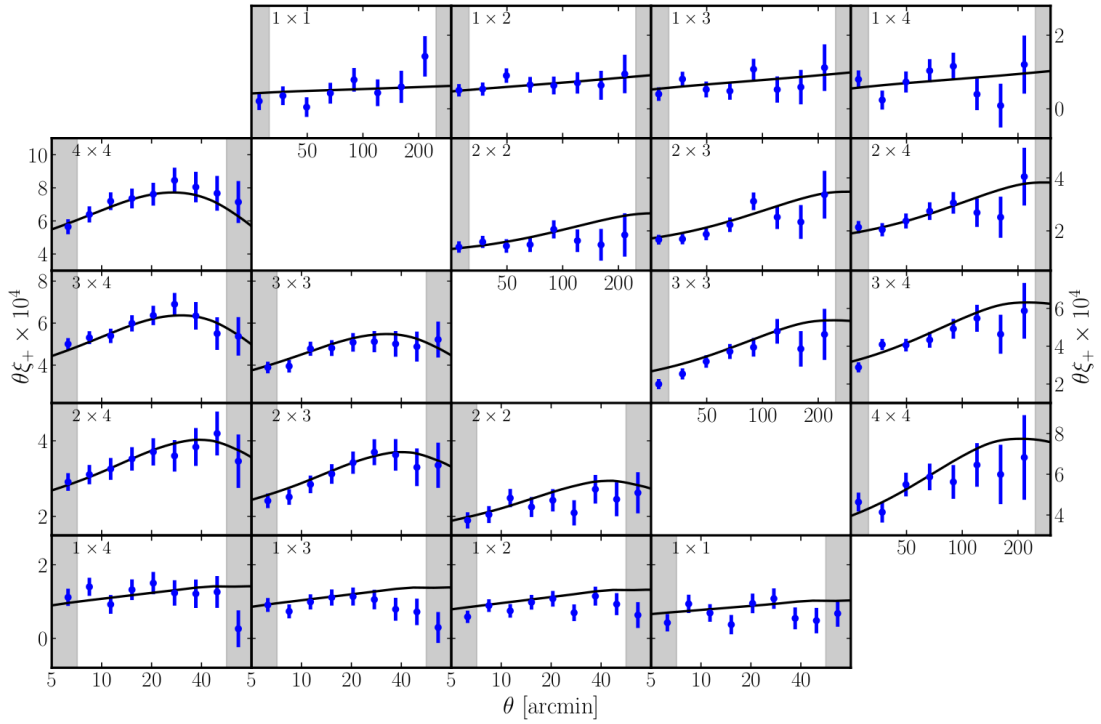

Figure 2.8: *Shear two-point correlation functions (blue dots) and their best-fit model (black solid lines) in HSC Y3 analysis, multiplied by the angular separation θ (in arcmin). The $\theta\xi+$ are displayed in lower left half, and $\theta\xi-$ in upper right half. Auto and cross-correlations are represented for the four redshift bins (labeled 1-4 on each figure's upper left corner).*

As we are measuring the effect of cosmic shear on background galaxy ellipticities, it is therefore important to understand their nature and characteristics. The next chapter is focused on the challenges of shape and shear measurement, and its first section gives a summarized overview of galaxy properties.

3

Challenges of shape measurement

Contents

3.1 Galaxies

3.1.1 Introduction

A galaxy is a cosmic gravitational system composed of stars, gaz, interstellar dust and dark matter for the most part. Most of the time, its content revolves around a central supermassive black hole, the first one directly observed being M87* at the center of Messier 87 in 2019 (Event Horizon Telescope Collaboration et al., 2019). Then the supermassive black hole Sagittarius A*, located in the center of our galaxy, the Milky Way, was observed in 2022 (Akiyama and Event Horizon Telescope Collaboration (2022), see figure 3.1). This black hole (at least the center of the galaxy, always more massive than the periphery) represents its center of rotation and sometimes of symmetry, especially for elliptical galaxies that can be described using *isophotes* (more details in section 3.1.3).

Through the effect of gravitation, galaxies can gather in larger structures such as groups, clusters or superclusters.

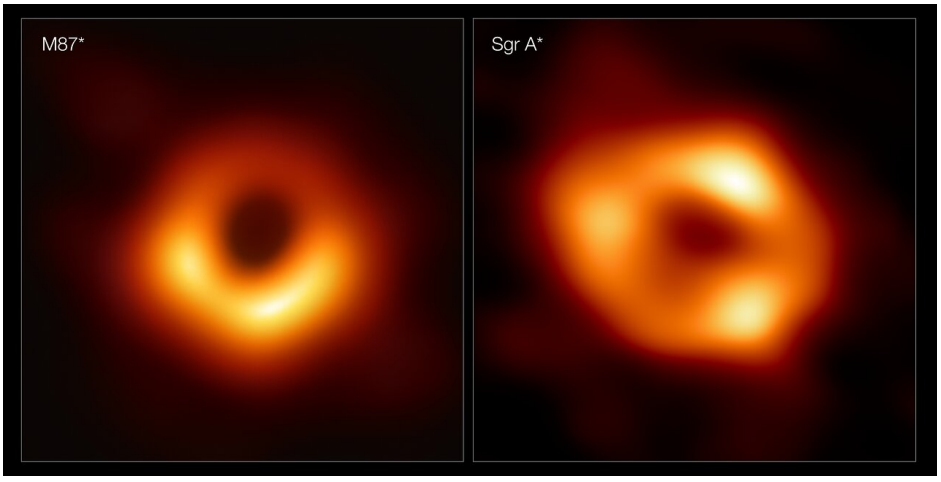

Figure 3.1: *Supermassive black holes : M87* and Sagittarius A* (Source : ESO).*

The first mention of galaxy-like objects was originally formulated by Emmanuel Kant in 1755 suggesting that nebulae were rotating systems, flattened by gravity and creating stars. The first observations of galaxies as stellar systems date back to 1914 (Slipher, 1914), but their discovery is generally attributed to Edwin Hubble, thanks to images taken by the Hooker telescope in the 1920s. He demonstrated that nebulae previously observed by other telescopes were not in fact objects belonging to the Milky Way, but are systems located outside of it. He went on to describe their three main morphological types (see section 3.1.3).

3.1.2 Properties

3.1.2.a Ellipticity

From an observer's point of view, the assessment of a galaxy's degree of roundness (or sphericity) is what we call its ellipticity. We assume these observed shapes to be randomly distributed in the Universe, as nothing indicates that galaxies should have a preferred ellipticity nor orientation. This is actually not exactly true : when galaxies evolve in the same gravitational environment, it creates a spatial correlation in their orientation and therefore a correlation in their shape. This effect, inherent in galaxies' formation and evolution, is called *intrinsic alignment*. It only correlates galaxies at small scales, both on the sky and in redshift.

3.1.2.b Color and magnitude

The colors of a galaxy are mainly due to the type of stars it contains. We can also define the absolute magnitude, which represents the intrinsic luminosity of a celestial object. A diagram showing the relation between galaxies' color and luminosity using the DR7 catalog of the Sloan Digital Sky Survey (SDSS) is given in figure 3.2. Such a diagram provides information on the distribution of galaxies according to their mass or age (Gavazzi et al., 2010). The more luminous a galaxy, the greater its mass, and the redder the older. More generally, the magnitude and color of galaxies depend on their stage of evolution, and obviously on their redshifts.

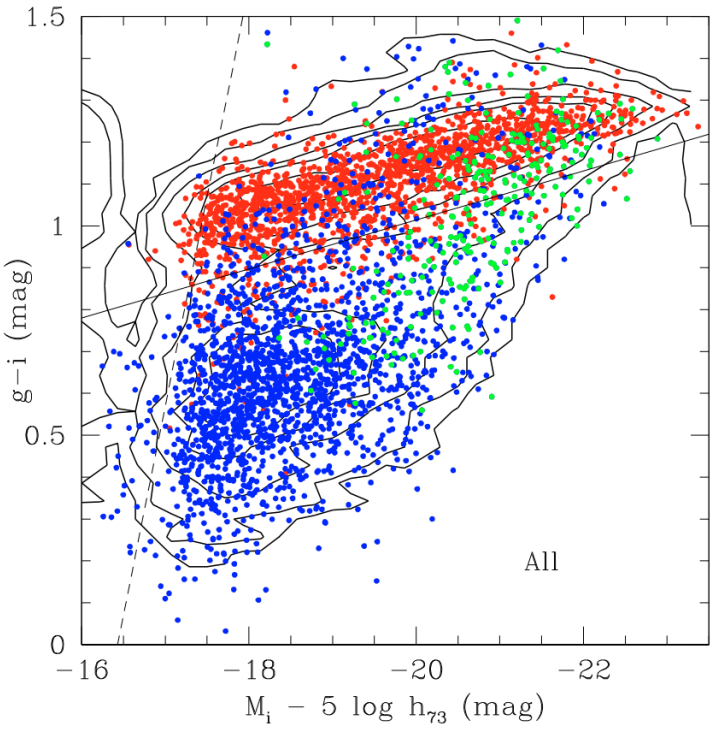

Figure 3.2: *Color (from bluer to redder) versus absolute magnitude (from fainter to brighter) relation of all galaxies in the Coma Supercluster coded according to Hubble type : red = early-type galaxies, blue = disk galaxies, green = bulge galaxies.*

3.1.2.c Rotation

On the basis of Newtonian mechanics and Keplerian dynamics, we can expect the mean orbital velocity of an object located at a given distance from the majority of mass distributions to decrease in inverse proportion to the square root of the orbit radius. This is also what was expected for the rotation of a galaxy's arms around its center. However, observations done at the end of the 1970s using the 21cm hydrogen-line, among others Morton S. Roberts (Roberts, 1966) and Vera C. Rubin (Rubin, 1983), have produced different and somewhat surprising results. Instead of decreasing as a function of the inverse square root of the distance from the center, the rotation curves shows that the velocity is almost constant as a function of radius (see figure 3.3). These results supported Zwicky's initial hypothesis about the presence of "extra mass" in galaxies (Zwicky, 1933), now known as dark matter (see section 1.5).

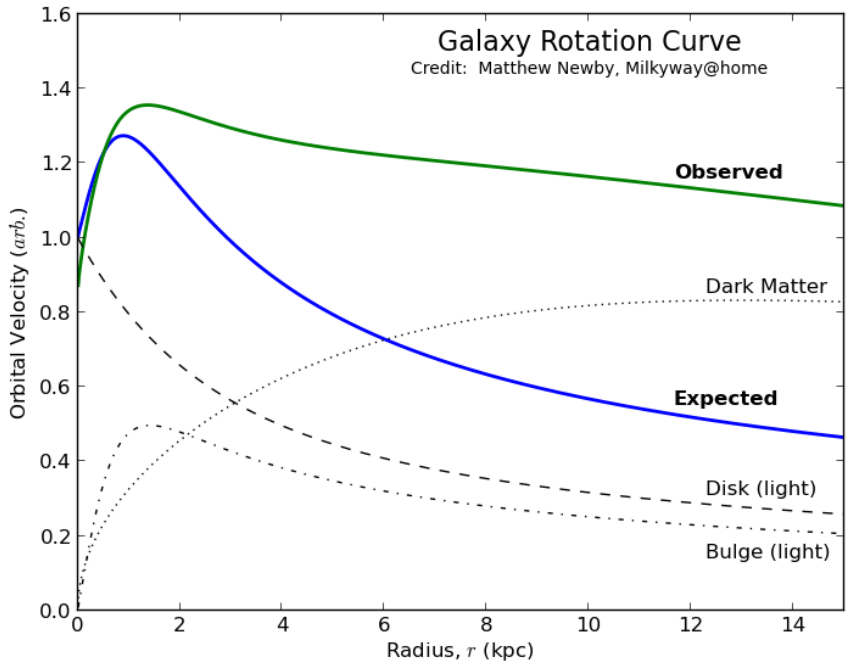

Figure 3.3: *Galaxy (Milky Way) rotation curve*

3.1.3 Classification

As introduced in section 3.1.1, Hubble proposed in 1926 a classification of galaxies into three main categories: elliptical (E), spiral (crossed SB or not S) and irregular (Hubble, 1926). A revised version of this classification was established in 1959 by Gérard de Vaucouleurs taking into account more subtle characteristics, and introducing intermediate galaxy categories (such as lenticular galaxies). The figure 3.4 shows this classification.

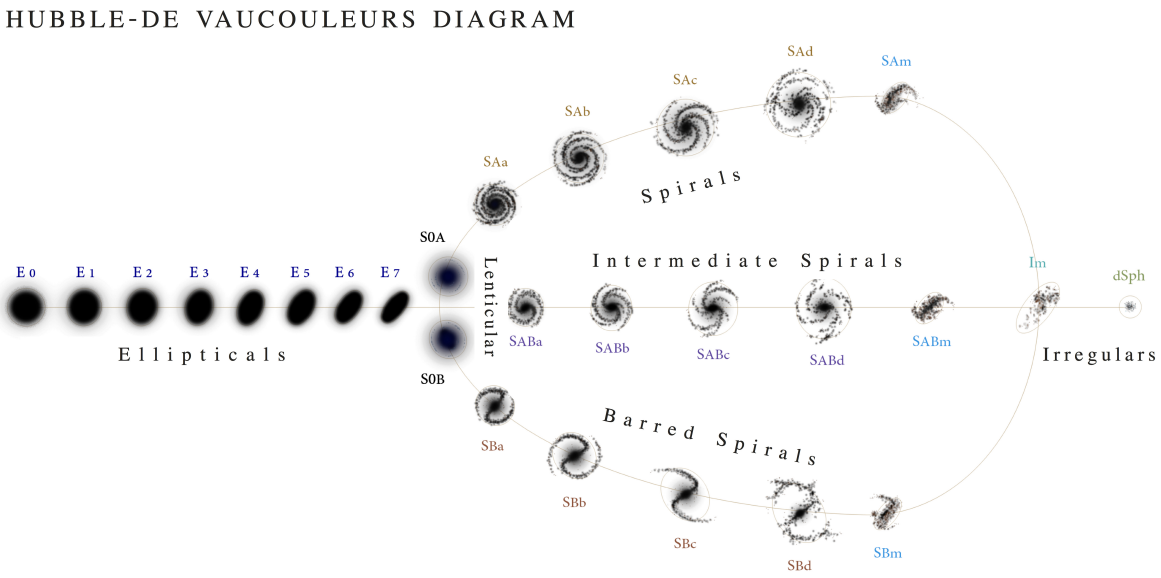

Figure 3.4: *Hubble - de Vaucouleurs galaxy classification*

In general, the different types of galaxies present in this classification correspond to precise characteristics and stages of development :

- **Elliptical** : contain a rather old population of stars and very little gas or dust. They usually correspond to the redder and the older galaxies.

  Elliptical galaxies' are characterized by three axes (see figure 3.5), and their shape can be described using the ratios of their lengths : let us call L_x the length of an axis (with $x = l,i$ or s for long, intermediate and short respectively), the shape is *oblate* if $L_l = L_i < L_s$, *prolate* if $L_l = L_i > L_s$ and *triaxial* if $L_l \neq L_i \neq L_s$. In this last case, the observed isophotes (lines connecting points of the same luminous intensity) can appear rotated from their true orientation. This effect is called "isophote twisting" (see figure 3.5). But in practice, it is not possible to distinguish if we observe a true or a twisted luminosity profile.

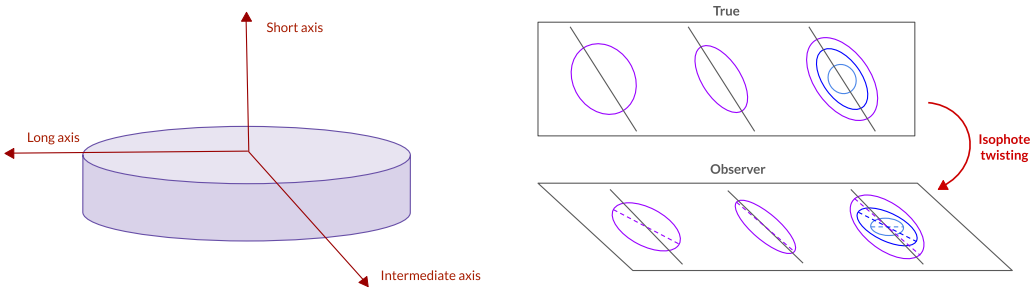

Figure 3.5: *Left : Three axis characterizing shapes of elliptical galaxies. Right : Isophote twisting seen by an observer, in case of triaxial galaxy.*

- **Spiral** : contain large quantities of gas and dust concentrated in their disc. The older stars are located in the bulge, whereas the younger are in the arms. The size of the bulge and the degree of arm curl decreases from type Sa to type Sc. In barred spiral galaxies, the core is crossed by a bar of stars, at the ends of which the spiral arms begin. They are commonly younger than elliptical galaxies. Considering their luminosity profile, even if the bulge often has homothetic isophotes, it is very less common for the disk, making them hard to model (see figure 3.6).

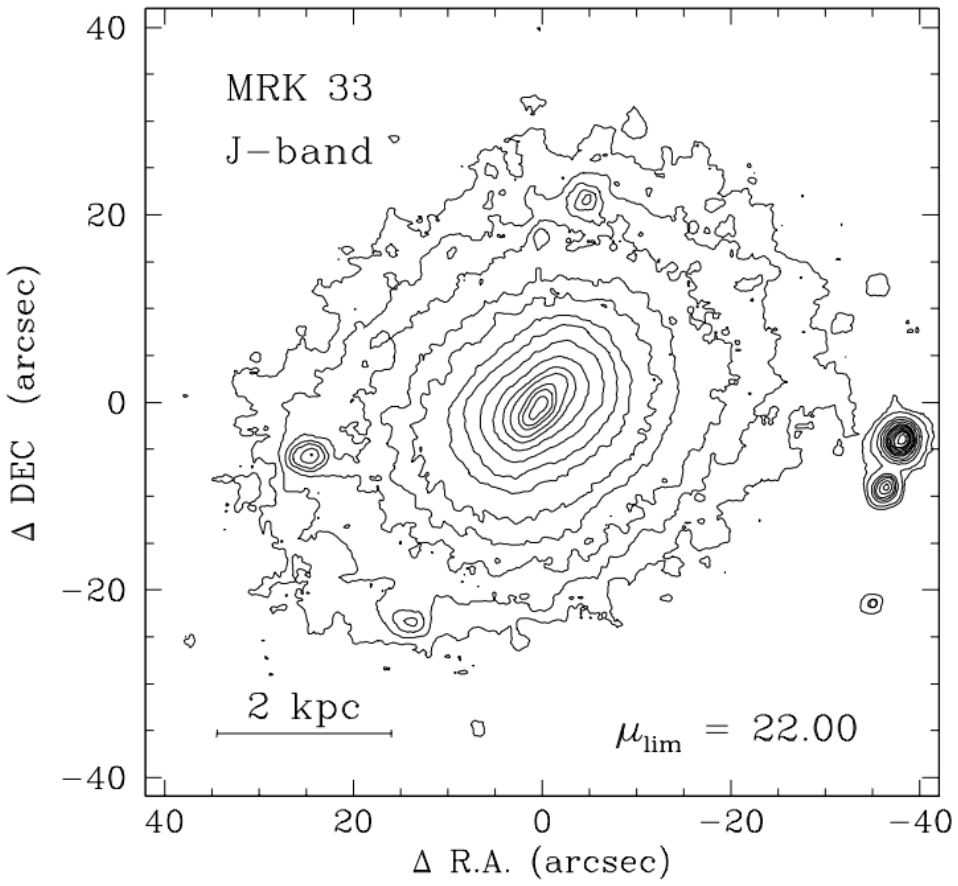

Figure 3.6: *Isophotal map of spiral galaxy MRK 33 (Cairós et al., 2003)*

- **Irregular** : generally refers to galaxies with an ill-defined shape.

- **Lenticular** : galaxies with a very large central bulge and a flattened disk with no spiral arms, and generally with no gas and dust.

As we saw in this section, galaxies have a vast zoology of properties which can make their modeling very complex. They can be used as shear indicators, but it is prudent not to make any assumptions about their shape, both because their light distributions are complex, and because they evolve with redshift. We will see later in section 4.1 how the shear measurement can be quickly limited by using a model-dependant estimator.

3.2 Point Spread Function

3.2.1 Introduction

The Point Spread Function (PSF) is defined as the instrumental response of an imaging system to a point source. In astronomy, when taking images from a ground-based detector, the PSF is a combination of the system response and the atmospheric turbulence, the latter being the most important contribution, especially for large telescopes, even based on sites with good optical conditions.
The effect of PSF is mainly to blur the "above-atmosphere" image of a source, and the resulting image we have on a detector is the convolution of this above-atmosphere image with the PSF. For a star, the expected shape is a point, but the resulting shape in an image is a spot due to the spreading effect of the PSF. The angular size of stars (typically their full width at half maximum) is the most common measure of image quality. A visual representation of the PSF impact on a source image is shown in figure 3.7.

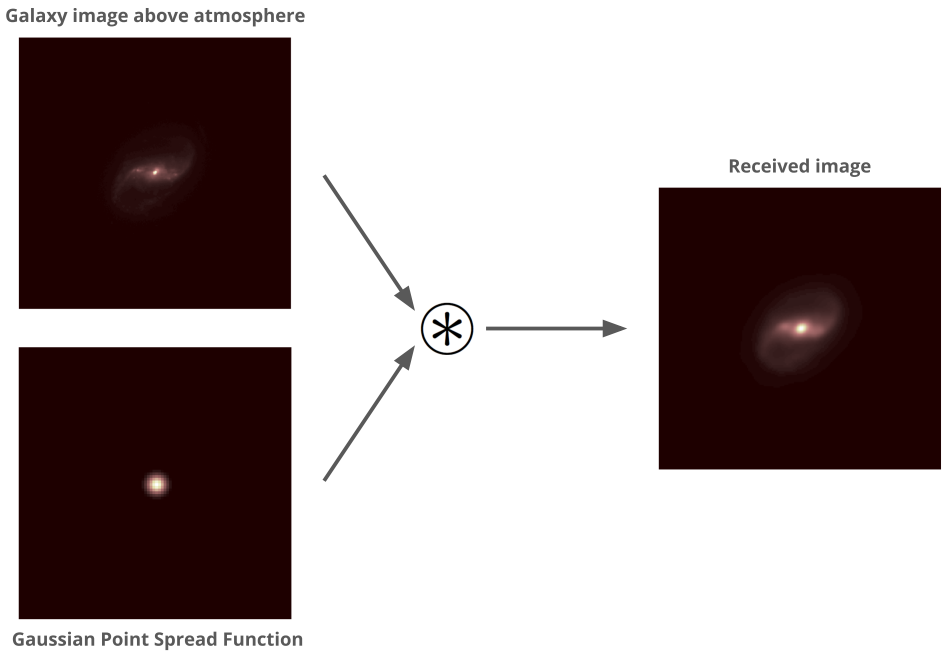

Figure 3.7: *Effect of the PSF on an image taken by an optical imaging system.*

For astrophysical and cosmological studies, it is important to be able to measure the PSF profile affecting the images. Especially for weak lensing, a PSF model is needed for all source galaxies on which the shear distortions are measured. However, because we don't know the intrinsic luminosity profile of galaxies (and also because they are extended on the images), we can't measure the PSF effect directly from their shapes. We therefore use the stars present in the field, because measuring their shapes directly leads to the PSF profile (since stars are point sources in practice). If there is a sufficient number density of stellar images, it is possible to describe the PSF variations across the field by a slowly-varying function (as it can vary across the field

of view). Today, the PSF profiles measured from stars are fairly well reconstructed, with resolution generally below the pixel size, even at the lowest stellar density found at high galactic latitudes.

Another important point to note is that PSF also depends on wavelength ("chromaticity"). As it is modeled from stars measured on broadband images, the model reflects the average Spectral Energy Distribution (SED) of the stars. However, the SEDs of stars and galaxies are different, so considering that the PSF measured from stars is the same over a galaxy introduces a *color bias*. Moreover, the galaxies SED also varies spatially, since their shapes can seriously differ from one filter to another.
For long exposures ground-based PSFs, the wavelength dependence leads to a seeing disc (i.e. PSF size) of : $\alpha_{seeing} \propto \lambda^{-1/5}$ (Roddier, 1981). This implies that the seeing size decreases with higher (redder) wavelengths. On the other hand, for space-based instruments, the optical system is responsible for most of the PSF size, and they are commonly described as "diffraction-limited". As a consequence, the PSF chromaticity is considerably stronger in space than on the ground (and they have opposite trends). The seeing disk follows a D/λ dependence (Airy disk), with D the aperture diameter of the telescope.

3.2.2 Atmospheric turbulence

The broadening of shapes in images due to atmospheric turbulence is called *seeing*. It is an indicator of the quality of sky visibility, and therefore of image quality. The common measure of image quality corresponds to the full width at half maximum of the measured PSF. This effect comes from the variation of the refractive index of the optical medium in the path of light rays between an astrophysical source and the ground detector when two parts of air have different temperatures or humidity. It has multiple effects on images :

- **Oscillation** : When large amplitude turbulence creates shifts of the object diffraction pattern.
- **Speckle** : Occurs in case of high energy turbulence, usually at high altitudes, and looks like multiple bulbs of light separated by dark interstices. Because it is very quickly varying, the effect we observe is the averaged speckle distortion over the entire exposure time.
- **Seeing disc** : Result of multiple speckle patterns superposition when taking a long exposure image.
- **Flashing** : Corresponds to a sudden loss of image definition and details, defocus, and a brightening in the surrounding diffusion pattern (happens only in very poor seeing conditions).

A visual representation of these effects is available in figure 3.8.

The larger the telescope aperture, the more sensitive it will be and affected by atmospheric turbulence, as it is schematized in figure 3.9.

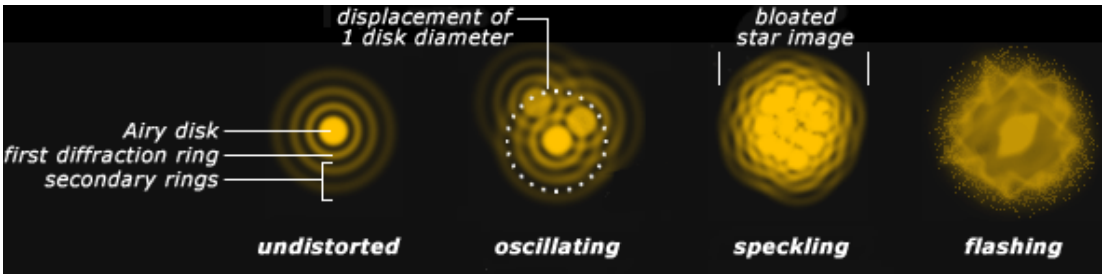

Figure 3.8: *Effect of seeing on a star image (credits : Bruce MacEvoy)*

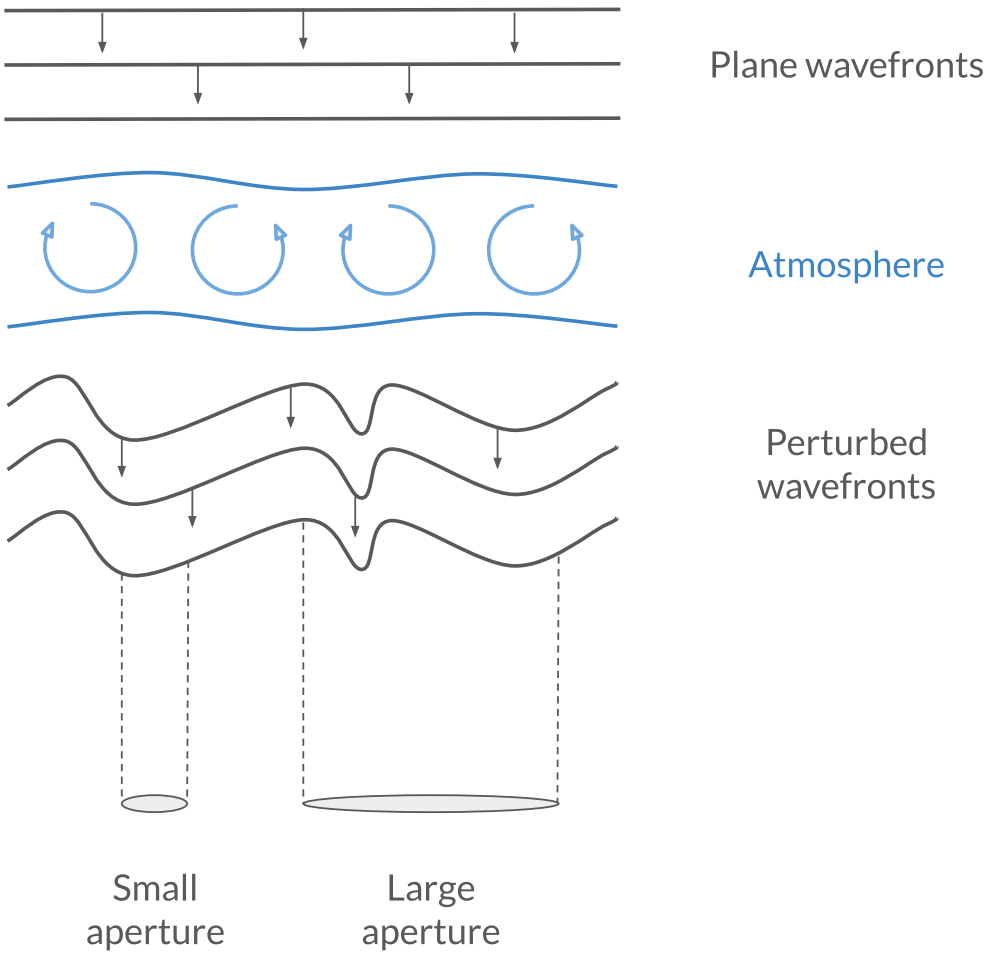

Figure 3.9: *Effect of atmospheric turbulence on source light wavefronts*

In summary, atmospheric turbulence has a number of effects on images, including spreading and smearing of shapes caused by seeing (highest atmospheric layers), and the lower layers causing displacement of objects. The effects depend on the observation site, weather conditions, image acquisition time and telescope aperture.

3.2.3 Instrumental effects and anisotropy

Due to imperfections of optical systems, including guiding errors, the PSF can be anisotropic. This can lead to a PSF ellipticity from 1% to 10%, or more. As it can change with time, depending on the telescope temperature, focus and guiding, it is therefore important to process each exposure separately. Moreover, as we have seen in the previous section 3.2.1, some variations and spatial discontinuities may arise from instrumental effects (like differences in piston between sensors), so it is sometimes necessary to process each CCD independently.
One possible way to correct the PSF anisotropy is to convolve the image with a "circularizing" kernel that contains ellipticity components to compensate for the ones of the PSF and make it round and isotropic. This has the drawback of degrading the image quality and correlating neighboring pixels.

3.3 Shear measurement and bias

3.3.1 Vera Rubin Observatory : *Legacy Survey of Space and Time*

The Vera Rubin Observatory (previously named Large Synoptic Survey Telescope, called LSST after) is an optical telescope based on the El Peñón peak of the Cerro Pachónin mountain in northern Chile. It is named after Vera Rubin, an American astronomer known for her work on the galaxy rotation problem and the discovery of dark matter.
The telescope is a Paul Baker type with three mirrors curved and asphericals to limit optical aberrations (see figure 3.10 left) :

- Primary mirror : 8.4 meter
- Secondary mirror : 3.4 meter
- Tertiary mirror : 5 meter

The camera also holds three lenses, the layout of which is detailed in figure 3.10 right. With its large field of view of 40 time the apparent surface of the Moon (see figure 3.11), the telescope can image the full southern sky (i.e. 18 000 squared degrees) in 3-4 nights (Jee and Tyson, 2011). During a decade, it will take images every night in six different optical filters (*ugrizy*, covering 330 to 1080 nm wavelengths) using a 3200 megapixels camera with a spatial resolution of 0.2 arcsec/pixel.

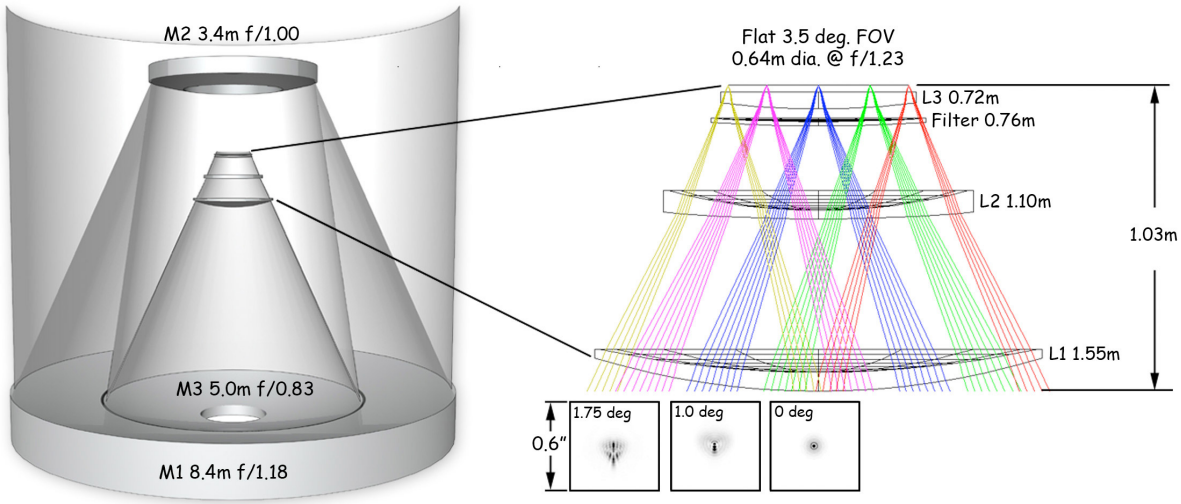

Figure 3.10: *Vera Rubin Observatory optical design*

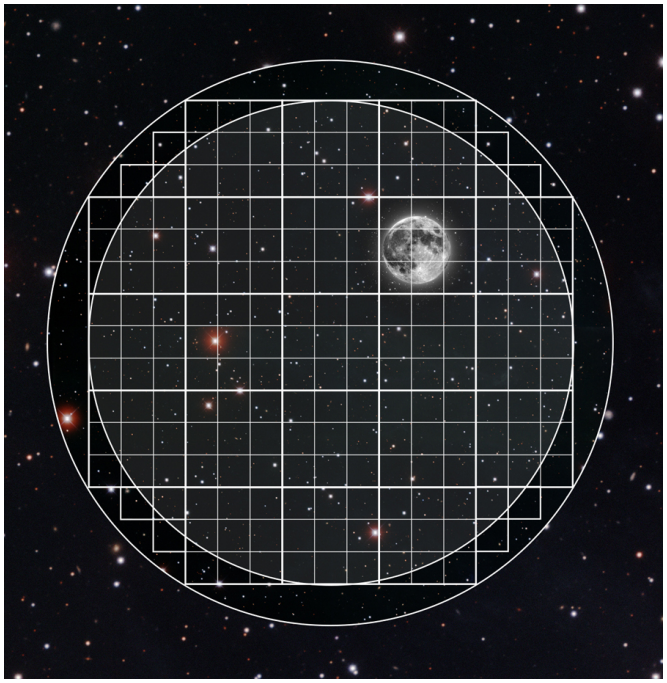

Figure 3.11: *Vera Rubin Observatory field of view*

The scientific goals of LSST cover fields ranging from astrophysics to cosmology and planetary physics, including :

- Mapping the Milky Way, in particular measuring parallaxes beyond the faint *Gaia* limit
- Detecting and tracking asteroids in the Kuiper belt, and other small objects in the solar system

- Detecting transient astronomical events including supernovae, gamma-ray bursts, quasar variability and gravitational lensing

- Studying dark matter and dark energy by observing strong and weak gravitational lensing, baryon acoustic oscillations, and type Ia supernovae

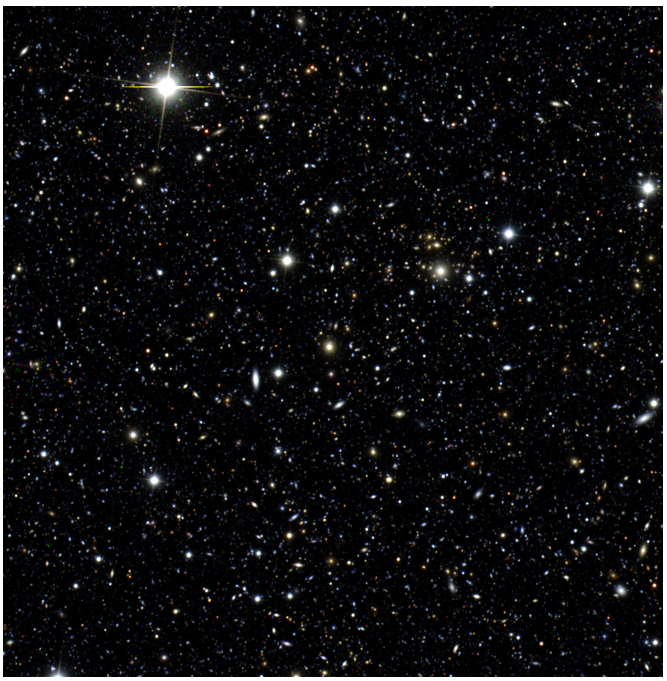

Figure 3.12: *LSST image simulation (source : lsst.org)*

At the end of the 10-year survey, it is expected that LSST will have observed around 20 billion galaxies. Through its optical design and sensitive camera, it is one of the first ground-based surveys designed to observe weak lensing. With such statistics, LSST is one of the surveys bringing observations into the era of precision cosmology. Figure 3.12 represents an image simulation where three frames with different filters were combined. This image corresponds to 13x13 arc minutes of sky, which represents 2.6 parts per million of LSST's ultimate sky coverage (20,000 square degrees).
The expected effective number density of galaxies that can be used for weak lensing analysis (n_{eff}, see section 3.3.2) is around 37 per square arcminute before considering blending and masking, and drops at $\sim$ 26 after (Chang et al. (2013), C13). For comparison, n_{eff} is $\sim$5 in SDSS, and $\sim$5.6 in DES.

As we can see on the year-10 forecast (see figure 3.13), the most sensitive probe to constrain dark energy is the weak lensing, the 3x2pt analysis representing a tomographic analysis of shear-shear, galaxy-shear and galaxy-galaxy correlations.

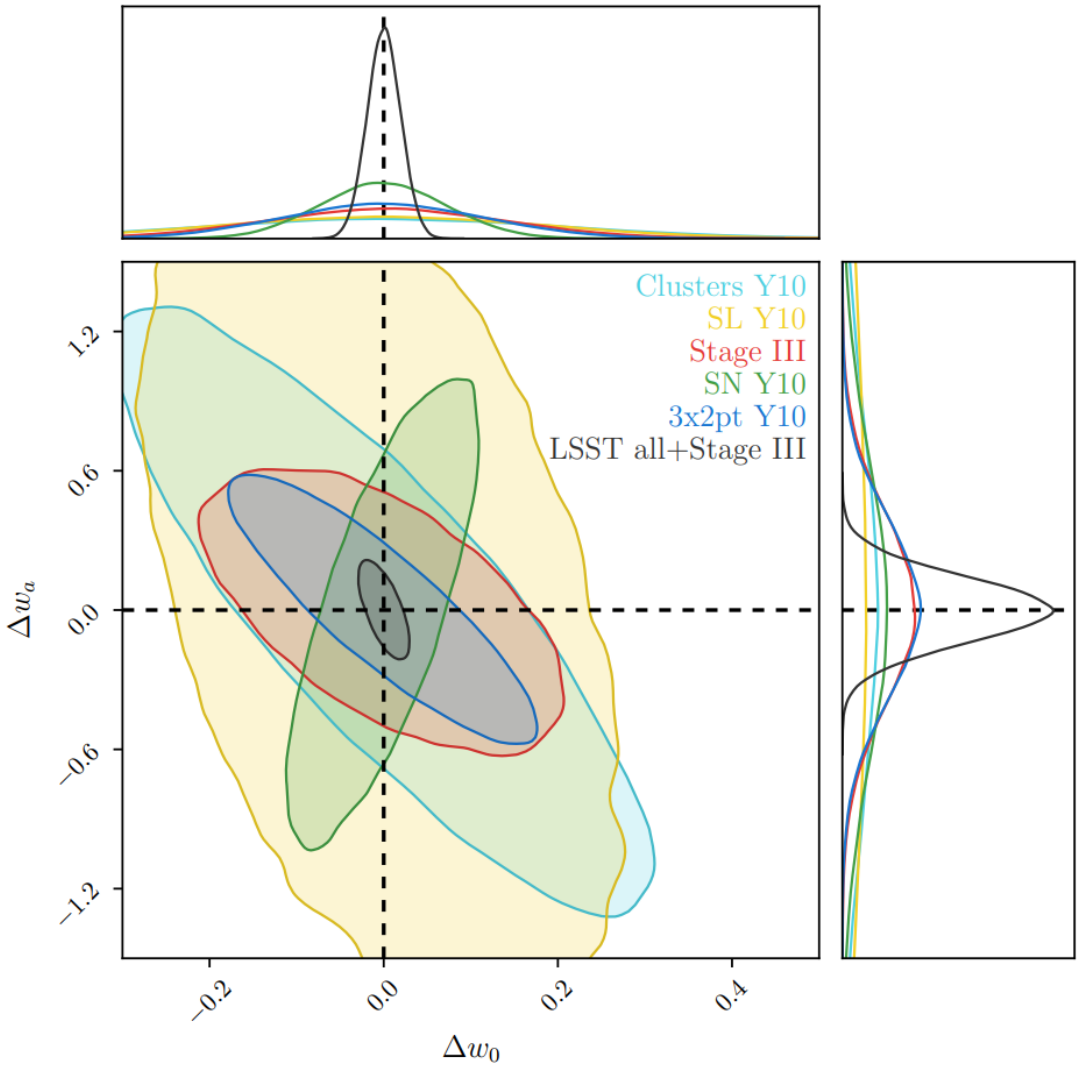

Figure 3.13: *LSST forecast for dark energy constraints at Y10 (source : arxiv:1809.01669)*

3.3.2 Effective number of galaxies and shear noise

In C13, n_{eff} is related to the average shear noise through the equation :

$$\hat{\sigma^2_\gamma} = \frac{\sigma^2_{SN}}{n_{eff}} \tag{3.1}$$

where the shear noise for each galaxy is defined as :

$$\sigma^2_{\gamma,i} = \sigma^2_{SN} + \sigma^2_{m,i} \tag{3.2}$$

with σ_{SN} the shape noise (i.e. the width of the source ellipticity distribution in the absence of shear), and σ_m the measurement noise. We can also rely n_{eff} and the sky coverage Ω :

$$n_{eff} = \frac{1}{\Omega} \sum_i^N \frac{\sigma^2_{SN}}{\sigma^2_{SN} + \sigma^2_{m,i}} \tag{3.3}$$

where N is the total number of galaxies used in the weak lensing analysis. For next-generation surveys, and with an optimal shear measurement method, the shear dispersion is dominated by the shape noise, according to C13 and Heymans et al. (2012) (H12). The shear dispersion $\sigma_{\gamma,i}$ in LSST is expected to be around 0.26 according to C13 (taking $\sigma^2_{\gamma,i} = \sigma^2_{SN}$), and around 0.275 according to H12 (taking $\sigma^2_{\gamma,i} = \sigma^2_{SN} + \sigma^2_{m,i}$). Setting a cut at SNR = 20 in LSST ensures a small contribution of the measurement noise in shear analysis.

3.3.3 Shear bias

The cosmic shear measurement is very complex since we try to estimate a very faint and subtle signal. There are many possible sources of bias that can lead to systematic errors :

- A poorly calibrated shear estimator
- Atmospheric turbulence (see section 3.2.2)
- Instrumental effects (see section 3.2.3)
- Astrometry
- Finite sampling of images
- Noise
- Selection bias

The usual parametrization used to describe the bias between the observed and true ellipticity can be expressed as follows (Huterer et al., 2006) :

$$g^{obs} = (1 + m)g^{true} + c \tag{3.4}$$

with g^{obs} the observed shear of a source, g^{true} its true shape, m the multiplicative bias and c the additive bias. The multiplicative bias generally depends on unaccounted-for galaxy properties and a poor shear calibration, whereas the additive bias results from measurement bias, especially an insufficient PSF anisotropy correction, which induces a preferential orientation in the image plane.
Because the expected shear correlation functions depend on cosmological parameters, a bias on the shear measurement introduces a bias on the cosmological parameters estimation. Considering LSST statistics, an upper bound for these biases is set : according to Cropper et al. (2013), the limits we need to achieve on m and c are respectively 1.5×10^{-3} and 1.3×10^{-4}.

Impact of PSF on shear measurement

Since the PSF affects the observed shapes of sources in images, it is crucial to take it into account when performing shear estimations. The impact of seeing is to make shapes "rounder", especially for the smallest objects, which dilutes the shear signal and makes it even harder to detect, given that the effect of cosmic shear on galaxy shapes only accounts for a few percent of the intrinsic ellipticity. The larger a source is in the image, the less it is affected by PSF.

We also saw earlier that the wavelength dependency of PSF can create a color bias when measuring galaxy shapes. Because the weak lensing signature is achromatic, its spectral and spatial dependency through the galaxies' SEDs can introduce a bias in shear higher-order terms, which is called *color gradient bias*. In practice, this is small for ground-based surveys and can be addressed via image simulations.

By assuming that the galaxies' intrinsic ellipticities are randomly oriented, the cosmic shear should be the only remaining effect in average shape distortion, considering an isotropic PSF. However the measured ellipticity evolves linearly with the PSF anisotropy. The convolution of the image with the PSF in itself introduces a multiplicative bias in the shear estimation, and a poorly corrected anisotropy can lead to an additive bias in the sources' ellipticity, leading to a spurious weak lensing signal. We therefore need a robust method to determine the PSF profile, and a good correction of the anisotropy.

Astrometry

When repeatedly imaging the same area of the sky, using a common source position for all images can reduce shear measurement biases, especially for low SNR sources. This is particularly important for surveys like LSST with short exposure times (15 sec). Averaging positions over multiple images requires precise mappings between image coordinate systems. Accurate position estimations are crucial, because if they are affected by some bias, it can also bias flux or shape measurements, leading to spatially correlated errors impacting cosmic shear studies.

Atmospheric turbulence significantly contributes to astrometric uncertainty, creating anisotropic spatial correlations that vary between exposures. When galaxy shape measurements are performed on co-added images, astrometric residuals affect the measured shapes and the PSF in a correlated way. Even if the atmosphere distortion decrease with the inverse square root of the exposure time, it still leaves a spatial imprint correlated with air displacements, creating a spurious shear signal measured in the direction of the distortion. In Léget et al. (2021), the shear offset $\partial\gamma$ in the astrometric residual direction is defined as :

$$\partial\gamma \simeq \frac{1}{4}\left(\frac{dx}{\sigma_g}\right)^2$$

with dx the position shift and σ_g the rms angular size of the galaxy. For short exposures similar to LSST, they found that the astrometrical residuals can lead to a shear correlation bias as large as the shear signal. In this same article, a correction to observed astrometric residuals was investigated by using Gaussian process interpolation with a correlation function (von Karman kernel). This procedure reduces the residuals' covariances by about one order of magnitude at small angular separations, which becomes acceptable.

Selection bias

Selection bias can be summarized as a set of steps that can introduce systematic errors, from object detection to classification in samples and catalogs.
A bias can be introduced in shear measurement when objects shape matter for entering the source sample, meaning that some shear values are preferred. This effect can be related to image pixelization, because the ellipticity estimation is more sensitive to rotations rather than elongations along the pixels' directions, according to Pujol et al. (2020). Furthermore, the PSF can also impact the detection, depending on its own ellipticity and the objects' orientations. Some configurations favor or disfavor galaxy selection. A method to calibrate this bias was developed by Sheldon et al. (2020), and is called *Metadetection*.
To get a confident and scientifically robust galaxy catalog, we must apply some cuts on the detected samples. These cuts can be applied to several properties, such as the size of the galaxies and the signal-to-noise (SNR) ratio. Some objects can pass under the SNR threshold because of their orientation. Because these properties can be directly affected by the shear, they introduce a bias in its estimation.

Model and noise bias

The model chosen to measure the galaxy shapes can also lead to a shear measurement bias, especially for galaxy-profile-dependent algorithms and the associated assumptions. The noise present in images is also a factor of multiplicative bias, since it makes the galaxy shapes apparently more elliptical due to centroid bias. This bias is also critical for tomographic shear analysis as it increases when the SNR decreases. Because the redshift is related to SNR (the farther a galaxy, the lower its surface brightness, and the lower its SNR), a poor noise bias correction causes a redshift-dependent bias of the shear signal, which can dramatically bias the dark energy equation of state measurement. These two points are the central questions of this thesis. We propose a new approach for shape measurement and calibration independent of the galaxy profile in section 4, and an analytical solution to the noise bias in section 6.

4

Shear estimation method

Contents

4.1 A history of previous shear estimation methods

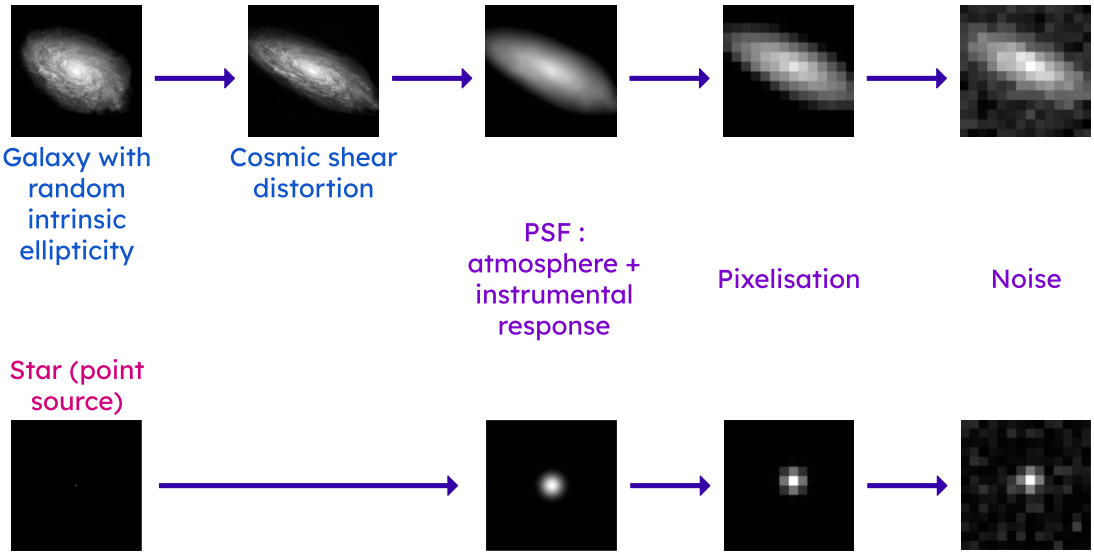

Figure 4.1: *Progressive galaxy or star image degradation between space and detector (credits : pictures are from Bridle et al. (2009)).*

Estimating shear in images has been a challenge for cosmologists since the 90s, the first crucial step being shape measurement. The first step is to find an observable that acts as a shear indicator. We saw in the last chapter that cosmic shear is acting like a coordinate system distortion, and that it requires a statistical detection to be observed. As we are measuring cosmic shear on galaxies, we can use their shapes as an indicator. Moreover, we saw that galaxy ellipticities are supposed to be randomly distributed, meaning that the only remaining effect visible on galaxy shapes distortion after averaging is cosmic shear. For this reason, galaxy ellipticity is commonly used as a shear indicator. Concerning its measurement procedure, two main approaches have been explored over the years : *model fitting* and *moment-based methods* (both detailed right after).

However, as we can see on figure 4.1, the resulting image we get from the detector is subject to many effects that will add spurious signal to the galaxy shape. So in the end, the final shape distortion after averaging is not due to the shear only anymore, but to its combination with atmosphere dilution, PSF anisotropy, pixelisation and pixel noise. If not corrected, these different contributions will increase the multiplicative and additive factors in the shear bias (see section 3.3.3).

Consequently, a calibration step is required to transform a shear indicator into an estimator. We can divide the calibration into two main issues : shape-to-shear calibration, and noise bias correction. A full chapter is dedicated to the noise bias and its

correction. About shape-to-shear calibration, the common issues to all the estimators are PSF dilution and anisotropy. We will detail later how model fitting suffers also from model bias, and how moment-based methods can be affected by a poorly calibrated weight function. Even today, none of the shear estimation methods proposed over the past 30 years has achieved consensus.

In this chapter, we will first review the historical methods of shape measurement and calibration, then detail the shear measurement algorithm developed as part of this thesis and the technical aspects that accompany it.

4.1.1 Model fitting

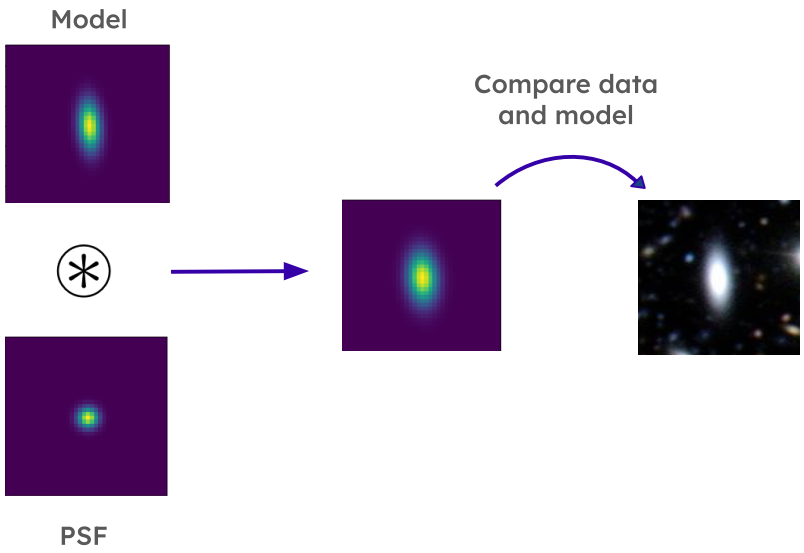

Figure 4.2: *Shape measurement using model fitting*

A widely used approach to determining the light distribution of galaxies is model fitting, which involves defining parametric models of galaxy shape and then fitting the convolution of the galaxy model and the known PSF to observed data using frequentist (maximum likelihood estimation, MLE) or Bayesian methods. Using MLE, a common model is fitted on each image, while each exposure is fitted independently and posterior probability distributions are combined in the Bayesian one. A comparison between frequentist or Bayesian approaches was done by Miller et al. (2007).

However, model fitting is subject to serious limitations, starting with model bias. Indeed, too simplistic or inaccurate models can lead to a bias in the shear estimation (Bernstein, 2010). The main issue is that the number of parameters to fit increases quickly with the complexity of the chosen model. For a basic elliptical profile, there are already six or seven parameters to fit (three for describing the shape through second moments, two for the position, one for the flux and possibly one to describe the radial profile), and there is generally not enough information in the images (especially for

undersampled ones) to perform the fit.
Moreover, the PSF convolved with the image breaks the galaxy profile's symmetries (Lewis, 2009), leading for example to a re-weighting of elliptical isophotes after the convolution. This means that even if we correctly know the PSF profile, we must have a very accurate galaxy model to avoid bias. A detailed review of model fitting limitation was published by Voigt and Bridle (2010).

4.1.2 Moments based methods

Another shape estimation method consists in measuring the light distribution second moments of the image. These (weighted) seconds moments lead directly to the ellipticity. The introduction of a weight function is mandatory due to the presence of divergent noise in un-weighted moments. The first method that laid the groundwork of shear estimations with a moment-based algorithm was proposed by Kaiser, Squires, and Broadhurst (1995) (KSB), where the quadrupole moments are defined as follows :

$$Q_{ij} = \int d^2\theta W(\theta)\theta_i\theta_j f(\theta) \tag{4.1}$$

where $f(\theta)$ denotes the surface brightness of the object, and angles are measured relative to the object's position. The weight function $W(\theta)$ is chosen to be Gaussian, with a scale length proportional to the one of the object. The ellipticity can be then determined :

$$e = \begin{pmatrix} (Q_{11} - Q_{22})/T \\ 2Q_{12}/T \end{pmatrix} \tag{4.2}$$

with $T = Q_{11} + Q_{22}$.
One has to rely on some estimation of the centroid (as for all moments-based methods), and this estimation impacts the estimator's performance. The centroid can suffer from bias caused by the PSF (described in section 4.1.3), and is affected by noise, which biases the ellipticity (6). We will see in the next section how the PSF correction plays a key role in the shape measurement.
Also, the choice of the weight function size is important to minimize the noise in ellipticity measurement. More details on the choice of weight function are given in section 4.2.1 and appendix B.

Another method using adaptive moments was introduced firstly by Bernstein and Jarvis (2002) (BJ02), then by Hirata and Seljak (2003), where the weight function is defined as a Gaussian :

$$W(x) = exp\left(-\frac{1}{2}(x - x_0)^T M_W^{-1}(x - x_0)\right) \tag{4.3}$$

with a second moments M_W which satisfies :

$$M_W^{ij} = 2\frac{\int (x - x_0)_i (x - x_0)_j W(x) I(x) d^2x}{\int W(x) I(x) d^2x} \tag{4.4}$$

Then the ellipticity is defined in the same way as in equation 4.2.

Although adaptive moments better match highly elliptical objects, giving lower uncertainties than the KSB method, this technique is mathematically equivalent to finding an elliptical Gaussian giving the best least-squares unweighted fit of the galaxy image (see appendix A for the demonstration), which makes the method sensitive to some of the biases of model fitting. Thus, objects with an ellipticity higher than $e_i = 0.5$ (limit beyond which adaptive moments override the KSB) are not very common (BJ02).

4.1.3 Shape calibration

We saw in the section 3.3.3 that whatever the chosen shape estimation method, they are generally affected by biases, needing additional calibration. Starting from the ellipticity, which is only a shear indicator, the calibration allows to define a real shear estimator.

Model fitting

For model fitting methods, the calibration is usually determined thanks to simulations. In Miller et al. (2013), these simulations mimic the properties of real galaxies in the CFHTLenS (Canada–France–Hawaii Telescope Lensing Survey) data, including their size distributions, ellipticity, and brightness. They also include realistic noise levels and PSF variations to accurately represent ground-based observational conditions. Then, the biases m and c derived from the simulations are used to calibrate the shear measurements from the real CFHTLenS data.
In Refregier and Amara (2014), the shear calibration is performed using Monte-Carlo Control Loops (MCCL).
A calibration to the *lensfit* algorithm was proposed in Fenech Conti et al. (2017) (for analyzing the KiDS data) by using extensive galaxy simulations carried out with *Galsim* (Rowe et al. (2015)), more details about *Galsim* are given in section 5.1.1) and performing an iterative calibration. Once the biases are sufficiently minimized and the calibration process converges, the final bias correction factors are applied to the observed KiDS shear measurements.

Moments-based methods

Moments-based methods also need calibration. In KSB, the shear is estimated as follows :

$$\gamma = P^{sh} e^{corr} = P^{sh}(e^{obs} - P^{sm} e^{PSF}) \tag{4.5}$$

where γ is the shear, e^{corr} and e^{obs} the corrected and observed galaxy ellipticity respectively, e^{PSF} the PSF ellipticity and P^{sm} and P^{sh} that represents the smear and shear polarizability tensors. These two tensors describe the ellipticity response to the PSF and the shear. The PSF correction procedure was done using artificially sheared and degraded HST telescope data to mimic the effect of seeing.
This method, which has been tried and tested for years, has shown its limits, in-

cluding the assumption that PSF can be modeled and corrected using its second moments. Real PSFs can have complex structures that are not well-represented by simple moment-based models, leading to incomplete or inaccurate corrections. Also, P^{sh} and P^{sm} are measured from data, and so can be noisy and biased.
Shear estimations performed using KSB are biased from 1% to 5% (Bacon, Refregier, and Ellis (2000), Van Waerbeke et al. (2000), Heymans et al. (2006), Massey et al. (2007)), which is at least 10 times higher than the next generation survey's fixed limit for the multiplicative bias.

Another source of bias in many estimators is the selection effect, which occurs when galaxy selection criteria are correlated with the shear signal, or aligned with the PSF. As introduced in section 3.2.3, PSF anisotropy can lead to a spurious shear signal because of the preferred orientation introduced in the image. If the PSF is elongated in a certain direction ($e_1 > 0$), then the galaxies with an opposite ellipticity ($e_1 < 0$) will appear enlarged after convolution. Their surface brightness will then be lowered, and the selection will favor objects with $e_1 > 0$, since many selection cuts are linked to the surface brightness. This effect was originally studied by Kaiser (2000), then by BJ02, and the proposed solution to the selection bias is to consider a target galaxies samples where images were previously deconvolved from the PSF, or by "rounding" the PSF with a convolution kernel.

A noisy centroid measurement may also arise from a PSF stretching, making the position measurement less accurate along the PSF elongation axis, pushing the image ellipticity measurement to be biased in the direction of PSF ellipticity. The fainter a galaxy, the larger the bias. The solution suggested by BJ02 was to calculate an empirical correction, or to add a noise image to recreate the original isotropic noise spectrum after a convolution with a rounding kernel.

A simulation-based calibration method was developed in Hoekstra, Viola, and Herbonnet (2017), where they investigated how slight differences between simulations and data could increase the multiplicative bias. For instance, they found that the bias is strongly correlated to the galaxy size, and that this dependency can be controlled by adjusting the simulation input parameters, or through empirical correction. Moreover, they shown how the bias is related to the galaxy density, as shear measurement algorithms are sensitive to neighbors in galaxy images. This effect is not always taken into account since simulated galaxies are generally alone in their thumbnails. While encouraging, this article highlights the many challenges associated with simulation-based calibration, especially considering data from next-generation survey like Euclid.

Finally, methods using perturbative calibration were proposed by Kaiser (2000) and more recently Sheldon and Huff (2017) (*Metacalibration*), that have many advantages, including not relying on galaxy properties priors. The idea is to introduce artificial shear variations to the image and measure how the estimator responds to these applied variations. In practice, this calibration method can be used both on model fitting or weighted moments-based algorithm.

In *Metacalibration*, the shear variations (represented by the matrix s here) are applied to the galaxy image I deconvolved from the PSF and pixel response P :

$$I(s) = \Gamma \circledast \left[s(P^{-1} \circledast I) \right] \tag{4.6}$$

and reconvolved by a dilated PSF Γ :

$$\Gamma(x) = P((1 + 2|\gamma|)x) \tag{4.7}$$

where γ is the introduced shear distortion.
This procedure introduces correlated anisotropic noise, which can lead to a systematic multiplicative bias.

In the next section, we will describe developments towards a new unbiased shear estimator developed as part of this thesis, where shapes are estimated using second moments, and a calibration method similar to *Metacalibration*, with some improvements to reduce biases and avoid correlated noise.

4.2 Unbiased cosmic shear estimator

4.2.1 Method

4.2.1.a Shape measurement : second moments

Whatever the estimator, the basic principle lies in the fact that the second moments (and more generally all moments after position) of a galaxy image are altered by shear. In the continuous limit, the second moments are expressed as follows :

$$M = \frac{\int (X - X_0)(X - X_0)^T W(X - X_0) I(X - X_0) d^2X}{\int W(X - X_0) I(X - X_0) d^2X} \tag{4.8}$$

with X the image coordinates and X_0 the object position (first moment) that we measure directly into the image, W the weight function and I the image (subtracted from the background). This image results from the convolution between the initial image (before entering the atmosphere) of the galaxy I_0 and the PSF ψ (*Point Spread Function*, see section 3.2). These moments are normalized by the flux of the total image $\int WI$.

The introduction of a weight function serves to optimize the signal-to-noise ratio. Without this, the moments are ill-defined (Kaiser, Squires, and Broadhurst, 1995), as their variance is not bounded and increases with the integration domain. We saw in section 4.1.2 that choosing the appropriate weight function is crucial to optimize moments' noise. According to BJ02, if we consider a round object, the optimal weight function is a Gaussian matching the size of the galaxy. They also develop why the Gaussian profile is a good weight function candidate (even considering more complex galaxy models) especially because of its analytical convenience, its central flatness or its quick dropping. Another important point we learn from this article is that setting

a universal weight function is simpler than trying to fit its profile to every galaxy, especially at low SNR. Following these results, we fix a single weight function that is approximately the same size as the smallest galaxy images we are going to select. This choice is indeed important for optimizing the variance of the estimates, but it is important to remember that the most important source of bias in cosmic shear analyses remains shape noise.

The second moments formula gives a 2x2 symmetric matrix :

$$M = \begin{pmatrix} M_{xx} & M_{xy} \\ M_{xy} & M_{yy} \end{pmatrix} \tag{4.9}$$

We can then define the unormalized ellipticity estimator $\mathbf{e}$:

$$\mathbf{e} = \begin{pmatrix} e_1 \\ e_2 \end{pmatrix} = \begin{pmatrix} M_{xx} - M_{yy} \\ 2M_{xy} \end{pmatrix} \tag{4.10}$$

that describes the shape of the galaxy. Another usual definition of ellipticity is to normalize e_1 and e_2 by the trace of the second moments matrix $M_{xx} + M_{yy}$. In our case we omit this normalization because it would increase the noise of our measurement.

Equation 4.8 can be rewritten as follows (taking X as $X - X_0$) :

$$M = \int XX^T W(X)[I_0 \circledast \psi](X)\, d^2X \tag{4.11}$$

then taking $\psi_-(X) \equiv \psi(-X)$ (thanks to Parseval's identity and the convolution theorem 4.13) :

$$M = \int [(XX^T W(X)) \circledast \psi_-](X) I_0(X)\, d^2X \tag{4.12}$$

using :

$$\int f(x)[g \circledast h](x)\, dx \;= \int [f \circledast g_-](x) h(x)\, dx \tag{4.13}$$

4.2.1.b Second moments calibration

The problem we encounter when designing the estimator is that we are trying to measure the shear on galaxies whose luminosity profiles are unknown, which can generate a bias. Furthermore, even if we assume that galaxies are randomly oriented, the ellipticity we have from second moments is not sufficient to measure the shear because of the PSF contribution. So we need to calibrate this ellipticity, as it was discussed in section 4.1.3.
Moreover, trying to accurately simulate galaxy profiles is a really non-trivial exercise, however the insertion of distortion into images is, on the other hand, a much better controlled practice. We are aiming at defining a shear-sensitive estimator that depends on as few assumptions as possible (especially any assumption about the galaxy profile) and see how it responds to the introduction of small variations in this shear. The

ellipticity calibration will rely on the calculation of a *self-calibration* matrix, defined in terms of second moments derivatives with respect to the shear.

The introduction of a shear will transform the image plane and coordinates (from X to SX to first order) before the transformation by the PSF.
Starting from this, we can use the equation 4.11 to introduce an artificial shear to the deconvolved original galaxy image I_0 :

$$M(S) = \int XX^T W(X)[I_0(SX) \circledast \psi(X)]\, d^2X \tag{4.14}$$

where S is the 2x2 shear matrix, with $\det(S) = 1$. We can then reconvolve the distorted galaxy image with the PSF to recover the initial configuration. This is essentially what is done in *Metacalibration*, but applying a distortion to the galaxy image introduces correlated noise. Instead, another solution can be to use equation 4.12 to apply the shear not to I_0, but to the other terms of the estimator (i.e. : $[XX^T W] \circledast \psi$) :

$$M(S) = \int [(XX^T W(X)) \circledast \psi_-](X) I_0(SX)\, d^2X \tag{4.15}$$

with $\psi_-(X) = \psi(-X)$. The equation can be rewritten as follows :

$$M(S) = \int F(S^{-1}X) I_0(X)\, d^2X \tag{4.16}$$

where

$$F(X) = (XX^T W(X)) \circledast \psi_-(X) \tag{4.17}$$

and in Fourier space :

$$\tilde{F}(k) = -(\partial k \partial k \tilde{W}(k))\tilde{\psi}^*(k) \tag{4.18}$$

We have $\tilde{F(S^{-1}X)} = \tilde{F}(Sk)$, therefore :

$$\begin{aligned} M(S) &= \int F(Sk) I_0(k)\, dk^2 \\ &= \int \frac{F(Sk)}{\tilde{\psi^*}(k)} \tilde{\psi^*}(k) I_0(k)\, dk^2 \\ &= \int G(S,X)[\psi \circledast I_0]\, d^2X \\ &= \int G(S,X) I(X)\, d^2X \end{aligned} \tag{4.19}$$

where

$$G(S,X) \equiv \int \frac{F(Sk)}{\tilde{\psi^*}(k)} e^{ikx}\, d^2x \tag{4.20}$$

This manipulation means that no transformation is applied to the initial image $I(X)$, as the shear variations will be applied directly to $\tilde{F}(k)$, which is a more extensive and better resolved function than I_0. Furthermore, this function is essentially noise-free, so transforming it does not introduce a significant anisotropic noise. Applying the distortion on the original galaxy image would add some correlated noise that can lead to a systematic multiplicative bias, as we deconvolve and reconvolve the distorted

image by the PSF.

Thanks to these derivatives, we can define the self-calibration factor **R**. It is a 2x2 matrix composed of linear combination of the derivatives of the second moments with respect to the shear :

$$\mathbf{R} = \begin{pmatrix} \frac{\partial e_1}{\partial g_1} & \frac{\partial e_2}{\partial g_1} \\ \frac{\partial e_1}{\partial g_2} & \frac{\partial e_2}{\partial g_2} \end{pmatrix} = \begin{pmatrix} \frac{\partial M_{xx}}{\partial g_1} - \frac{\partial M_{yy}}{\partial g_1} & \frac{2\partial M_{xy}}{\partial g_1} \\ \frac{\partial M_{xx}}{\partial g_2} - \frac{\partial M_{yy}}{\partial g_2} & \frac{2\partial M_{xy}}{\partial g_2} \end{pmatrix} \tag{4.21}$$

4.2.1.c Shear estimation

The Taylor expansion of the ellipticity can be written as follows :

$$e = e|_{g=0} + g\frac{\partial e}{\partial g}|_{g=0} + ... \tag{4.22}$$

When averaging over galaxies, the first term vanishes and we can approximate $\langle e \rangle$ as :

$$\begin{aligned} \langle e \rangle &= \langle e|_{g=0} \rangle + \langle g\frac{\partial e}{\partial g}|_{g=0} \rangle + ... \\ &\simeq \langle \mathbf{R}g \rangle \end{aligned} \tag{4.23}$$

Given **R**, we can then define an estimator of the shear $\langle g \rangle$:

$$\langle g \rangle = \langle \mathbf{R} \rangle^{-1} \langle e \rangle \tag{4.24}$$

In the case of a round galaxy, there is no need to average to estimate shear, and the equation 4.24 can be expressed as :

$$g \simeq \mathbf{R}^{-1} e \tag{4.25}$$

The advantage of this method is that calculations are based on second moments, rather than maximum likelihood (or other model-fitting methods), so we don't have to make any assumption about the galaxy profile. Thus, the F function is more extensive than the object image I_0, and so better resolved, it is therefore better to apply shear distortion on it. Accordingly, this method allows to perform shear estimation on undersampled images. Distorting the original galaxy image would introduce some correlated noise due to the deconvolution and reconvolution by the PSF (this is basically what it is done in *Metacalibration*).

4.2.2 Technical aspects and corrections

4.2.2.a Derivatives practical calculation

To find out how M depends (on average) on shear, we can derive the equation 4.19 with respect to γ.

$$\frac{dM}{d\gamma} = \int \frac{dG(S(\gamma), X)}{d\gamma} I(X)\, d^2X \tag{4.26}$$

This expression describes a relationship between shear and second moments, which involve the same pixels in the image.

For real images, the PSF is empirical and we hence resort to numerical derivatives. This procedure follows several steps :

- First, we apply the shear matrix to the coordinates system to distort the pixel grid, following this relation :

$$\begin{pmatrix} sx \\ sy \end{pmatrix} = S \begin{pmatrix} x \\ y \end{pmatrix} \tag{4.27}$$

  where :

$$S = \frac{1}{\sqrt{1-|g|^2}} \begin{pmatrix} 1+g_1 & g_2 \\ g_2 & 1-g_1 \end{pmatrix} \tag{4.28}$$

  with $g = g_1 + ig_2$
  We chose four shear distortion : $(g_1 = \pm\epsilon\ ;\ g_2 = 0)$ and $(g_1 = 0\ ;\ g_2 = \pm\epsilon)$, with ϵ ten times smaller than the input cosmic shear value applied to the galaxy (as we expect the shear values to be in the percent range, we choose $\epsilon = 0.001$).

- Once we have distorted the coordinates system, we can interpolate the F function on the new grid. The interpolation is performed using a bivariate spline approximation over a rectangular mesh.
  Because we have four shear distortions, this procedure leads to four new images.
  A visual representation of these two steps is given in figure 4.3.

- Once we have the four distorted images, we can calculate each of their second moments (noted $M^{1\pm}$ and $M^{2\pm}$) and the derivatives are calculated as follows :

$$\frac{\partial M}{\partial g_1} = \frac{M^{1+} - M^{1-}}{2\epsilon} \tag{4.29}$$

$$\frac{\partial M}{\partial g_2} = \frac{M^{2+} - M^{2-}}{2\epsilon} \tag{4.30}$$

We can also imagine to develop ψ and W on analytical functions to calculate their analytical derivatives before integration on pixels.

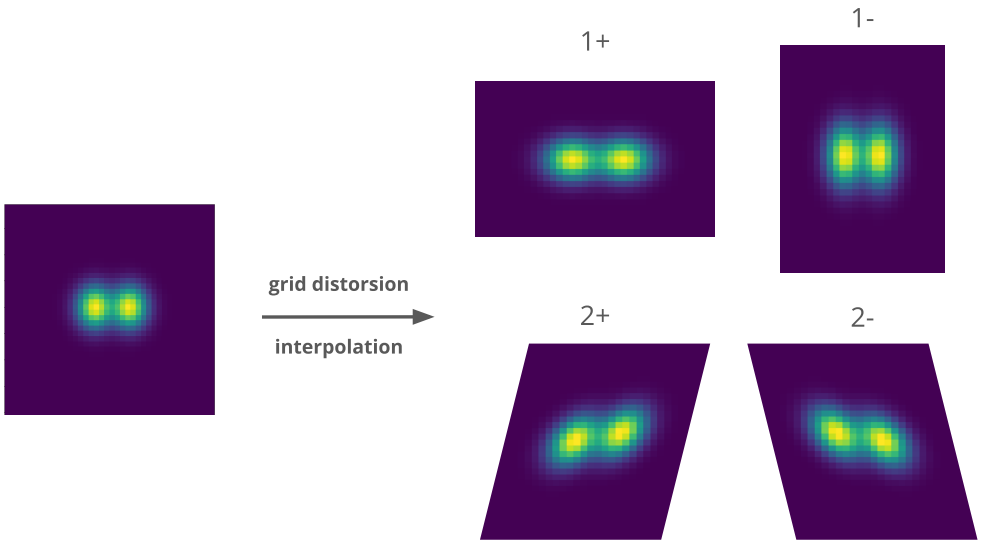

Figure 4.3: *Schematic visualization of the grid distortion and interpolation of the F function. The 1_+, 1_-, 2_+, 2_- values represent the shear applied on the pixels coordinates, respectively ($g_1 = \pm\epsilon$; $g_2 = 0$), ($g_1 = 0$; $g_2 = \pm\epsilon$)*

4.2.2.b Sampling correction

When an image is sampled, this can be translated as a convolution between a continuous function (here the galaxy profile convolved with the PSF) and a tophat function (which corresponds to the pixel response).
This image can be expressed as follows :

$$I(X) = I_c(X) \circledast \Pi(X) \tag{4.31}$$

and therefore, the resulting moments is the sum of the continuous image second moments and the pixels (or tophat function) second moments.

To calculate the pixel contribution, first define the coordinate system using the affine transformation (2D) :

$$\vec{X} = J\vec{i} + \vec{x_0}$$

where J is a 2x2 matrix (called Jacobian), $\vec{i}$ designates the coordinates in pixel space and $\vec{X_c}$ is the pixel center.
The pixel's second moments can be written as follows:

$$M_{pix} = \frac{\int_{pixel} (\vec{X} - \vec{X_c})(\vec{X} - \vec{X_c})^T d^2\vec{X}}{\int_{pixel} d^2\vec{X}}$$

By changing the integration variable :

$$\begin{aligned} (\vec{X} - \vec{X_c}) &= J(\vec{i} - \vec{i_c}) \\ d^2\vec{X} &= |det(J)|\ d^2\vec{i} \end{aligned}$$

where $\vec{i_c}$ is the center of the pixel in native (pixel) coordinates.

We then have :

$$\begin{aligned} M_{pix} &= \frac{\int_{pixel}(\vec{X}-\vec{X_c})(\vec{X}-\vec{X_c})^T d^2\vec{X}}{\int_{pixel} d^2\vec{X}} \\ &= \frac{|det(J)| \int_{pixel} J(\vec{i}-\vec{i_c})(\vec{i}-\vec{i_c})^T J^T \ d^2\vec{i}}{|det(J)| \int_{pixel} d^2\vec{i}} \\ &= J\left[\int_{pixel}(\vec{i}-\vec{i_c})(\vec{i}-\vec{i_c})^T \ d^2\vec{i}\right] J^T \\ &= JJ^T/12 \end{aligned}$$

It is worth noting that :

$$\int_0^1 (x-1/2)^2 \ dx = \int_{-1/2}^{1/2} x^2 \ dx = \frac{1}{12}$$

The total measured second moments is then :

$$\begin{aligned} M &= M_c + M_{pix} \\ &= \int XX^T I(X)\, d^2X \ + \frac{JJ^T}{12} \end{aligned} \tag{4.32}$$

In our simulations, J is a very basic Jacobian, including only the scale s of the image :

$$J = \begin{pmatrix} s & 0 \\ 0 & s \end{pmatrix} \tag{4.33}$$

4.2.2.c Shear and sampling cross-effect bias correction

We introduced in the previous section that sampling add a pixel component to the total image second moments.
As we calculate the derivatives by distorting the pixels grid and interpolating the F function on it, we should subtract a *distorted* pixels second moments to the M^S matrixes (cf 6.21, 6.22). We can rewrite a more general formalism for these second moments :

$$M(s,\epsilon) \propto \gamma + \alpha\epsilon + \alpha'\epsilon^2 + \beta s^2 + \beta' s^4 + \delta s^2\epsilon + \delta' s^4\epsilon \tag{4.34}$$

where s is the image's pixel scale (involved in the Jacobian J) and ϵ the shear variation we introduce to calculate the derivatives. The $\gamma + \alpha\epsilon + \alpha'\epsilon^2$ term represents the continuous sheared second moments, βs^2 is equivalent to M_{pix} in equation 4.32, and the term including δ' is the cross-effect between shear and sampling after the grid distortion, that we will call after SSB. At first, we expected the δ term to be related to this cross effect as well, since we can't consider it as a theoretical one because of its scale dependency. However, it turns out that adding it in the correction introduces a bias, but we can't remove it from the fit at the risk of calculating inaccurate values for the other terms. The question remains open as to its origin.

The $\frac{1}{12}$ factor in equation 4.32 is the value of β for a single image (before any shear application), but here we have a product between I and W, and depending on the sizes of these two components, the β factor will change.
For example, in the case where both I and W are Gaussian, we can re-express the total second moments as :

$$M_{tot}^{-1} = \left(M_W + \frac{JJ^T}{12}\right)^{-1} + \left(M_I + \frac{JJ^T}{12}\right)^{-1} \tag{4.35}$$

using that :

$$G_A = G_B \cdot G_C \Leftrightarrow V_A^{-1} = V_B^{-1} + V_C^{-1} \tag{4.36}$$

where G_X is a Gaussian and V_X its associated variance.

If I and W have the same size :

$$M_{tot} = \frac{M_I}{2} + \frac{JJ^T}{24} \tag{4.37}$$

To calculate β, β', δ and δ', we compute the least-squares solution to equation 4.34. Since the usual values we use for s and ϵ are respectively 0.2 arcsec/pixel (same pixel scale as LSST) and ± 0.001, we chose a range of [0.1, 0.3] for s and [-0.01, 0.01] for ϵ, then we run over 15 values to compute the solution.
We then subtract the β, β' and δ' terms to recover the real image second moments. In fact, since the two β and β' terms are only involved in the M_{xx} and M_{yy} components, they cancel each other out because of the subtractions in **e** and **R** calculations (see 4.10 and 4.21), but they are needed to check a single second moments value. Thus, the only term we need to put into the correction to perform a shear estimation is the last one in equation 4.34.
We see no big impact of the galaxy profile on the parameters estimation, but it is highly related to the size of the galaxy. We computed the relation between δ''s estimation and the second moments of the galaxy for a Gaussian profile, with Gaussians PSF and W.
Here are the results of the fits :

$$\delta'_{xx} = 658.26 M_{xx}^3 - 236.86 M_{xx}^2 + 27.61 M_{xx} - 1.01 \tag{4.38}$$

$$\delta'_{xy} = 131.20 M_{xy}^3 - 51.32 M_{xy}^2 + 6.38 M_{xy} - 0.24 \tag{4.39}$$

Since these fits were performed over round Gaussian galaxies, the fits for δ'_{xx} and δ'_{yy} give the same values. An uncertainty up to 10% is acceptable on these parameters without compromising the shear estimations.

The estimation of δ' is also related to the PSF profile, but since this profile is sufficiently well known (enough to be sampled more finely than the pixel size), it's not as problematic as the relation between δ' and the galaxy which we don't know anything about, except the apparent size on the image that we can measure.

4.3 Conclusion and perspectives

In this chapter, we described the development of a new shear estimation method based on image second moments to measure the galaxy shape.
We saw that the ellipticity alone, although supposed to be null on average, is not sufficient to measure the shear, mainly because of seeing dilution and PSF anisotropies. Also, because we use weighted moments, it is important to choose the weight function size carefully to avoid introducing an additional bias.
To compensate for sources of bias in the shape measurement, we calibrate the ellipticity calculated using second moments using a perturbative method that introduces shear variations into the images. This procedure, which is similar to *Metacalibration*, has several notable innovations and advantages :

- All calculations are based on second moments rather than other model fitting techniques, allowing no assumptions to be made about the galaxy profile.
- The original (deconvolved) galaxy image is not distorted, contrary to *Metacalibration*, which generates correlated anisotropic noise leading to a multiplicative bias.
- The shear variations are applied on a more extensive and better-resolved function ($[XX^TW] \circledast \psi$), which allows shear estimations on under-sampled images.

There are, however, avenues for improvement to be explored. First, we saw in the previous section that the cross-effect between shear and sampling which introduces a bias in the distorted second moments is also dependent on the PSF profile. In this work, we calculated a correction of this bias for a Gaussian PSF profile, which works pretty well even for other PSF profiles (tests on noise-free simulations are the subject of the next chapter). We also tried to perform a fit using a Moffat profile for the PSF, but the resulting coefficients did not properly correct for second moments. This could mean that an adjusted correction with a more complex PSF profile requires the addition of its fourth moments (and maybe the fourth moments of the galaxy). We can imagine calculating tabulated correction values as a function of the PSF size and profile.

Another possible improvement would be to calculate the second moments derivatives analytically. Since we are not applying any distortion to the image, the PSF can be developed on analytical functions. Good candidates are the quantum harmonic oscillator eigenfunctions (Bernstein and Jarvis (2002), BJ02), which have many remarkable properties, including that they are invariant under Fourier Transform (allowing analytical convolutions) and that transformations (rotation, shear etc...) can be expressed easily as combination of operators. Performing these calculations in Fourier space would overcome sampling, making it likely that the SSB would disappear.

Finally, a shear estimator cannot be considered complete without a correction algorithm for PSF anisotropies (introduced in 3.2.3). Because these anisotropies will contribute to the average second moments, it is necessary to compensate them.
One possible way to perform this compensation is to define a weight function in such a way that the F function (see equation 4.17) is round. Following BJ02, we can use the shapelets basis functions to characterize objects' shapes and define the expected

response.
These functions have angular symmetries defined by the value of the quantum number m, which can be defined through the eigenfunction formula :

$$f_{n,m}(r,\theta) \propto P_{n,m}(r)e^{im\theta} \tag{4.40}$$

where $P_{n,m}(r)$ is a polynomial depending on m, n the order of the state (corresponding to its energy) with $-n \leq m \leq n$ (the allowed values are separated by two). States with $m = 0$ are azimuthally symmetric, and those with $m = \pm 2$ change sign under a rotation of $\pi/2$. By describing the pre-seeing galaxy using a basis function $f_{n,m}$, we can define the second moments in the following manner :

$$M = \int XX^T W(X)[\psi \circledast f_{n,m}](X)d^2X \tag{4.41}$$

This formalism allows W to compensate for PSF skewness by ensuring that $m = 0$ delivers $M \propto \begin{pmatrix} 1 & 0 \\ 0 & 1 \end{pmatrix}$, $m = 2$ delivers $M \propto \begin{pmatrix} 1 & 0 \\ 0 & -1 \end{pmatrix}$ and $m = -2$ delivers $M \propto \begin{pmatrix} 0 & 1 \\ 1 & 0 \end{pmatrix}$.

5

Estimations on noise-free simulations

Contents

5.1 Simulations

In this section, we will describe how we simulated our galaxy images to perform our shear estimations. We will test the estimations at different steps, from very basic simulations on Gaussian and Sersic profiles, to real profiles using the *COSMOS* catalog. All the simulated galaxy, PSF and weight function profiles are performed using the *GalSim* package, which is described right after in section 5.1.1.

5.1.1 The *GalSim* package

GalSim (Rowe et al., 2015) is an open-source software for simulating images of astronomical objects with a large variety of profiles, combinations and transformations. Its development was initiated by *GREAT3* (Mandelbaum et al., 2015), a weak lensing measurement challenge requiring a large number of galaxy simulations. Beyond the needs of this challenge, it is possible to simulate very realistic galaxies using *GalSim* for many other types of projects.

The key features of *GalSim* are :

- Modularity : It allows users to build simulations by combining various components such as galaxy models, point spread functions, noise, and more. It also contains many operations and transformations as convolution, deconvolution, rotation, shear, shifts etc...
- Flexibility : Users can customize simulations to fit their specific research needs. For example, a large amount of parameters are available to modify any type of profile at will (flux, full-width-half-max, centroid offset etc...).
- Accuracy : The toolkit is designed to handle complex galaxy shapes and PSFs accurately, which is crucial for precise astronomical studies.

GalSim also includes second moments and shear measurement routines, along with several PSF correction functions. The adaptive moments algorithm described in Hirata and Seljak (2003) is the method used to measure the observed image moments. The calculations are performed by matching an elliptical Gaussian weight function to the object image. The adaptive moments routine's output gives estimations of ellipticity, second moments sigma, centroid, and other image parameters, and the shear estimation routine returns the shear parameters corrected from the PSF and the PSF shape, among others.

This package is particularly useful for simulating data for large-scale surveys like LSST and calibrating weak lensing measurements, which requires highly accurate galaxy shape measurements. The software is open-source and written in C++ with a Python interface.

5.1.2 Galaxy and PSF models

To test the robustness of the estimator, and ensure that measurements are independent of galaxy shape, we have chosen to perform the estimations on different galaxy profiles and PSF provided by *GalSim*.

We chose these profiles for the galaxy :

- **Gaussian** :

$$I(r) \propto e^{-\frac{r^2}{2\sigma^2}} \tag{5.1}$$

  The Gaussian profile is interesting as a first approach because the expected Gaussian-weighted second moments can be calculated analytically.

- **Sersic** :

$$I(r) \propto e^{(-\frac{r}{R_H})^{\frac{1}{n}}} \tag{5.2}$$

  where n is the Sersic index R_H the half light radius. Sersic's law is a generalization of de Vaucouleur's law, which is only effective for representing elliptical galaxies. Sersic's law also includes an efficient representation of spiral galaxies. Its index n corresponds to the slope of its luminosity curve (i.e. n=4 corresponds to the de Vaucouleur law, and n=1 to an exponential law).

We have also chosen three different profiles for PSF modelling :

- **Gaussian** :

$$I(r) \propto e^{-\frac{r^2}{2\sigma^2}} \tag{5.3}$$

- **Kolmogorov** :

$$T(k) \propto e^{-\frac{D(k)}{2}} \tag{5.4}$$

  defined in Fourier space, where $D(k) = 6.8839\left(\frac{\lambda k}{2\pi r_0}\right)^{5/3}$, λ is the light wavelength (in the middle of the bandpass) and r_0 the Fried parameter. In our simulations, we fix the FWHM of the light distribution, which is defined in *GalSim* as $\sim 0.976\lambda/r_0$. A Kolmogorov profile is frequently used to represent a long exposure atmospheric PSF.

- **Moffat** :

$$I(r) \propto (1 + (\frac{r}{r_0})^2)^{\beta} \tag{5.5}$$

  where r_0 is the scale radius, and taking the kurtosis $\beta = 3.5$. The FWHM of the profile is calculated as follows : FWHM $= 2r_0\sqrt{2^{1/\beta} - 1}$. This profile is widely used to model PSFs, as it provides a better representation of the wings' distribution than a Gaussian or a Lorentzian.

Moffat and Kolmogorov profiles are frequently used to represent the effect of seeing in the case of ground-based detectors. The surface brightness of different galaxy and PSF profiles are given in figure 5.1 and 5.2 respectively.

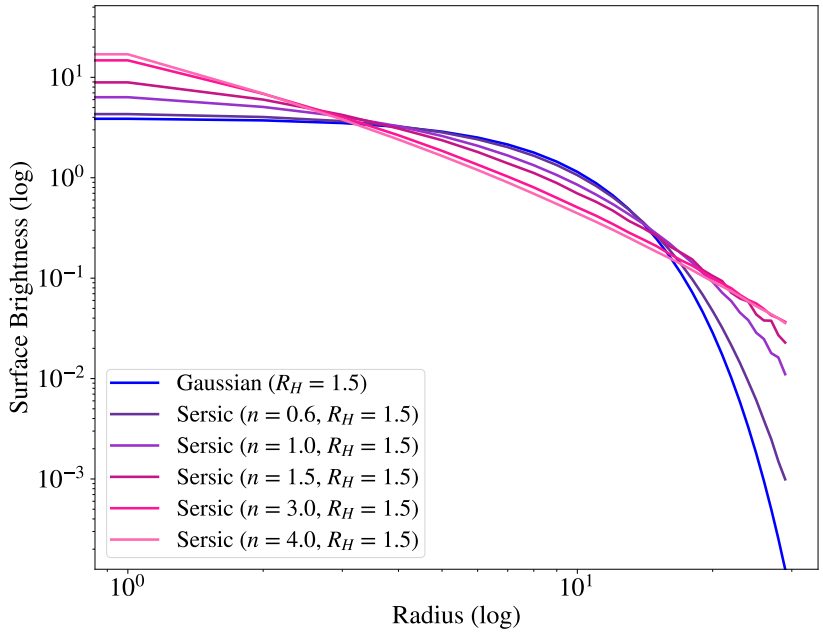

Figure 5.1: *Radial light distribution of different galaxy profiles simulated with GalSim*

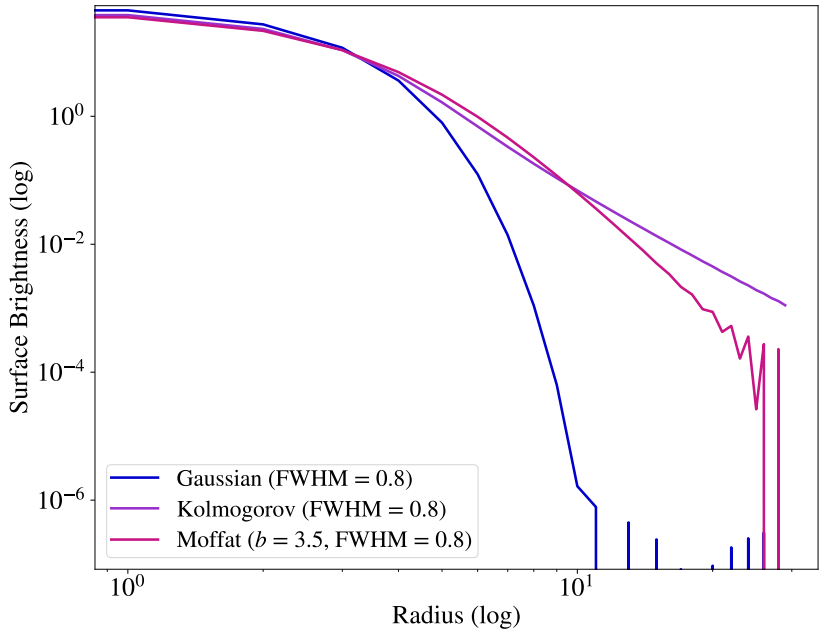

Figure 5.2: *Radial light distribution of different PSF profiles simulated with GalSim (logscale). The strills visible in the wings of the profiles are probably numerical artifacts of the Fourier transform in GalSim.*

Once we decide which profile we want to use, the second important thing is to consider different size ratio between the galaxy and the PSF to determine the limits of the estimator. Taking the weighted second moments of the image and the PSF as a sum over the pixels :

$$\begin{aligned} M_{image} &= \sum_{i,j}^{N} X_i X_j^T W_i [I_0 \circledast \psi]_i \\ M_{PSF} &= \sum_{i,j}^{N} X_i X_j^T W_i \psi_i \end{aligned} \tag{5.6}$$

we can define the *trace ratio* (TR) as follows :

$$TR = \frac{Tr(M_{image})}{Tr(M_{PSF})} \tag{5.7}$$

This ratio will be the reference for choosing our parameters, especially the fixed W size. A similar criterion was also defined in Mandelbaum et al. (2018) (M18) and Zuntz et al. (2018) (Z18) for the Subaru HSC Y1 and DES Y1 shear catalogs respectively. In M18, their criterion is defined as : $R = 1 - \frac{M_{PSF}}{M_{image}}$, and their analyses are limited at R around 0.3 (TR=1.43), meaning that below this value, the shear estimation will become poor because of the PSF dilution. In Z18, the trace ratio involves the weighted second moments of the galaxy above atmosphere, and not the one of the convolved image, with a threshold around 0.5 (TR=1.5).

To test the limits of our estimator, and following the threshold established in M18 and Z18, we choose our profiles' parameters in order to correspond at certain TR key values (between 1.25 and 1.8). We decided to set the FWHM of the PSF to a given value (usually 0.8 arcsec), and then we varied the FWHM of the galaxy to achieve the desired TR values.
The choice of weight size has been set regarding the un-weighted trace ratio between the image and the PSF. To do this, we choose the limiting case beyond which estimations are expected to deteriorate, i.e. TR $= 1.5$. Considering Gaussian galaxies and PSF, this ratio corresponds to $\sigma_{image} \sim 1.22\sigma_{PSF}$. We therefore choose the weight's σ to be 1.25 times higher than the PSF σ (if the PSF's FWHM $= 0.8$ arcsec, the weight's FWHM $= 1$ arcsec), as we saw before in section that the optimal weight size is equivalent to the image size. In the same way as for PSF, this value will be fixed for all the simulations.

5.1.3 Other parameters

We set the pixel scale of the simulated images to 0.2 arcsec/pixel, which is similar to the LSST pixel scale.

To mimic real cosmic shear estimation over a sample of galaxies, we apply different intrinsic ellipticities to the chosen galaxy image before averaging. We usually take random values between -0.3 and 0.3, and we duplicate these values with an

opposite signs to generate our sample. By following this method, we make sure to have a null intrinsic ellipticity on average, which cancels the shape noise of simulated samples.

For the simulated cosmic shear, we choose values ten times smaller than the ellipticity, usually between -0.03 and 0.03, and we set ϵ at 0.001 (ten times smaller than the average shear value) to distort the grid and perform the calculation of the derivatives. A visual representation of the shear distortion applied to a galaxy is shown in figure 5.3.

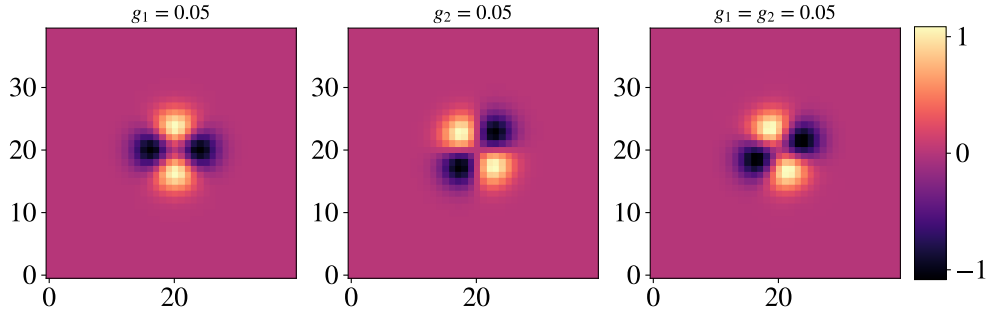

Figure 5.3: *Difference between a round galaxy and a sheared galaxy with $g_1 = 0.05$ (left), $g_2 = 0.05$ (middle) and $g_1 = g_2 = 0.05$ (right).*

5.2 Shear estimations

On noise-free image simulations, the first tests were carried out on images with Gaussians galaxies, PSF and weight function. Then, a set of tests using more complicated profiles was performed, using Sersic profiles for the galaxies and Kolmogorov or Moffat profiles for the PSF. We finally performed a shear estimation on a realistic galaxy profile from the *COSMOS* catalog.

5.2.1 Gaussian and Sersic galaxies

The first sanity check we must do is to perform a shear estimation on very basic profiles, i.e. Gaussian galaxies. The estimations are performed over 40 random shear values and we average over 20 pairs of random (and opposite) intrinsic ellipticities. We have varied the galaxy size between $\sigma = 0.24$ and $\sigma = 0.4$, which corresponds to TR=1.27 and TR=1.73 respectively.

In all the figures that follow, we show the absolute (top) and relative (bottom) differences between the input and the estimated shear (as a function of the input shear), with the associated trace ratio in the figure caption. Figure 5.4 shows the difference between an estimation performed without any correction for the SSB, and

an estimation done under the same simulating conditions with the correction developed in section 4.2.2.c. We see that both g_1 and g_2 are biased on the left figure compared to the right one, especially g_1 which is much more sensitive to the sampling than g_2. In fact, g_1 has an influence on M_{xx} and M_{yy}, which are also affected by the scale via the Jacobian (equation 4.33), contrary to M_{xy} which is linked to g_2. This highlights the particular importance of SSB correction, without which the shear could be biased by 3 or 4 times more than the limit imposed on the multiplicative bias.

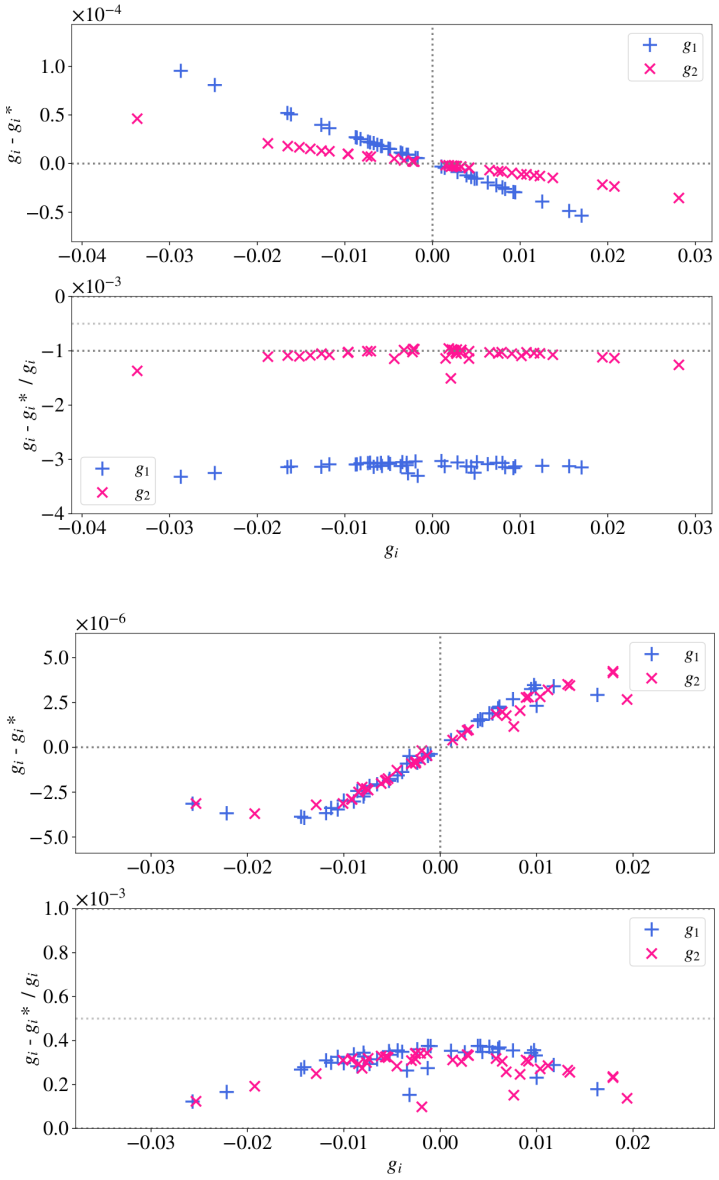

Figure 5.4: *Shear estimations performed on Gaussian profiles (galaxy and PSF), with TR=1.32. For both figures, the upper panel represents the absolute difference between input and output shear, and the lower one the relative difference.*
Top : Estimation performed without any correction for the SSB.
Bottom : Same conditions including the SSB correction.

Figure 5.5 shows the shear estimation for a Gaussian PSF, figure 5.6 a Kolmogorov PSF and figure 5.7 a Moffat PSF.

Whatever the trace ratio, both Gaussian galaxies and PSF give very accurate shear estimations, we always satisfy our multiplicative bias limit under 1×10^{-3}. This is not a surprising result since Gaussian profiles are particularly basic, and also because the SSB introduced in section 4.2.2.c was corrected using a Gaussian PSF model, so we benefit from exact calibration. This same correction is used for every PSF profile.
For other PSF models, we have very satisfying results at fairly low trace ratio values, even if we can't go as low as for the full Gaussian estimation. This can be easily explained because the SSB correction does not accurately describe the simulated data when a non-Gaussian PSF profile is used. This conclusion is reached quite naturally since at low TR, g_1 becomes more biased than g_2, which is the parameter most sensitive to sampling. Nevertheless, all these estimations on Gaussian galaxies are biased under the per mil level, and to very acceptable TR values.

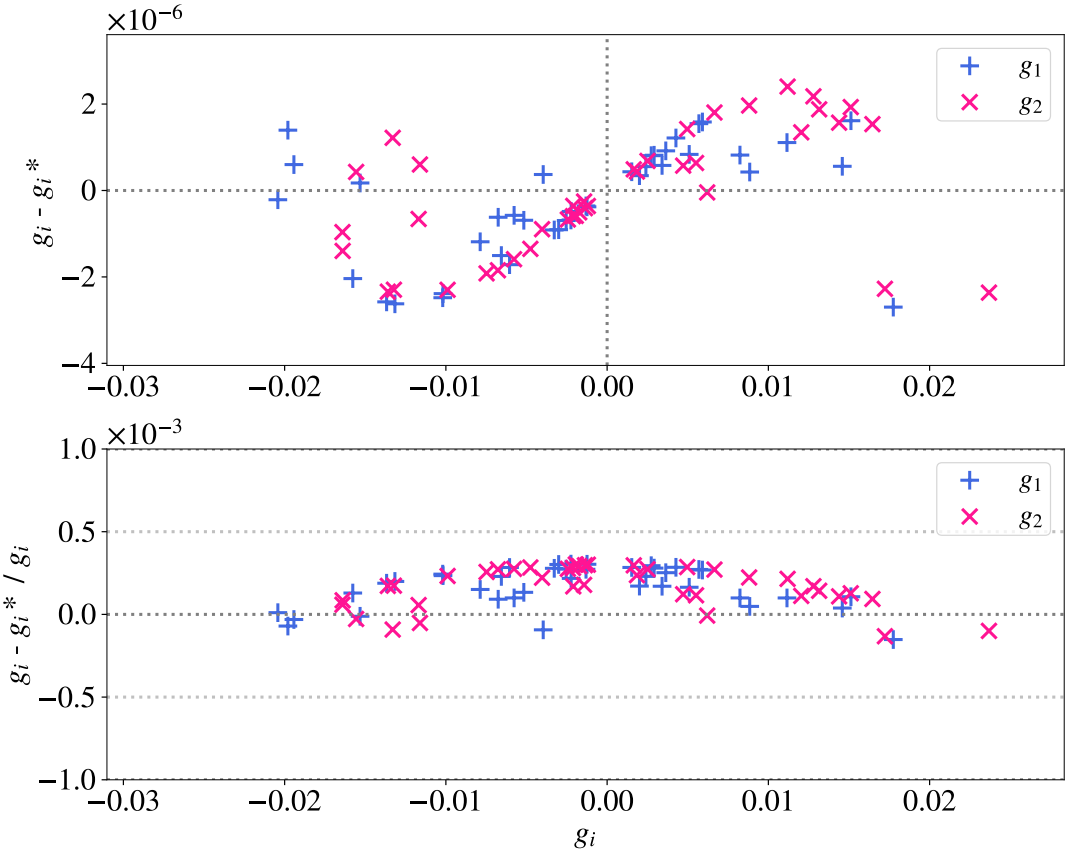

Figure 5.5: *Shear estimation on elliptical Gaussian galaxies convolved with a Gaussian PSF. Trace ratio = 1.50.*

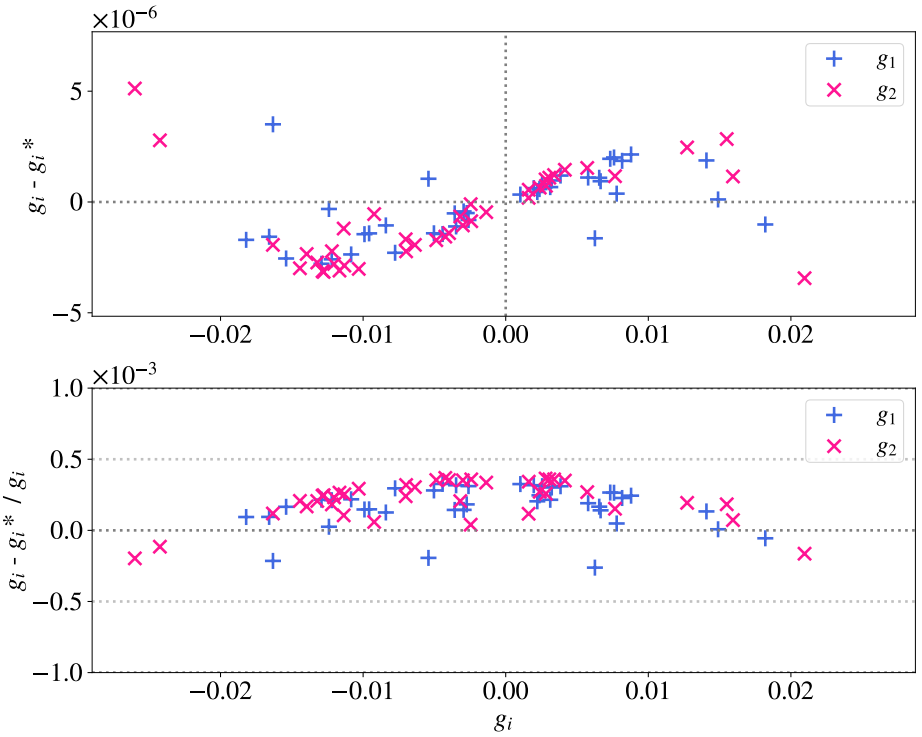

Figure 5.6: *Shear estimation on elliptical Gaussian galaxies convolved with a Kolmogorov PSF. Trace ratio = 1.57.*

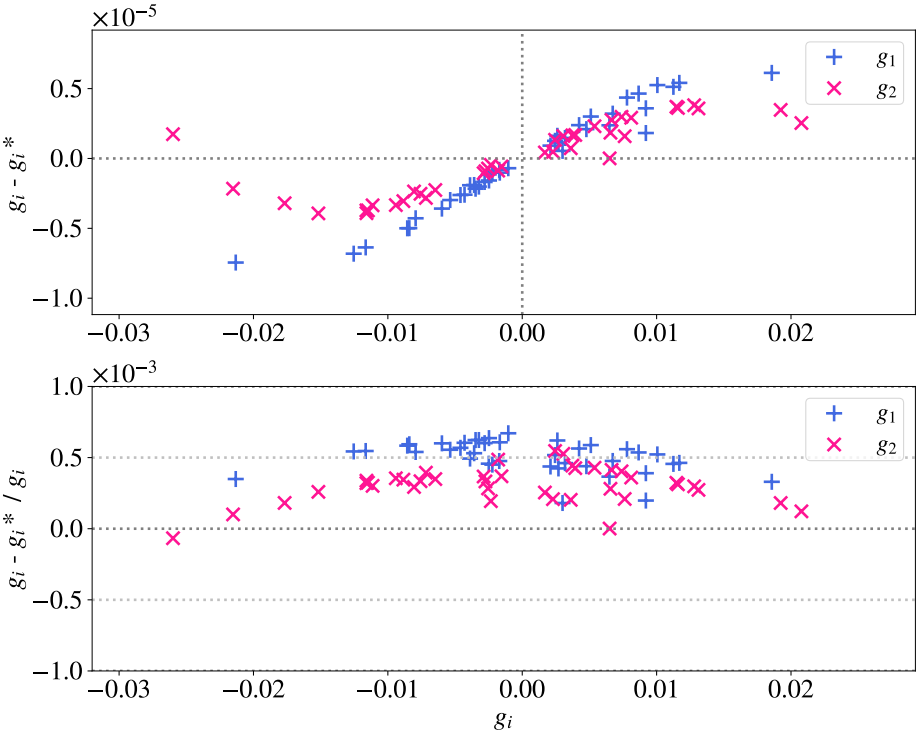

Figure 5.7: *Shear estimation on elliptical Gaussian galaxies convolved with a Moffat PSF. Trace ratio = 1.47.*

To perform estimations on more complicated and realistic profiles, we choose to simulate Sersic galaxies. We chose three values for the Sersic index n : 1.0 (exponential profile), 1.5 and 4.0 (elliptical profile). The exponential profile is usually used to represent disk galaxies, like spirals. Once again we oriented the galaxy profile using 20 pairs of random intrinsic ellipticities, and we performed the estimations on 40 shear values.
The conclusion is similar to the one with Gaussian galaxies : we achieve a bias under 10^{-3} in all the estimations, for every PSF model and at realistic TR values.

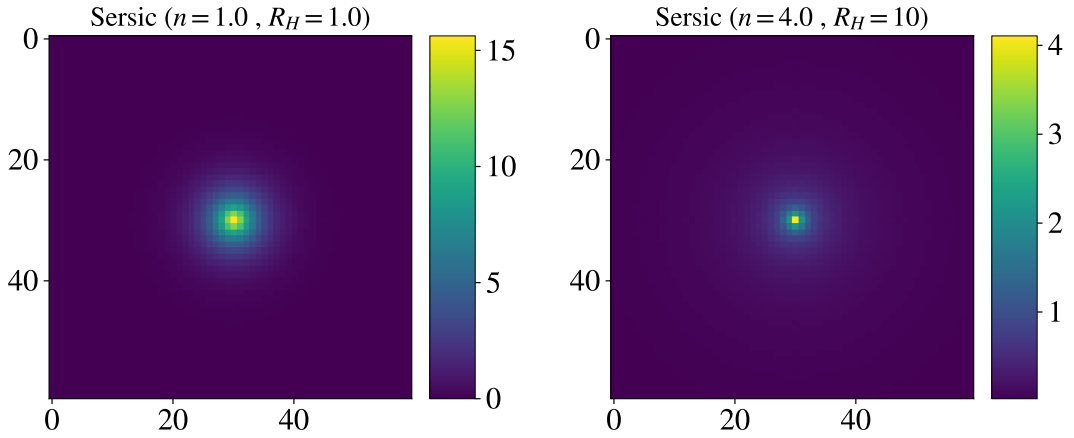

Figure 5.8: *Two Sersic profiles simulated with GalSim*

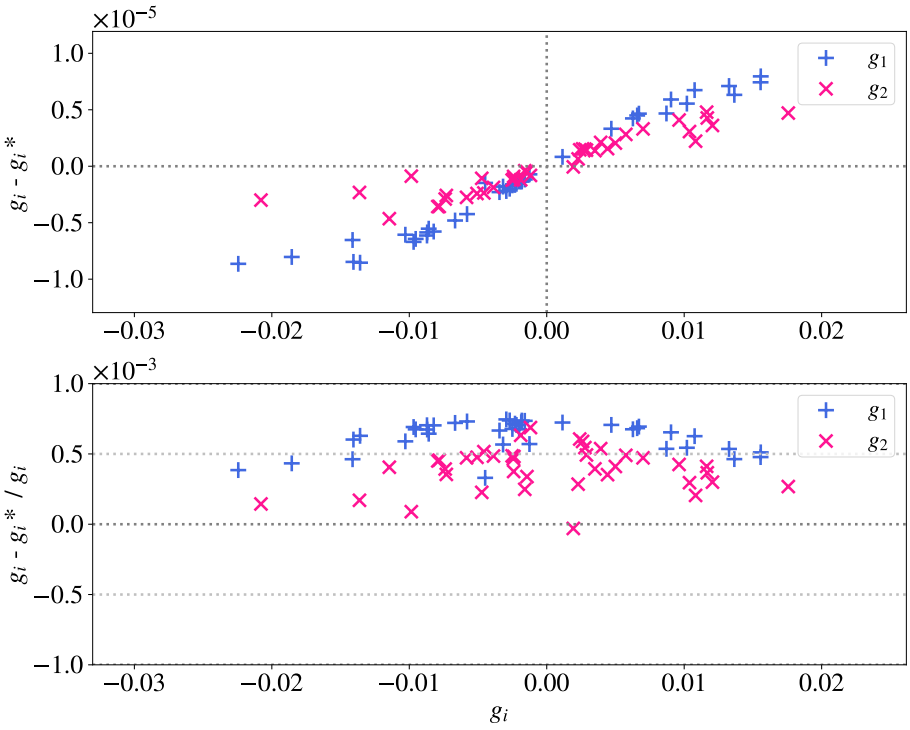

Figure 5.9: *Shear estimation on elliptical Sersic galaxies (n=1.0, R_H=0.55) convolved with a Moffat PSF. Trace ratio = 1.57.*

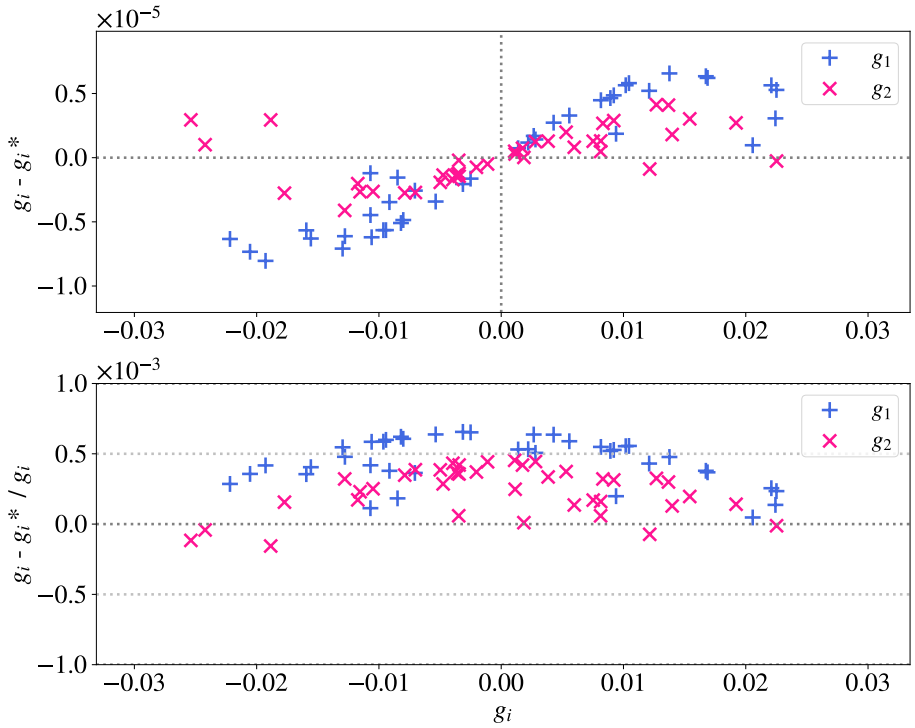

Figure 5.10: *Shear estimation on elliptical Sersic galaxies (n=1.5, R_H=0.9) convolved with a Moffat PSF. Trace ratio = 1.66.*

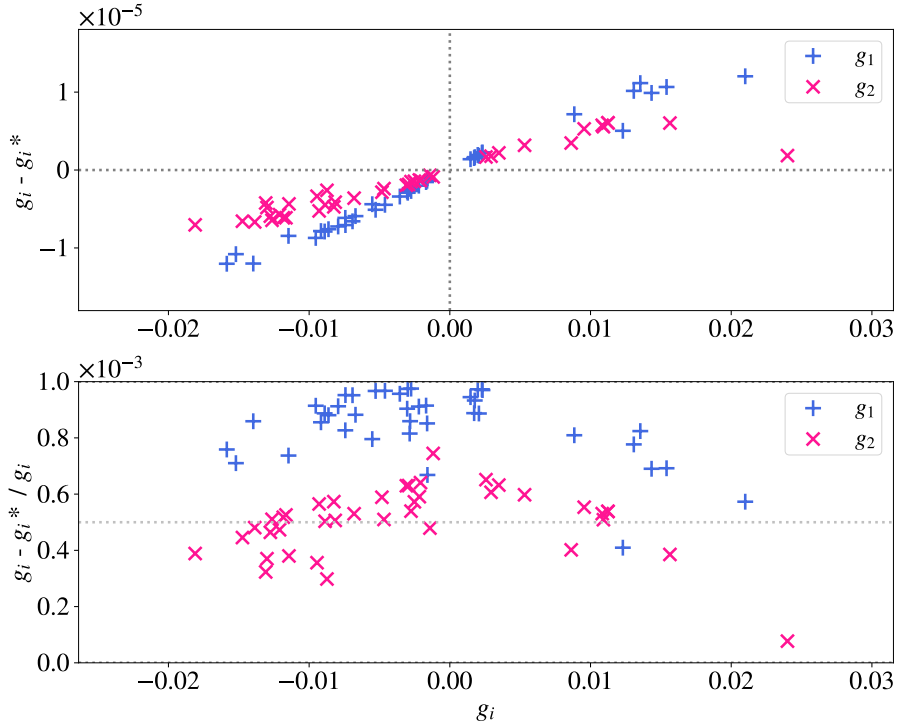

Figure 5.11: *Shear estimation on elliptical Sersic galaxies (n=4.0, R_H=3.53) convolved with a Moffat PSF. Trace ratio = 1.63.*

5.2.2 Bulge and disk galaxies

Many galaxies in the universe actually have a composite profile, made of a bulge and a disk. This configuration is found mostly in spiral galaxies. The bulge is usually modeled using a Sersic profile (with $0.5 < n < 6$), and the disk can be represented with an Exponential profile. The two most frequently observed bulge profiles are elliptical ($n = 4$) and spiral-like ($n = 1$). We thus chose to look at composite profiles where bulges' Sersic index takes these specific values. The bulges and disks half-light radius are given in arcsec. The chosen PSF profile is a Moffat for all the estimations.

We see that for a roughly equal TR of 1.57 (figure 5.12) and 1.52 (figure 5.13), the limit of 10^{-3} for the multiplicative bias is achieved, however, it seems that we can more easily go to lower TR values for spiral-like bulges. This may come from the fact that when $n = 1$, the bulge and the disk have the same profile (Exponential), which is not the case anymore when $n \neq 1$. This hypothesis would need further investigation. Also, the light is more concentrated in the center than in the wings of the distribution when n increases, which can make shape (and shear) information harder to measure. This would explain why the estimation is better for a bulge with $n = 1$ than $n = 4$ at a similar TR value.

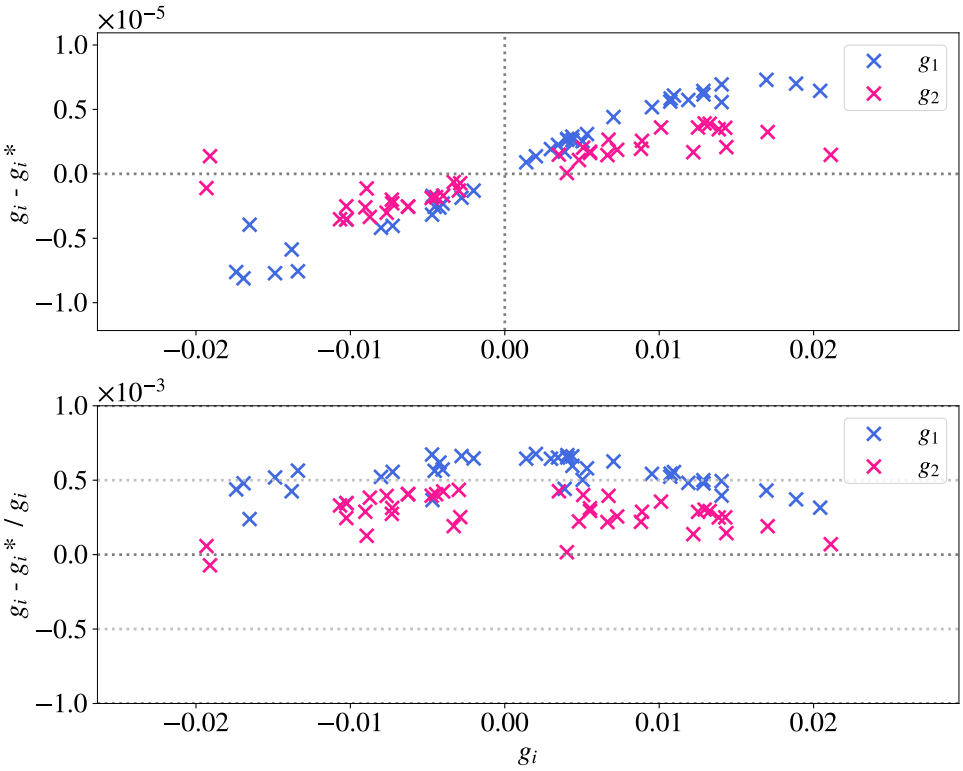

Figure 5.12: *Shear estimation on a bulge ($n = 1$, $R_H = 0.5$) + disk ($R_H = 0.8$) composite galaxy convolved with a Moffat PSF. Trace ratio = 1.57.*

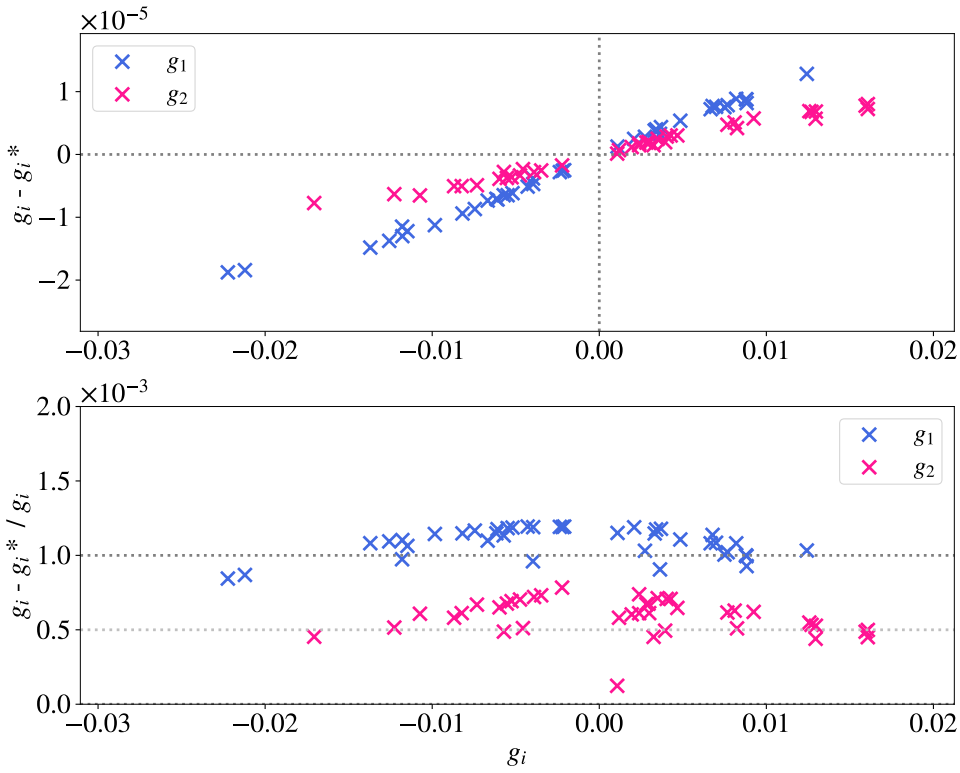

Figure 5.13: *Shear estimation on a bulge ($n = 4$, $R_H = 0.8$) + disk ($R_H = 0.8$) composite galaxy convolved with a Moffat PSF. Trace ratio = 1.52.*

5.2.3 Realistic galaxy profiles : *COSMOS* catalog

COSMOS (Scoville et al., 2007) is a multi-wavelength survey that uses data from a wide range of telescopes, including the Hubble Space Telescope, to map a two-square-degree area of the sky. The survey covers wavelengths from X-ray to radio and provides a detailed look at the distribution and properties of galaxies over cosmic time. Because of its wide range of redshift (from $z \sim 0.5$ to $z \sim 6$), this catalog provides galaxies with both common and atypical shapes.
The main goals of this survey were to better constrain the evolution of galaxies, stars, LSS and AGNs, but also to constrain dark matter through galaxies' weak lensing measurement. These images have a number of advantages, in particular the diversity of profiles and the absence of atmospheric PSF. This sample of galaxy images is often used to test shear measurement for ground based survey because a known shear can introduced in the images prior to convolution by the atmospheric PSF.

A sample of *COSMOS* is implemented in *GalSim*, with $\sim$ 56 000 galaxies. To ensure noise-free shear estimations, we chose images with a flux $>$ 5000. The following results were performed on the object n°31085, shown in figure 5.14.

To cancel shape noise in the estimations using *COSMOS* galaxies, we need to rotate the galaxy profile in different orientations. Analogously to the random pairs of ellipticities defined before, we create 50 random pairs of angles in radians (each angle is

associated with its opposite value by adding $\pi/2$). We pass the galaxy images into the interpolation routine of *GalSim* before applying the rotation transformation, then we resample the final image after the convolution with the PSF. This procedure can be carried out without introducing any spurious information into the image at the time of interpolation, as COSMOS images have a very high sampling rate (0.03 arcsec/pixel), and the scale used to sample our simulations is 0.2 arcsec/pixel.

Concerning shear estimations, it is difficult to achieve the per mil limit for TR under 1.6, especially for non-Gaussian PSF (see figures 5.16, 5.17, 5.18). One possible explanation for this result is that even if the *COSMOS* images taken by Hubble are not affected by the atmospherical turbulence (since the telescope is in space), the images suffer the effects of an instrumental PSF. We can see it in the radial galaxies' light distribution, where the wings always decrease more slowly than clean *GalSim* simulations (see figure 5.15).
The absence of visible values in the center of the graphs is because we remove shears too close to zero which can sometimes lead to outliers caused by the division in the relative difference. The reason is twofold : first, we don't expect to measure shears very close to zero (because it would take a huge statistic to measure such small values), and also because the shear bias is to be considered on average over the sample, and not for every measured galaxy. Thus, we are interested in the average of all absolute shear differences divided by the mean of the true values, and not by the mean of each individual ratio, that is why outliers can be removed.

More figures showing shear estimations with all these previous galaxy profiles (Gaussian, Sersic, composite and *COSMOS*) are available in appendix C, exploring others profiles parameters and TR values.

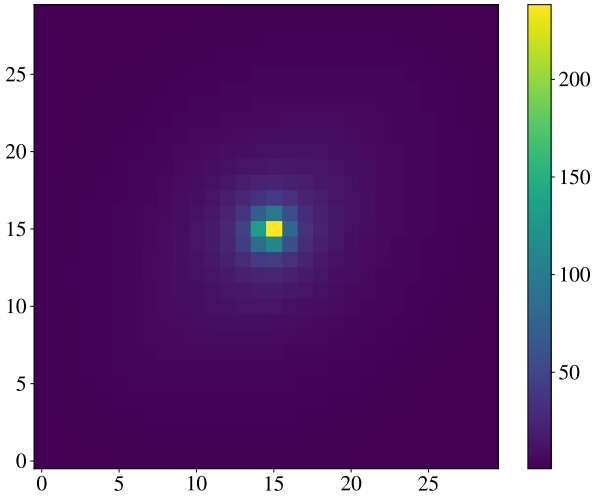

Figure 5.14: *COSMOS galaxy n°31085*

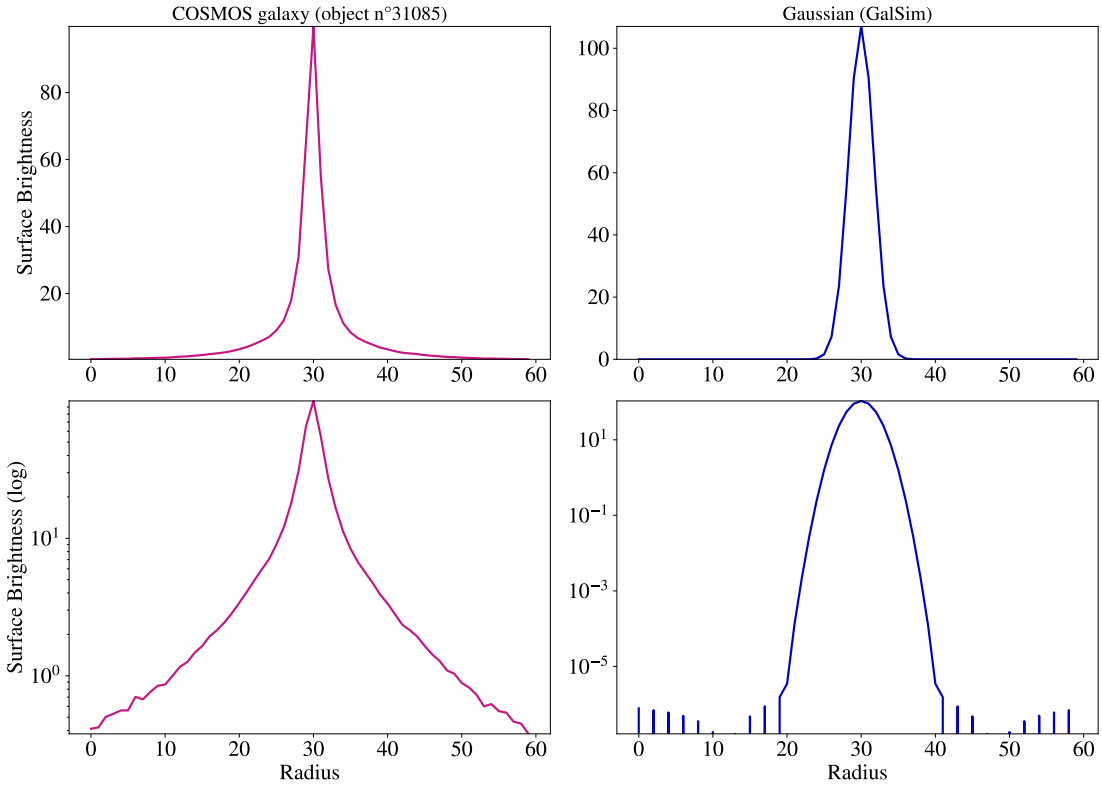

Figure 5.15: *Comparison of luminosity profile decay between a COSMOS galaxy and a profile simulated with GalSim.*

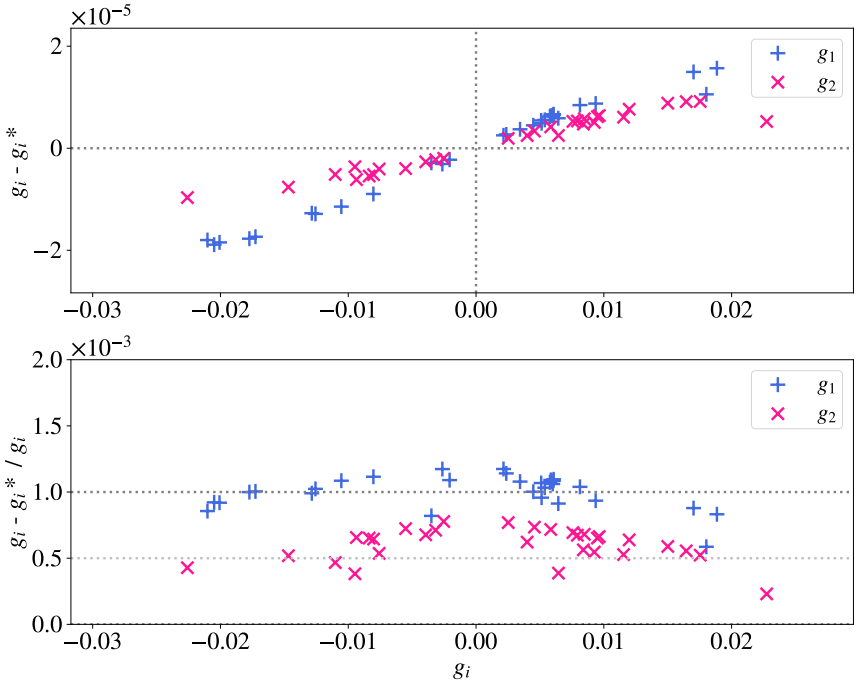

Figure 5.16: *Shear estimation on COSMOS galaxy (object n°31085) convolved with a Gaussian PSF. Trace ratio = 1.56.*

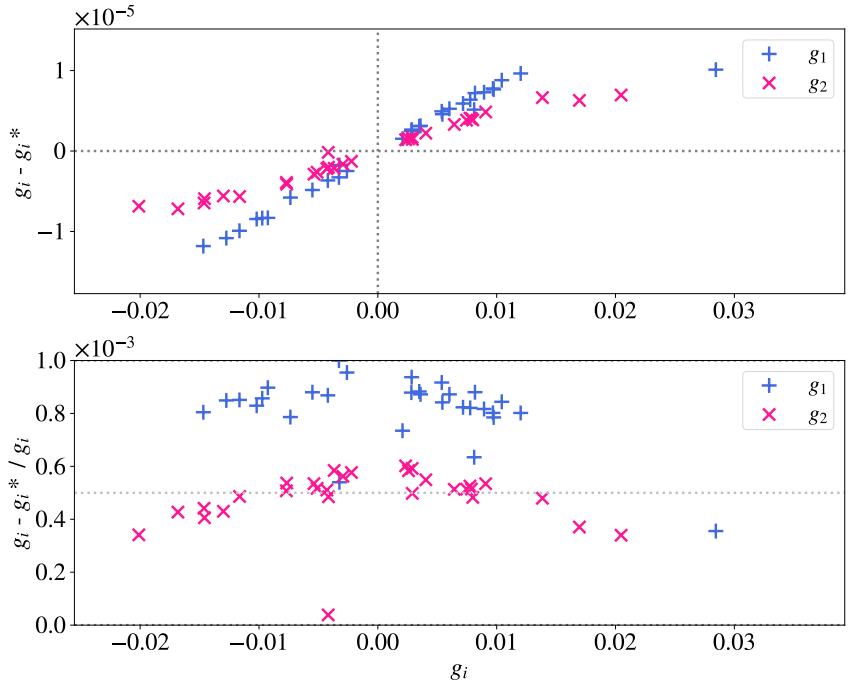

Figure 5.17: *Shear estimation on COSMOS galaxy (object n°31085) convolved with a Kolmogorov PSF. Trace ratio = 1.62.*

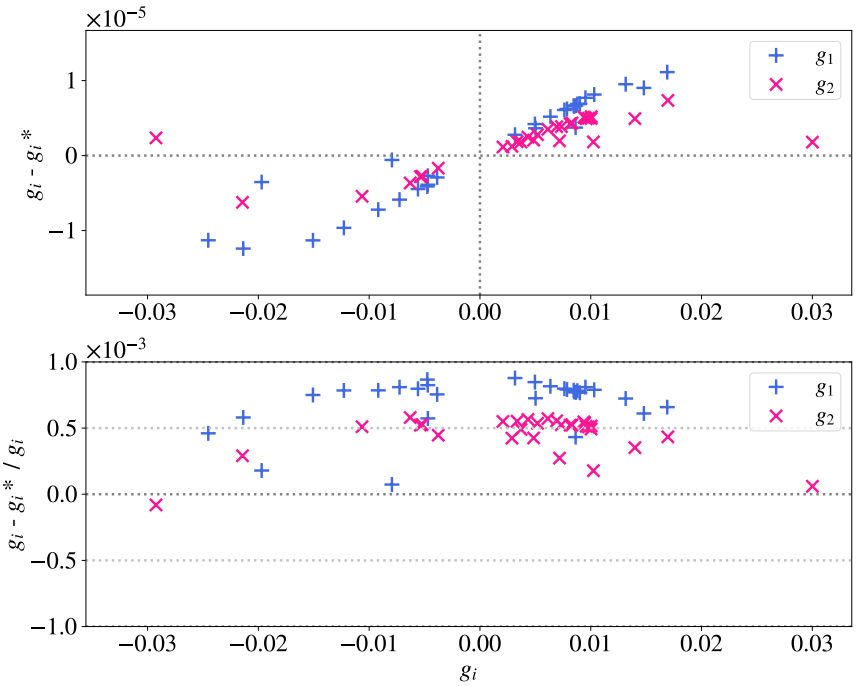

Figure 5.18: *Shear estimation on COSMOS galaxy (object n°31085) convolved with a Moffat PSF. Trace ratio = 1.62.*

5.3 Conclusion

In this chapter, we have explored several sets of simulations, from the most basic models to Hubble Space Telescope images, in order to test shear measurements using the estimator presented in section 4.2.1. The challenge is to be able to measure an averaged shear whose relative bias is of the order of 1×10^{-3} or less, for realistic galaxy to PSF sizes ratios. These tests produced highly satisfactory results, regardless of the galaxy and PSF profile combination.

We note that in almost all these estimations (without considering the slight residual bias on g_1 for low-TR estimates performed using a Kolmogorov or Moffat PSF profile), the bias affecting the shear measurement is around 0.5×10^{-3}. The fact that this bias takes similar values regardless of the chosen profiles is probably linked to the shear formalism that is used, and could be corrected by adding higher-order terms to the second moments' derivatives. However, since these estimations fall within the set limits for the multiplicative bias, we haven't explored this hypothesis.

Finally, all these tests were performed on noise-free images, which does not correspond to realistic observational conditions. The next step is therefore to achieve the same results using noisy simulations. Nevertheless, adding noise to images introduces bias in shape and shear measurements, so the estimation method will need an additional calibration.
The noise bias and its calibration are the main topics of the next chapter.

6

Realistic shear estimations : noisy simulations

Contents

6.1 Noise bias

In this chapter, we will describe the concept of *noise bias*, its origins, its impact on shear measurement and how it was corrected in the previous estimation methods. We will then introduce a new noise bias correction method developed within this thesis's framework, which consists of analytically calculating the second-order terms of the moments affected by the noise.

6.1.1 Introduction

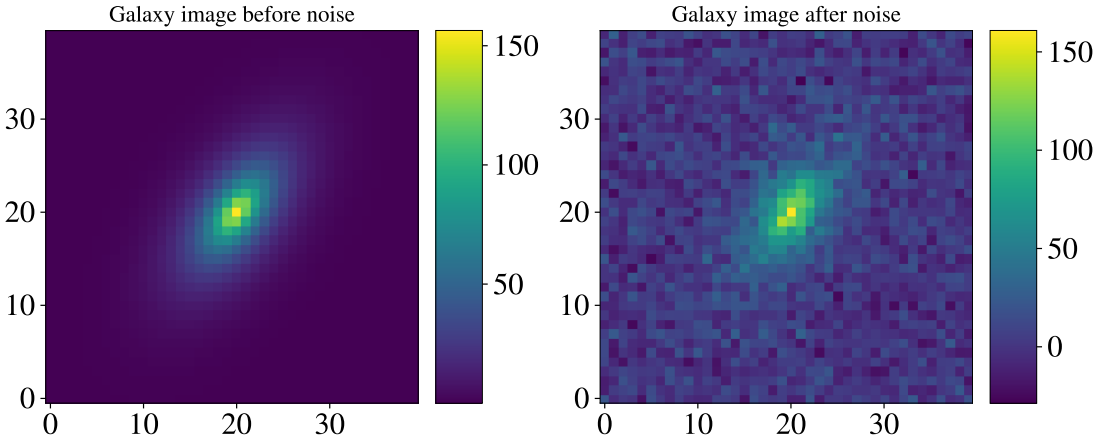

Figure 6.1: *Galaxy image without noise (left) and after the addition of a noisy image (right). The noisy image was simulated using a random Gaussian noise (SNR = 60).*

As it was briefly introduced in chapter 4.1, data we receive from detectors are usually affected by noise (see figure 6.1). This noise has two main contributions :

- **Shot noise** : Caused by the variability of photon detection on a sensor. Its main contribution is the sky background, including zodiacal or galactic light. This noise follows a Poisson distribution. Usually, when a distant object image is taken, like a galaxy, its flux is negligible compared to the background noise, meaning that the sky background is assumed to be stationary and uncorrelated. For brighter objects where this approximation is arguable, the noise bias affecting shear measurements is sufficiently small to keep treating the noise as stationary. It is however conceivable to modify the calculations that follow in order to account for the shot noise of the object light on uncorrelated pixels.

- **Image noise** : Inherent source of noise caused by electronics in the telescope, including the sensor's temperature (thermal or Johnson-Nyquist noise) and stability. It represents the fluctuation affecting the image between acquisition and recording. This noise is usually characterized by measuring the repeatability of "empty" images, called biases. It is commonly named readout noise.

The shot noise is the dominant counterpart visible on science images. The image noise is expected to be a few electrons per pixel (for instance, 4.5 electrons r.m.s

are associated to readout noise in the HSC CCDs around -100°C, Miyazaki et al. (2018)), whereas the sky background commonly reaches a few thousand electrons after integrating a few minutes on an 8-m telescope. For LSST, it is anticipated that the background noise will dominate the sky noise in all bands (however marginally in *u* band) in 30 s exposures.
All pixels in the image affected by noise are statistically independent. When co-adding several exposures of the same field, one has to resample input images to the same pixel grid, which correlates neighboring pixels. Avoiding stacking is therefore preferable to ensure that pixels remain uncorrelated, which makes the noise bias correction tractable.

When an image is received from a detector, it is first divided by a flat image to ensure a flat sky background. The flat-field correction is used to remove artifacts present during image acquisition, due for example to dust in the detector or spatial variations of the sensor efficiency. These flat-field images are averages of uniform illuminations, such as the twilight sky or an illuminated screen inside the dome. The background level is then measured on the empty sky areas visible in the image, and the average of this measurement is subtracted off the image. Fluctuations of this background constitute the dominant source of noise in the image, and are usually approximated by a Gaussian with a null average.
This noise can affect astrophysical measurements in different ways, especially for images with a low SNR. Noise obviously contributes uncertainties to any measurement extracted from the image, for example position, flux or shape. For reasons detailed below, non-linear quantities, such as shape indicators, are usually biased by noise.

6.1.2 Impact on shear measurement

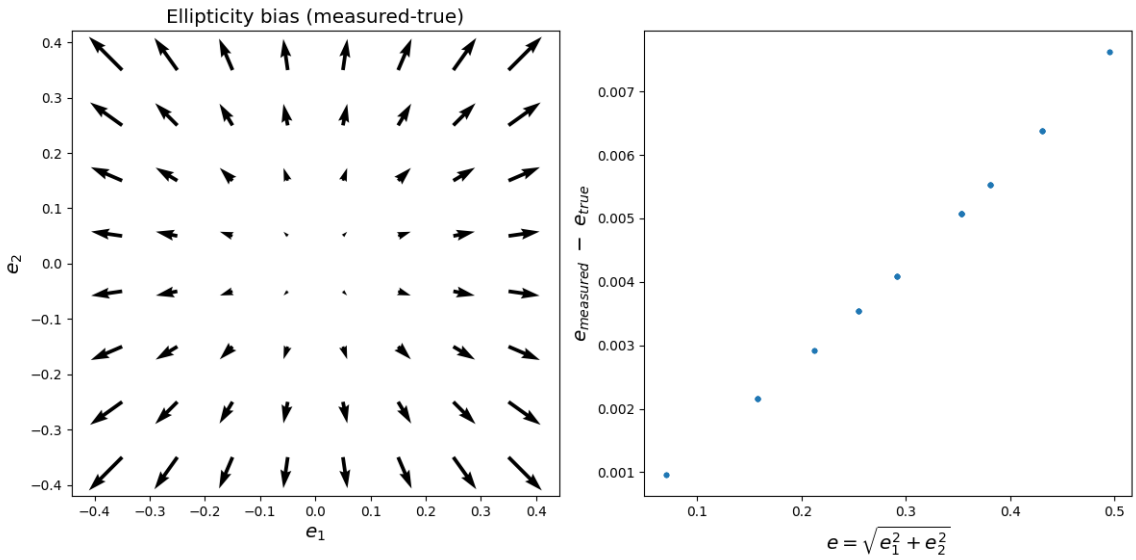

Figure 6.2: *Ellipticity bias measured on noisy images, as a function of the ellipticity parameters e_1 and e_2.*

"Bias" refers to the difference of some statistics of the data over an (infinite) ensemble of data realizations and the value of these statistics for noise-free data. Any non-linear function of the image pixels is in general biased (see R12) : if one expands this non-linear function in powers of the data, noise contributions to squares (or higher powers) of the data do not average out.
Whatever the shape estimation method, they are all biased by noise because of unavoidable non-linearities in their formalism.

In model fitting, the pixel noise affecting the ellipticity leads to a skewness of the likelihood, even in the case of a Gaussian or Poissonian noise (Melchior and Viola (2012), Refregier et al. (2012) (R12), Miller et al. (2013)). This bias is a complex function of SNR, galaxy size, ellipticity and PSF profile.

Moments-based methods are not safe either, since moments are not linear functions of the (noisy) galaxy centroid. Considering noisy galaxy images, the centroid uncertainty reflects the galaxy ellipticity. This means that the ellipticity measurement on a round galaxy is not really affected by the noise bias, because its moments suffer from equal noise bias, as opposed to a very elongated galaxy (see figure 6.2).

The effect of noise on shape measurement will introduce a multiplicative bias in the shear estimation (as it was mentioned in section 3.3.3). Even if the shape noise is the main source of bias in shear measurement, the noise bias needs a specific correction before performing estimations (while shape noise averages out over a large number of sources).
According to R12, if we consider galaxies with a given SNR, the noise bias affecting the different measured parameters (including centroid, flux and ellipticity) scales to first order as SNR^{-2}. For instance, if a galaxy has a SNR $\sim$10, the bias is $\sim$0.01, which is the same order of magnitude as the shear signal. In the case of LSST, this bias drops to $\sim$0.0025 (which is still 25% of the shear signal) since the SNR threshold is set to $\sim$20.

One obvious way to limit the effect of noise bias would be to only observe galaxies with higher SNR, but this solution is unrealistic since the faint galaxies (associated to low SNR values) dominate the brightness distribution.

Noise bias is particularly concerning for measurements that depend on comparing shear at different redshifts : growth rate of structures and dark energy parameters. Indeed, since high redshift galaxies are on average much fainter than closer ones, a poorly corrected noise bias translates into a redshift-dependent bias of the estimated shear signal.

In the following section, we describe the methods previously used to reduce and correct noise bias, for both model fitting and moment-based methods.

6.1.3 Noise bias calibration

Many noise bias correction methods were developed in the last 30 years, the most common being calibration with simulations.
This implies the simulation of artificial galaxy images with known properties on which we add realistic noise. We then apply the same shape measurement algorithm that is used on real data, and the noise bias calibration is just the difference between the input and the measured shape. Such procedures were performed in Mandelbaum et al. (2014) using the *GREAT3* image analysis challenge (with a known PSF), and in Fenech Conti et al. (2017) using the *lensfit* algorithm on the KiDS data. In this article, they also developed an empirical calibration function derived from the simulation to correct the ellipticities of real galaxies. Simulation-based calibration using the KSB algorithm on Euclid-like images was also performed in Hoekstra, Viola, and Herbonnet (2017), previously mentioned in section 4.1.3.
The models used for simulated-based calibrations are functions of the SNR and the galaxy size, and the main challenge when designing such calibrations is to assign the bias to these two parameters. Considering the *lensfit* algorithm, the separation of variables between galaxy size and SNR is quite tedious (Miller et al., 2013).

Bayesian inference for noise bias correction was also implemented in Bernstein and Armstrong (2014), where priors on galaxies and noise characteristics are incorporated in the measurement process, then the posterior distribution of galaxy shapes (given the noisy data) are estimated using Bayesian method. The Bayesian method was also investigated in Miller et al. (2013), also using *lensfit* to perform shear analysis on the CFHTLens data, but this method could not independently correct for noise bias and required calibration with simulations. The main issue of Bayesian inference is that they usually work for a specified sample with its own properties, so these corrections are no longer adequate if the selection function is changed.

Empirical noise bias calibrations using observational data were also explored, especially in Refregier and Bacon (2003). They decomposed galaxy images into shapelets-basis function, where the coefficients of the shapelets decomposition describe the shape and orientation of the galaxy. Noise properties are measured from empty sky regions on observational data, and used to adjust the coefficients of the shapelets decomposition. However, this method is not fully analytical since the noise bias is not detailed.

In view of all these methods and their associated limitations, we are exploring the possibility of developing an analytical noise bias calibration, based solely on the received galaxy image properties. A very recent work described in Li and Mandelbaum (2023) and Li et al. (2024) called *AnaCal* also explores an analytical approach to determine both the shear response and the noise bias correction. The method builds on the Fourier Power Function Shapelets (FPFS) technique, combined with an auto-differentiation (AD) method to calculate the second-order noise bias terms. In Li et al. (2024), the AD capability of *JAX* (Schoenholz and Cubuk, 2019) was used to calculate the noise bias correction, improving the previous results presented in Li and Mandelbaum (2023). This method has been tested on LSST-like simulations, with significant results in

terms of limiting multiplicative bias.
Analytical calibration has the dual advantage of not being subject to any assumptions about galaxy distribution or priors, and would also free us from the time-consuming Monte-Carlo procedures required for simulations. Particularly for next-generation surveys, the pour mil limit requires millions of galaxies for each point. The analytical noise bias calibration developed within this thesis is described in the next sections.

6.2 Analytical prediction of ellipticity noise bias

The noise bias of moment measurements can be traced down to the noise affecting the used image. However, in the context of several exposures of the same field, one improves the overall moment measurements by imposing a common position on all images, using some astrometric solutions. Is is then useful to consider separately the contribution to the noise bias of moments arising from position uncertainty, from those related to image pixels, because the position is not necessarily extracted from the same pixels as the moments. If we have 10 images of the same galaxy, we can choose to measure the shear on the last one, while the position has been determined by averaging the centroid measurements done on the other nine. In this case, there is no covariance between position and image, hence the importance of being able to separate these two variables. Moments can vary from image to image (because the PSF varies), while position should not. This more general setting also covers the case of a single image used to measure both position and moments.

As we measure the galaxy's position directly on the received - and noisy - image, it creates a bias in the second moments' calculation, as it was introduced in 6.1.2. This position is indeed re-injected into the pixel coordinates and the weight function W (see formula 4.8). This also introduces a bias in the flux measurement.
In this section, we will evaluate the possibility of establishing a noise bias correction using analytical formulas from the second order terms of the moments.

6.2.1 Analytical formula of position variance

When the image is affected by the noise, we can describe it as the sum of the original galaxy image and a noise image (that we call n). We assume that the pixels are affected by independent noise and that the noise is stationary :

$$Cov(n_i, n_j) = \delta_{ij}\sigma^2$$

with $E[n] = 0$.

The first thing we need to calculate is the variance of the position x_0, as it's involved in most of the terms in the global noise bias correction.

The position x_0 is estimated by canceling:

$$f(x_0, I) = \sum (x_i - x_0) W(x_i - x_0) I_i \tag{6.1}$$

where the sum runs over pixels, I is the image and W the weight function. The same calculation is done for y_0 be replacing $(x_i - x_0)$ by $(y_i - y_0)$. We will then continue to refer at x_i and x_0 as 2D position vectors including $[x_i, y_i]$ and $[x_0, y_0]$.

In order to evaluate the effect of image noise on the position estimation x_0, we should calculate :

$$\frac{\partial x_0}{\partial I_i} = -\frac{\partial f}{\partial I_i}\left[\frac{\partial f}{\partial x_0}\right]^{-1} \tag{6.2}$$

where the expression on the right comes from the implicit function theorem.

We assume a Gaussian weight function :

$$W(x - x_0) = e^{-\frac{1}{2}(x-x_0)^T M_W^{-1}(x-x_0)} \tag{6.3}$$

and its derivative with respect to x_0 :

$$\frac{dW}{dx_0} = M_W^{-1}(x - x_0)W(x - x_0) \tag{6.4}$$

We have :

$$\frac{\partial f}{\partial I_i} = (x_i - x_0)W_i \tag{6.5}$$

$$\begin{aligned}\frac{\partial f}{\partial x_0} &= -\sum WI + M_W^{-1}\sum (x_i - x_0)(x_i - x_0)^T WI \\ &= -F\mathbb{1} + M_W^{-1}M_P^* F\end{aligned} \tag{6.6}$$

with F the flux, i.e. the sum over the pixels of WI, and $M_P^* = M_P/F$ (P being the product between I and W).
By replacing 6.5 and 6.6 in 6.2, we therefore have :

$$\begin{aligned}\frac{\partial x_0}{\partial I_i} &= \frac{1}{F}[\mathbb{1} - M_W^{-1}M_P]^{-1}(x_i - x_0)W_i \\ &= K(x_i - x_0)W_i\end{aligned} \tag{6.7}$$

with M_W the second moment of W and M_P the second moment of P.

The noisy second moments can be re-expressed as follows :

$$M = \sum (x_i - x_0 - \delta x_0)(x_i - x_0 - \delta x_0)^T W(x_i - x_0 - \delta x_0)(I_i + \epsilon_i) \tag{6.8}$$

where ϵ is the noise image of variance σ^2_{noise} and :

$$\begin{aligned}\delta x_0 &= \frac{\partial x_0}{\partial I_i}\epsilon_i \\ &= K(x_i - x_0)W_i\epsilon_i\end{aligned} \tag{6.9}$$

We can then express the variance V of x_0 :

$$\begin{aligned}V &= \sigma(\epsilon_i)^2 \sum \frac{\partial x_0}{\partial I_k}\frac{\partial x_0^T}{\partial I_k} \\ &= \sigma^2_{noise} K \sum (x_k - x_0)(x_k - x_0)^T W_k^2 K \\ &= \sigma^2_{noise} K M_{W^2} K\end{aligned} \tag{6.10}$$

with M_{W^2} the second moments of W^2.

The analytical formula for the position variance is finally :

$$V = \sigma^2_{noise} K M_{W^2} K \tag{6.11}$$

In order to test the validity of the analytical position variance from equation 6.11, we compared it with the numerical variance calculated using simulations. Two tests were performed : comparisons between position variance and SNR, and between position variance and ellipticity. Numerically, x_0 and y_0 are determined by minimizing equation 6.1, the minimization target being 10^{-4}. This value represents a compromise between calculation time and accepted uncertainty on position variance. As the latter is measured in arcsec, a limit higher than 10^{-4} (e.g. 10^{-3}) creates an offset between the analytical prediction of the variance and the numerical value.

We performed all the tests with an average of $N = 10^4$ galaxies for each point, with Gaussian galaxies, PSF and weight function. The galaxies' σ is 0.4 arcsec, and PSF's σ is 0.34 arcsec (which corresponds to FWHM = 0.8 arcsec). The noise image added to the noise-free simulation is generated using a normal distribution, with σ going from 3.0 to 6.0 (which corresponds to SNR$\sim$35 and SNR$\sim$17.5) for the first test (see figure 6.3). It is fixed to 5.0 for the changing ellipticity tests (see figures 6.4 and 6.5), and the ellipticity parameters are varying between -0.3 and 0.3.

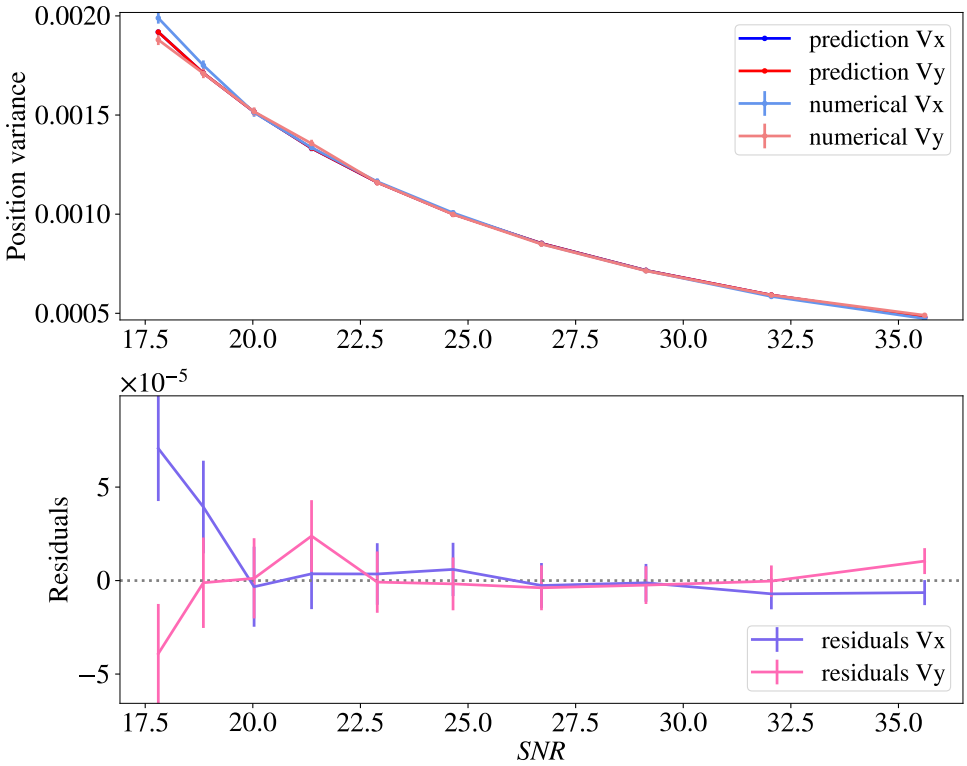

Figure 6.3: *Comparison between the analytical prediction and the numerical measurement of the position variance as a function of the signal-to-noise ratio. The averaging from the numerical calculation was done over 10^4 round galaxies.*

In figure 6.3, we see, not surprisingly, that position variance (V_x and V_y for the x_0 and y_0 variances respectively) increases as SNR decreases, with a value of the order of 0.0015 for SNR $\sim$ 20, which is the limit value set in LSST where most objects are observed. The residuals (here the absolute difference between the numerical and the analytical values of the quantity under consideration) are between 0 and 5×10^{-5}, corresponding to differences between 0.05% and 3.2%. The errors for the variances are calculated as follows : $\sigma_k = V_k\sqrt{2/N}$, with V_k corresponding to V_x or V_y.
It is also interesting to see how the variances evolve with the ellipticity, as we saw in

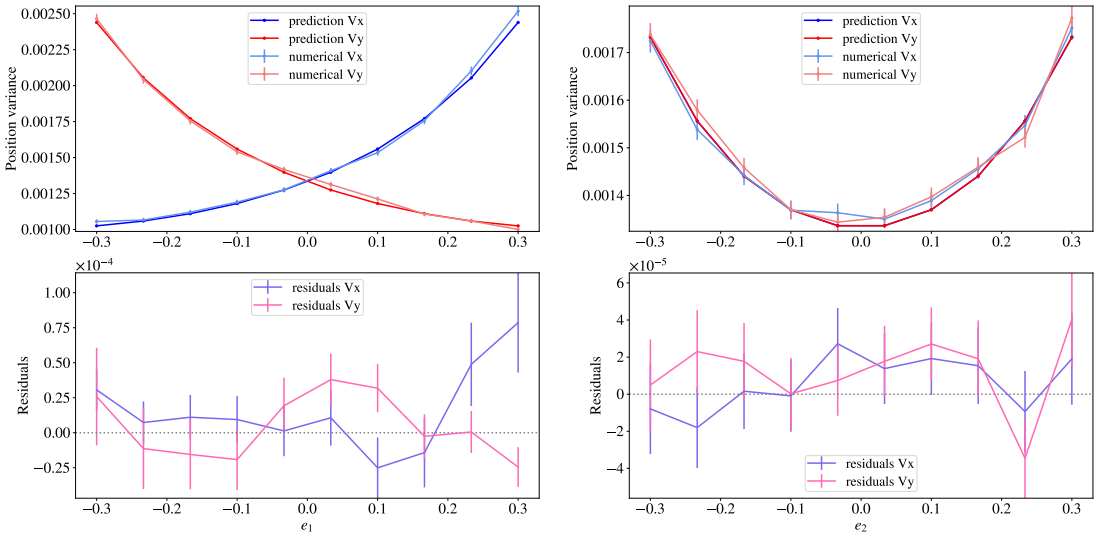

Figure 6.4: *Comparison between the analytical prediction and the numerical measurement of the position variance as a function of e_1 (left) and e_2 (right) for SNR = 21.*

figure 6.2 that the noise bias increases with ellipticity. We investigated three cases : e_1 varying only, e_2 varying only, and e_1 and e_2 varying simultaneously.
In figure 6.4 left, we see that both V_x and V_y are evolving together with opposite trends, with V_x low and V_y high for negative values of e_1, and vice versa. This result is fairly logical since the ellipticity is elongated along the y axis when e_1 is negative (see figure 2.7). We see however on the right panel that V_x and V_y are evolving the same way when e_2 is changing. A distortion with respect to e_2 makes the galaxy oriented at $\pm 45°$, which involves both axis x and y at the same time.

We see that the variance is higher when only e_1 is varying ($V \sim 0.0025$ for the extremal ellipticity values) than for e_2 ($V \sim 0.0017$), probably because the distortion is equally distributed along x and y in this last case, so the elongations are less important for both axes than with e_1 only.
When e_1 only is varying, the residuals are going from 0.1% to 3%, and when e_2 only is varying, the residuals are going from 0.04% to 3.2% both for V_x and V_y.

For the last test where e_1 and e_2 vary at the same time (see figure 6.5), we see that the position variance tendency is a combination of the two previous ones, when only one parameter is changing. The highest values of these variances are reaching

$\sim$0.003 for the extremal ellipticity values, and the residuals vary between 0.1% and 3% both for V_x and V_y.

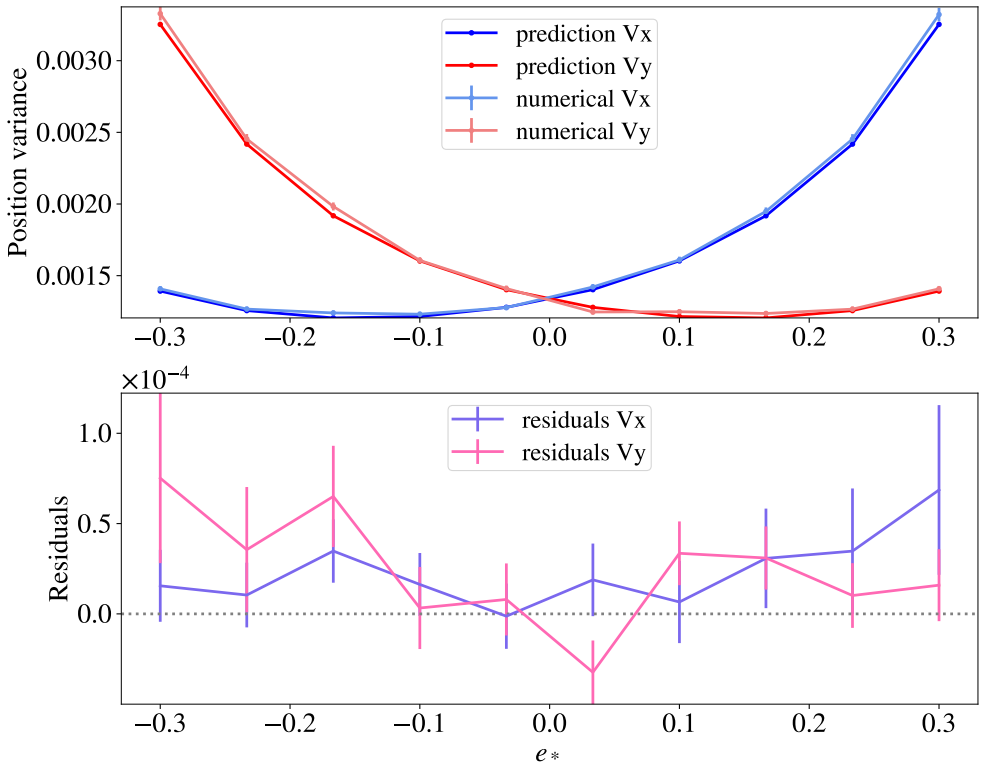

Figure 6.5: *Comparison between the analytical prediction and the numerical measurement of the position variance as a function of the ellipticity (e_1 and e_2 varying simultaneously, with SNR = 21).*

6.2.2 Analytical expression of the flux noise bias

Because we are working with normalized second moments, we also need to calculate the noise bias contribution to the image's flux. This formula will then be used to correct the norm of the second moments.

The flux is defined as follows :

$$F = \sum_k W_k I_k \tag{6.12}$$

Once again, we need to calculate both the second derivative with respect to x_0^2 and the second cross-derivative with respect to x_0 and I.

For greater clarity, we will use Greek indices to index the coordinate axes, and the 2-vector $(x_k - x_0)$ is replaced by x^k for brevity. The index k runs over image pixels.

To evaluate the bias, we will need to contract the expressions with the variance V of x_0 and with the covariance between x_0 and I_k, named C.

We have :

$$Cov(x_{0\gamma}, x_{0\delta}) = \sigma^2 (KM^2(W^2)K)_{\gamma\delta} \equiv V_{\gamma\delta}$$
$$Cov(x_{0\gamma}, I_k) = \sigma^2 K_{\gamma\rho} x_\rho^k W_k \equiv C_{\gamma k}$$

The bias associated to the position x_0 only is written :

$$\begin{aligned}
2B_1 &= \frac{\partial^2 F}{\partial x_{0\gamma} x_{0\delta}} V_{\gamma\delta} \\
&= V_{\gamma\delta} \sum_k W_{k,\gamma,\delta} I_k \\
&= V_{\gamma\delta} \sum_k -\delta_{\epsilon\delta} M^{-1}_{W\gamma\epsilon} W_k I_k + x_\epsilon^k M^{-1}_{W\gamma\epsilon} M^{-1}_{W\delta\eta} x_\eta^k W_k I_k \\
&= V_{\gamma\delta}(-M^{-1}_{W\gamma\delta} F + (M_W^{-1} m^P M_W^{-1})_{\gamma\delta}) \\
&= -F \ Tr(M_W^{-1} V) + Tr(M_W^{-1} m^P M_W^{-1} V)
\end{aligned}$$

where m^P is the un-normalized second moments of WI. We use $\sum_{ij} A_{ij} B_{ji} = Tr(AB)$. The cross-derivative term gives :

$$\begin{aligned}
B2 &= \frac{\partial^2 F}{\partial x_{0\gamma} I_k} C_{\gamma k} \\
&= M^{-1}_{W\gamma\epsilon} \sum_k x_\epsilon^k W_k K_{\gamma\rho} x_\rho^k W_k \\
&= M^{-1}_{W\epsilon\gamma} K_{\gamma\rho} M^2(W^2)_{\rho\epsilon} \\
&= Tr(M_W^{-1} K M^2(W^2))
\end{aligned}$$

Finally, the total flux bias is defined as :

$$B_F = B_1 + B_2 \tag{6.13}$$

The contributions to B_1 and B_2 to B_F are shown in figure 6.6.

To test the validity of the flux noise bias B_F, we will compare it to numerical bias from simulation, in the manner of the position variance. We averaged over $N = 10^5$ galaxies for each point, with the same random and opposite pairs of intrinsic ellipticities procedure to cancel the shape noise. The parameters of the simulations are similar to the ones of the position variance's tests, i.e. Gaussians galaxies with a σ = 0.4 and Gaussian PSF with σ = 0.34. The noise image is also generated using a normal distribution, with σ going from 3.0 to 5.0 (which corresponds to SNR=32 and SNR=21). For all the following plots, the errors are calculated using : $\sigma_k = \sqrt{V_k/N}$, where V_k is the variance of the quantity under consideration.

Figures 6.7 and 6.8 show on the top panel the difference between the flux measured on the noisy image and the true flux in blue, the analytical prediction of the noise bias B_F in red, and the residuals on the bottom panel. In figure 6.7, the analytical prediction was calculated from noise-free simulations, while it was calculated using the noisy images in figure 6.8, as it should be done in realistic conditions. We see that there is no big difference between the two approaches.

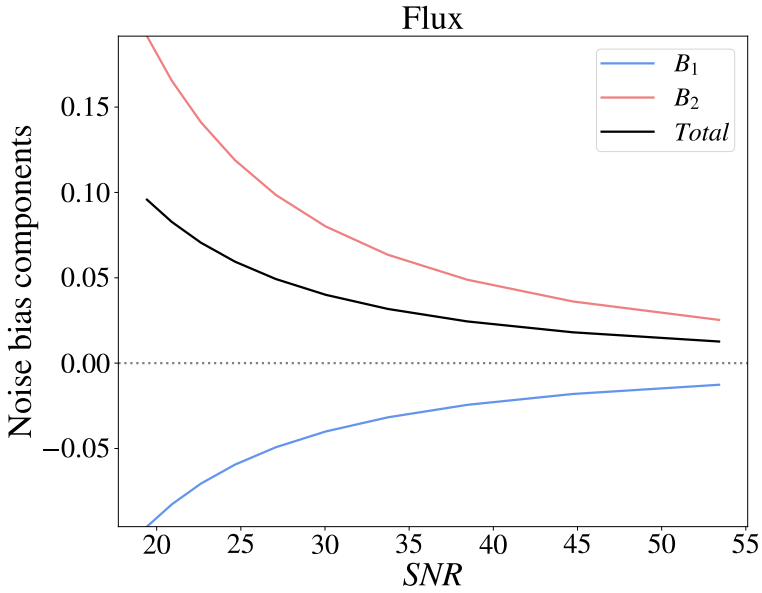

Figure 6.6: *Contributions of B_1 and B_2 in the flux noise bias for a round galaxy.*

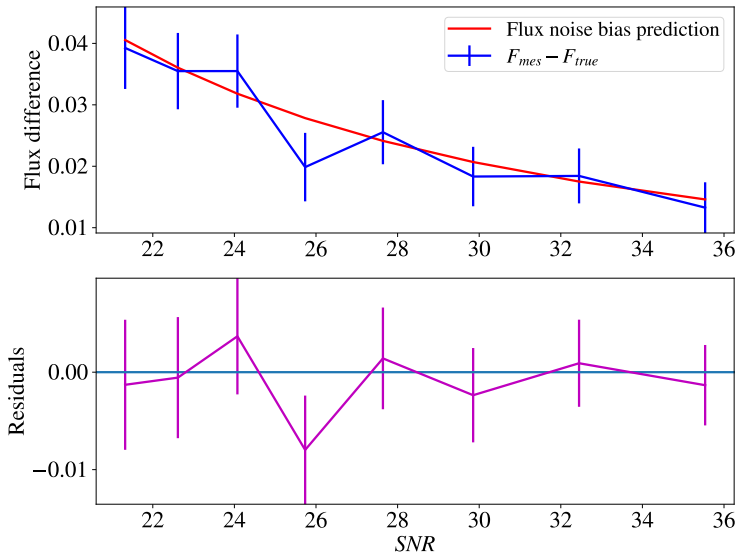

Figure 6.7: *Comparison between the analytical prediction and the numerical measurement of the image's flux as a function of the SNR. The noise bias correction was calculated on the noise-free simulations*

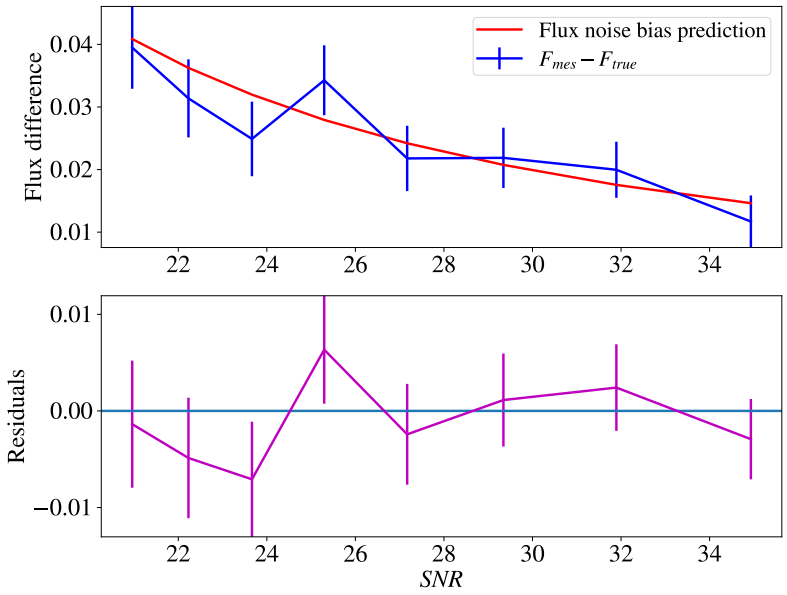

Figure 6.8: *Comparison between the analytical prediction and the numerical measurement of the image's flux as a function of the SNR. The noise bias correction was calculated on the noisy simulations*

6.2.3 Analytical expression of the second moments noise bias

The second moment is not a linear function of the data, i.e. the image's pixels, due to the x_0 dependency of the weight function W and reduced coordinates $(x-x_0)(x-x_0)^T$. The bias affecting the second moments can be estimated by evaluating the second derivatives of the moment with respect to the image, considering the dependence of the position x_0 on the image :

$$\begin{aligned} m_P(I+n) = m_P(I) + \sum_k \frac{\partial m_P}{\partial I_k} n_k + \frac{\partial m_P}{\partial x_0}\delta x_0 \\ + \frac{1}{2}\sum_{kl} \frac{\partial^2 m_P}{\partial I_k \partial I_l} n_k n_l + \sum_k \frac{\partial^2 m_P}{\partial I_k \partial x_0} n_k \delta x_0 + \frac{1}{2}\frac{\partial^2 m_P}{\partial x_0^2}\delta x_0 \delta x_0 \\ + \dots \end{aligned} \tag{6.14}$$

As we are evaluating the average over an ensemble of realizations, and we assume the mean of the noise to be zero, the linear terms involved in the second moments derivative disappear. It is only necessary to calculate the quadratic terms, in other words $\partial^2 m_P/\partial x_0^2$ and $\partial^2 m_P/\partial I_k \partial x_0$. Because the image is linear, the second derivative of the moments with respect to I_k^2 cancels out.
We should keep in mind that higher order terms may contribute a bias, but the next contribution scales as SNR^{-4} and is hopefully negligible. If it is not, Monte-Carlo tests should indicate it clearly, because of the specific SNR dependence.

There are 4 factors involved in the definition of the second moments m_P :

$$m^P_{\alpha\beta} = \sum_k x^k_\alpha x^k_\beta W_k I_k$$

where $x_k - x_0$ has been replaced by x_k. We need to calculate the second derivatives of these terms, the first three factors depending only on x_0 and the last only on I.

We define :

$$\begin{aligned} x^k_{\alpha,\beta} &\equiv \partial x^k_\alpha / \partial x_{0\beta} \\ &= -\delta_{\alpha\beta} \end{aligned}$$

$$\begin{aligned} W_{k,\gamma} &\equiv \partial W_k / \partial x_{0\gamma} \\ &= M^{-1}_{W\gamma\epsilon} x^k_\epsilon W_k \end{aligned}$$

$$\begin{aligned} W_{k,\gamma,\delta} &\equiv \partial W_{k,\gamma} / \partial x_{0\delta} \\ &= -M^{-1}_{W\gamma\epsilon}\delta_{\epsilon\delta} W_k + M^{-1}_{W\gamma\epsilon} x^k_\epsilon W_{k,\delta} \\ &= -M^{-1}_{W\gamma\epsilon}\delta_{\epsilon\delta} W_k + M^{-1}_{W\gamma\epsilon} x^k_\epsilon M^{-1}_{W\delta\eta} x^k_\eta W_k \end{aligned}$$

We have :

$$\frac{\partial^2 m^P_{\alpha\beta}}{\partial x_{0\gamma}\partial x_{0\delta}} = T^{12}_{\alpha\beta\gamma\delta} + T^{13}_{\alpha\beta\gamma\delta} + T^{23}_{\alpha\beta\gamma\delta} + T^{33}_{\alpha\beta\gamma\delta} \tag{6.15}$$

where the upper indices of the T's refer to the terms to be derived (x_α, x_β, W_k or I_k).

With :

$$\begin{aligned} T^{12}_{\alpha\beta\gamma\delta} &\equiv \sum_k (x^k_{\alpha,\gamma} x^k_{\beta,\delta} + x^k_{\alpha,\delta} x^k_{\beta,\gamma}) W_k I_k \\ &= (\delta_{\alpha\gamma}\delta_{\beta\delta} + \delta_{\alpha\delta}\delta_{\beta\gamma}) F \end{aligned}$$

$$\begin{aligned} T^{13}_{\alpha\beta\gamma\delta} &\equiv \sum_k (x^k_{\alpha,\gamma} x^k_\beta W_{k,\delta} + x^k_{\alpha,\delta} x^k_\beta W_{k,\gamma}) I_k \\ &= -\sum_k (\delta_{\alpha\gamma} x^k_\beta M^{-1}_{W\delta\epsilon} x^k_\epsilon + \delta_{\alpha\delta} x^k_\beta M^{-1}_{W\gamma\epsilon} x^k_\epsilon) W_k I_k \\ &= -m^P_{\beta\epsilon}(M^{-1}_{W\epsilon\delta}\delta_{\alpha\gamma} + M^{-1}_{W\epsilon\gamma}\delta_{\alpha\delta}) \end{aligned}$$

$$T^{23}_{\alpha\beta\gamma\delta} = T^{13}_{\beta\alpha\gamma\delta}$$

$$\begin{aligned} T^{33}_{\alpha\beta\gamma\delta} &\equiv \sum_k x^k_\alpha x^k_\beta W_{k,\gamma,\delta} I_k \\ &= -M^{-1}_{W\gamma\delta} m^P_{\alpha\beta} + M^4_{\alpha\beta\epsilon\eta}(WI) M^{-1}_{W\gamma\epsilon} M^{-1}_{W\delta\eta} \end{aligned}$$

where we define the fourth-order moment of an image:

$$M^4_{\alpha\beta\epsilon\eta}(A) = \sum_k x^k_\alpha x^k_\beta x^k_\epsilon x^k_\eta A_k$$

For the crossed second derivatives of the moment, we write :

$$\frac{\partial^2 m^P_{\alpha\beta}}{\partial x_{0\gamma}\partial I_k} = T^{14}_{\alpha\beta\gamma k} + T^{24}_{\alpha\beta\gamma k} + T^{34}_{\alpha\beta\gamma k}$$

with

$$T^{14}_{\alpha\beta\gamma k} \equiv x^k_{\alpha,\gamma} x^k_\beta W_k = -\delta_{\alpha\gamma} x^k_\beta W_k \tag{6.16}$$

$$T^{24}_{\alpha\beta\gamma k} = T^{14}_{\beta\alpha\gamma k} \tag{6.17}$$

$$T^{34}_{\alpha\beta\gamma k} \equiv x^k_\alpha x^k_\beta W_{k,\gamma} = x^k_\alpha x^k_\beta x^k_\epsilon M^{-1}_{W\epsilon\gamma} W_k$$

We can now contract these expressions with the variance V and covariance C. By defining $T^{12}_{\alpha\beta} = T^{12}_{\alpha\beta\gamma\delta} V_{\gamma\delta}$, we finally find :

$$T^{12}_{\alpha\beta} = 2FV_{\alpha\beta}$$

$$T^{13}_{\alpha\beta} = -2(VM^{-1}_W m_P)_{\alpha\beta}$$

$$T^{23}_{\alpha\beta} = T^{13}_{\alpha\beta}$$

$$T^{33}_{\alpha\beta} = -m^P_{\alpha\beta} Tr(M^{-1}_W V) + M^4(WI)_{\alpha\beta\epsilon\eta}(M^{-1}_W V M^{-1}_W)_{\epsilon\eta}$$

We can clarify the expression :

$$M^4_{\alpha\beta\epsilon\eta}(A)B_{\epsilon\eta} = \begin{bmatrix} M^4_{x^4}(A)B_{xx} + 2M^4_{x^3y}(A)B_{xy} + M^4_{x^2y^2}(A)B_{yy} & M^4_{xy^3}B_{yy} + 2M^4_{x^2y^2}(A)B_{xy} + M^4_{x^3y}(A)B_{xx} \\ M^4_{xy^3}B_{yy} + 2M^4_{x^2y^2}(A)B_{xy} + M^4_{x^3y}(A)B_{xx} & M^4_{y^4}(A)B_{yy} + 2M^4_{xy^3}(A)B_{xy} + M^4_{x^2y^2}(A)B_{xx} \end{bmatrix}$$

Terms involving odd moments are only zero in the case where the image A has no xy moment or the matrix B matrix is diagonal.

We can now calculate the cross-derivative bias including the covariance C :

$$\begin{aligned} T^{14}_{\alpha\beta} &= \sum_k -\delta_{\alpha\gamma} x^k_\beta W_k \sigma^2 K_{\gamma\rho} x^k_\rho W_k \\ &= -\sigma^2 M_{W^2,\beta\rho} K_{\rho\alpha} \\ &= -\sigma^2 (M_{W^2} K)_{\alpha\beta} \end{aligned}$$

$$T^{24}_{\alpha\beta} = T^{14}_{\alpha\beta}$$

$$\begin{aligned} T^{34}_{\alpha\beta} &= \sum_k x^k_\alpha x^k_\beta x^k_\epsilon M^{-1}_{W\epsilon\gamma} W_k \sigma^2 K_{\gamma\rho} x^k_\rho W_k \\ &= \sigma^2 M^4(W^2)_{\alpha\beta\epsilon\rho}(M^{-1}_W K)_{\epsilon\rho} \end{aligned}$$

Note that M_{W^2} represents the second moments of W^2.
For a well-sampled Gaussian weight, the relationship between the fourth-order moments and the second-order moments of a Gaussian means that $2T^{14} = -T^{34}$ and therefore the cross-derivative terms do not contribute to the bias.

Finally, the total bias (measured second moments minus true second moments) is written :

$$B_M = \frac{1}{2}(T^{12} + 2T^{13} + T^{33}) + 2T^{14} + T^{34} \tag{6.18}$$

Figures 6.9 and 6.10 shows the prediction for e_1 and e_2 respectively (i.e. the difference between B_M^{xx} and B_M^{yy} and $2B_M^{xy}$). The predictions were calculated on noise-free images, with exact positions and second moments. We see that the correction is approximately null when the galaxy is round (as expected because the more a galaxy is round, the less it is affected by noise bias, see figure 6.2) and goes up to $\sim 10^{-2}$ when the galaxy is elliptical (which represent $\sim 1\%$ of the un-normalized second moments). The fact that the noise bias prediction is small compared to the moment value is a good thing, as it means that prediction calculations on noisy images will also be reliable (given that the moment bias is also of the order of 1%).

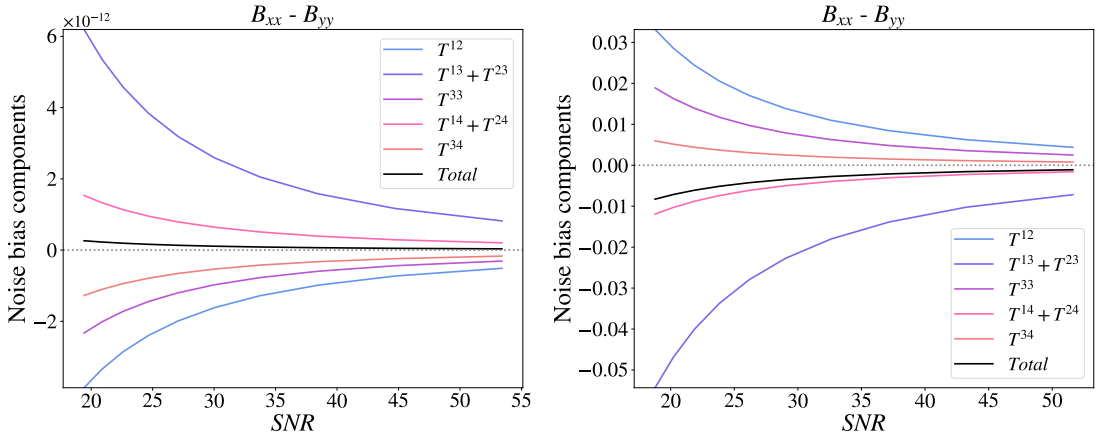

Figure 6.9: *Contributions of all the different terms of the numerator of e_1 noise bias for a round galaxy (left) and an elliptical (e_1 = 0.2 ; e_2 = -0.3) galaxy (right)*

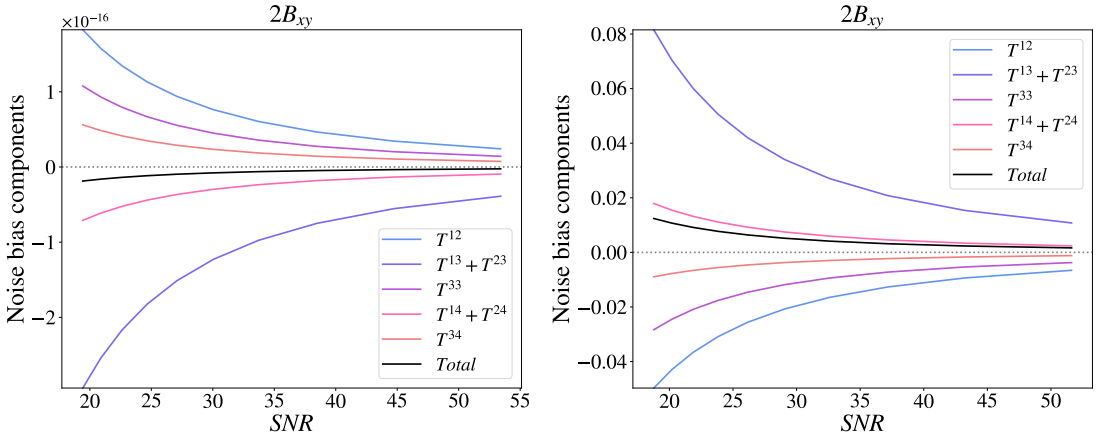

Figure 6.10: *Contributions of all the different terms of the numerator of e_2 noise bias for a round galaxy (left) and an elliptical (e_1 = 0.2 ; e_2 = -0.3) galaxy (right)*

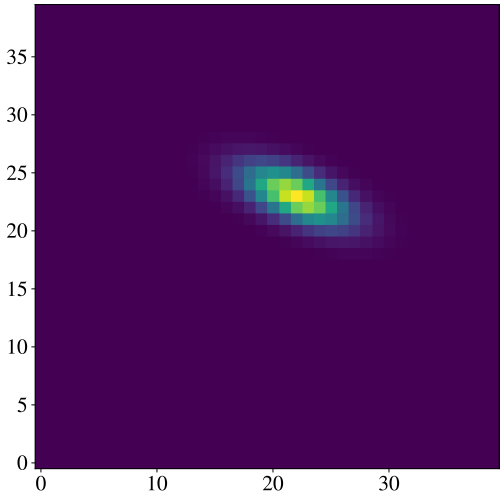

Figure 6.11: *Galaxy profile chosen to test the noise bias predictions on ellipticity.*

We can now apply these noise bias predictions to the second moments, in order to correct the ellipticity. We will first check the efficiency of the correction on the three parameters of the second moments, i.e. M_{xx}, M_{yy} and M_{xy}. The seconds moments are corrected with the prediction B_M, and divided by the measured flux (the sum over the pixel of IW) corrected by the prediction B_F :

$$M_c = \frac{M_{mes} - B_M}{F_{mes} - B_F} \tag{6.19}$$

We performed the simulations over 10^5 galaxies for each point, for noisy simulations going from SNR = 20 to SNR = 34. The Gaussian galaxy model used for the simulations has a σ = 0.4 arcsec, and a fixed intrinsic ellipticity of $[e_1 = 0.3; e_2 = -0.3]$.

Because we want to check the noise bias correction on the ellipticity, we don't want to cancel the shape noise anymore, for this reason we chose a single intrinsic ellipticity. The PSF is still fixed to a Gaussian with $\sigma = 0.34$ arcsec.

We see in figures 6.12, 6.13 and 6.14 that the three components of second moments are satisfactorily corrected from the noise bias. Not surprisingly, the bias affecting M_{xx} is greater compared to the other second moments terms, which can be explained by the chosen galaxy ellipticity. As it can be seen in figure 6.11, the galaxy is more elongated along the x axis, which explains a bigger bias in this direction. We also saw earlier that the position variance is increasing with ellipticity.

We can now verify the efficiency of the noise bias correction directly on the ellipticity components e_1 and e_2. As a reminder, $e_1 = M_{xx} - M_{yy}$ and $e_2 = 2M_{xy}$, with M normalized by the flux. We see in figure 6.15 and 6.16 that e_1 and e_2 respectively are well corrected from the noise bias, which was expected given the satisfactory results of the second moments.

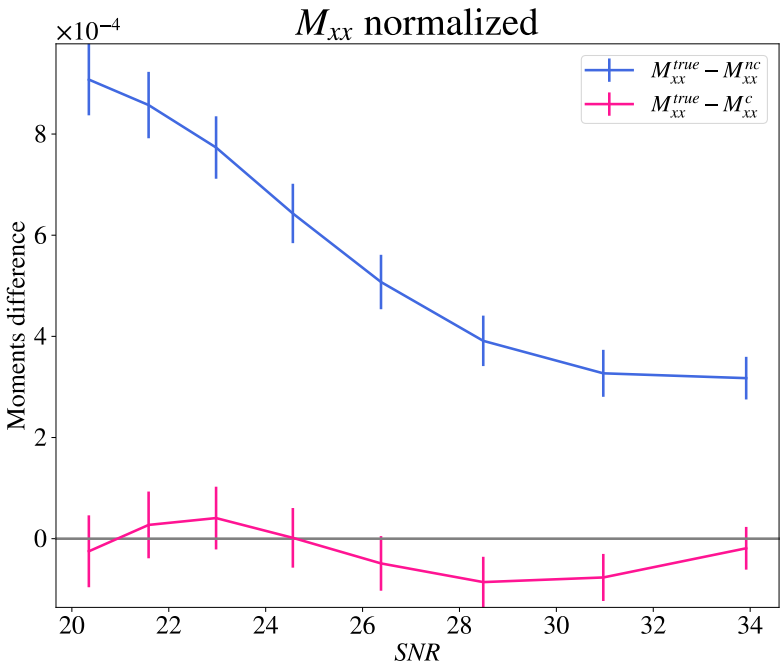

Figure 6.12: *Difference between the true M_{xx} and the noisy one in blue, and between the true M_{xx} and the corrected one in pink.*

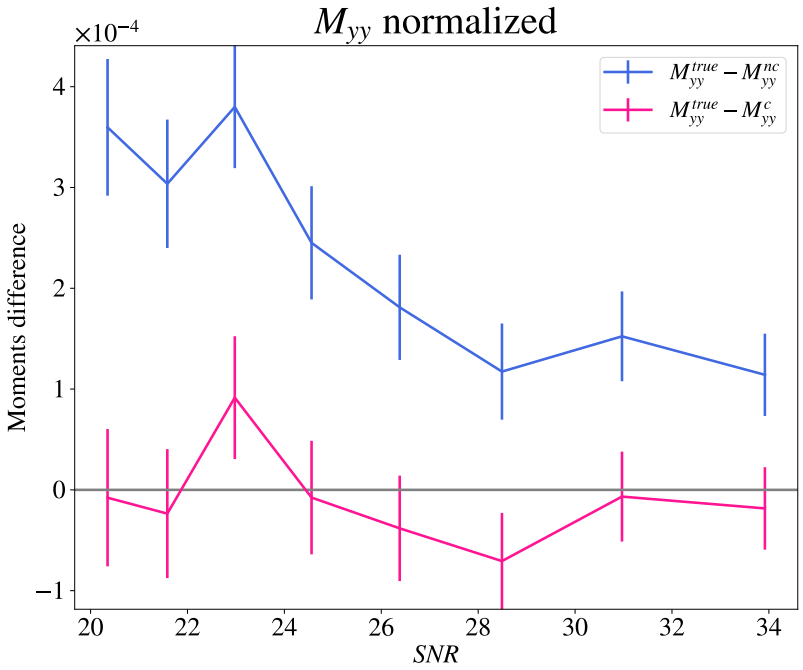

Figure 6.13: *Difference between the true M_{yy} and the noisy one in blue, and between the true M_{yy} and the corrected one in pink.*

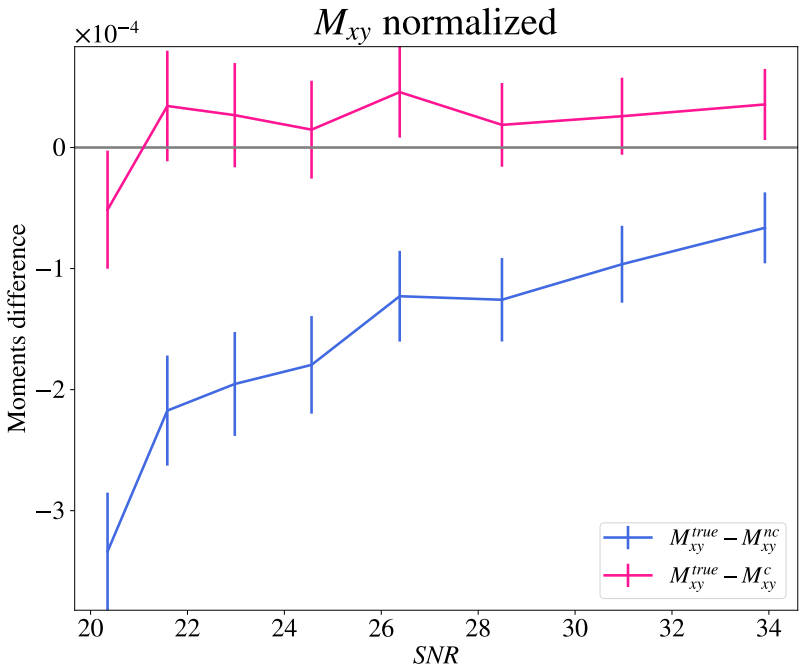

Figure 6.14: *Difference between the true M_{xy} and the noisy one in blue, and between the true M_{xy} and the corrected one in pink.*

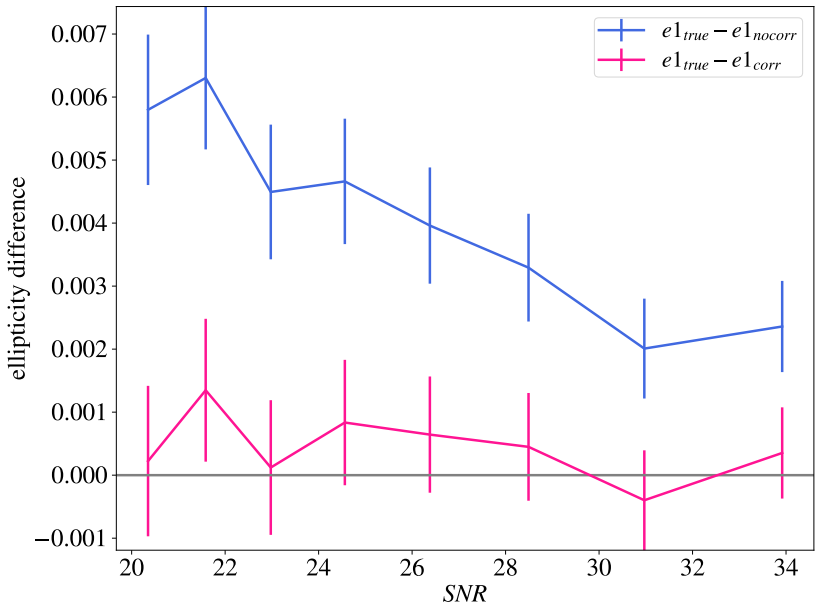

Figure 6.15: *First parameter of ellipticity e_1 calculated from second moments measured on noisy images without correction (blue) and corrected thanks to the analytical noise bias prediction (pink).*

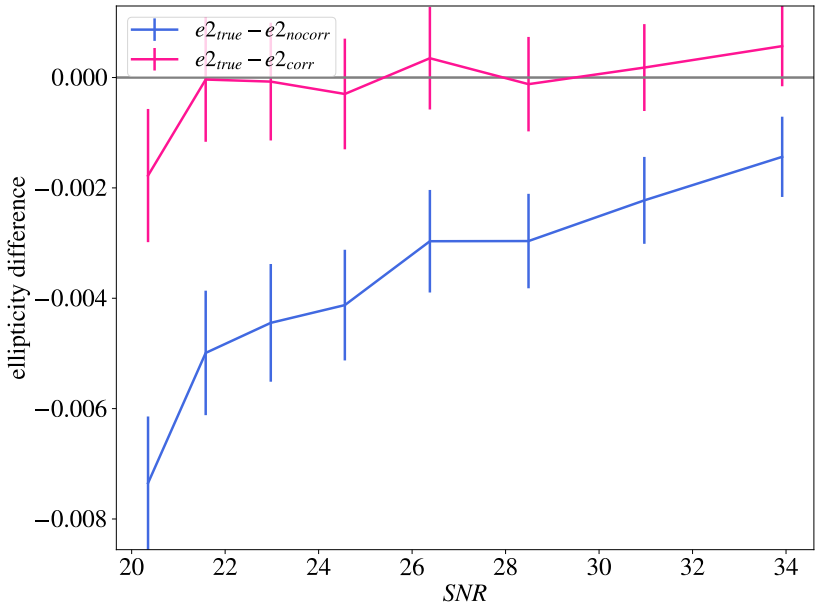

Figure 6.16: *Second parameter of ellipticity e_2 calculated from second moments measured on noisy images without correction (blue) and corrected thanks to the analytical noise bias prediction (pink).*

6.3 Analytical prediction of calibration factor noise bias

Now that we've corrected ellipticity, we also need to calculate the noise bias correction for the calibration factor R. This implies calculating the second derivatives of the *distorted* moments M^S involved in the derivatives (equations 6.21, 6.22).
Because the coordinates system is distorted, we can no longer dissociate the unnormalized moments and the flux corrections, since they are both affected by the shear, and so correlated. In the next section, we'll look at attempts to calculate noise bias analytically on normalized moments, and the limits we face.

6.3.1 Distorted normalized second moments noise bias

For greater clarity, we recall below the equations involved in the definition of R, introduced in section 4.2.1:

$$\mathbf{R} = \begin{pmatrix} \frac{\partial e_1}{\partial g_1} & \frac{\partial e_2}{\partial g_1} \\ \frac{\partial e_1}{\partial g_2} & \frac{\partial e_2}{\partial g_2} \end{pmatrix} = \begin{pmatrix} \frac{\partial M_{xx}}{\partial g_1} - \frac{\partial M_{yy}}{\partial g_1} & \frac{2\partial M_{xy}}{\partial g_1} \\ \frac{\partial M_{xx}}{\partial g_2} - \frac{\partial M_{yy}}{\partial g_2} & \frac{2\partial M_{xy}}{\partial g_2} \end{pmatrix} \tag{6.20}$$

where the second moments' derivatives with respect to the shear $\partial M/\partial g$ are defined numerically :

$$\frac{\partial M}{\partial g_1} = \frac{M^{1+} - M^{1-}}{2\epsilon} \tag{6.21}$$

$$\frac{\partial M}{\partial g_2} = \frac{M^{2+} - M^{2-}}{2\epsilon} \tag{6.22}$$

In the following, we will often refer to the distorted second moments components using these notations :

- M^S : distorted second moments matrix
- M^{1+} : distorted second moments matrix with $+\epsilon$ applied on g_1 in the shear matrix S (can also be M^{1-}, M^{2+} or M^{2-}, see equation 4.28 for the expression of S)
- M^{1+}_{xx} : first component of the distorted matrix M^{1+} (can also be M^S_{xy} or M^S_{yy})

Note that all the second moments involved in R are normalized by the flux.

We can re-write equation 4.21 as a function of M^S :

$$\mathbf{R} = \frac{1}{2\epsilon} \begin{pmatrix} R_{11} & R_{12} \\ R_{21} & R_{22} \end{pmatrix} \tag{6.23}$$

with :

$$R_{11} = (M_{xx}^{1+} - M_{xx}^{1-}) - (M_{yy}^{1+} - M_{yy}^{1-}) \tag{6.24}$$
$$R_{12} = 2(M_{xy}^{1+} - M_{xy}^{1-}) \tag{6.25}$$
$$R_{21} = (M_{xx}^{2+} - M_{xx}^{2-}) - (M_{yy}^{2+} - M_{yy}^{2-}) \tag{6.26}$$
$$R_{22} = 2(M_{xy}^{2+} - M_{xy}^{2-}) \tag{6.27}$$

In order not to overload the notations, we'll continue to use the same formalism as the one introduced in section 6.2.3 to calculate the noise bias : we keep m_P to define the un-normalized second moments.

The bias of the quantity m_P/F is evaluated here. This is not trivial because the two quantities have correlated fluctuations that need to be evaluated. The approach is the same as for moment and flux, but applied to the m_P/F combination. Here too, we need to calculate the second derivatives with respect to x_0 and I_k and contract them with the corresponding variances or covariances. These second derivatives can essentially be expressed using what we've already seen.

The expression of the second derivative of X with respect to two variables x and y is written :

$$\begin{aligned}\frac{\partial^2(m_P F^{-1})}{\partial x \partial y} = &\frac{\partial^2 m_P}{\partial x \partial y} F^{-1} - \frac{1}{F^2}\left[\frac{\partial m_P}{\partial x}\frac{\partial F}{\partial y} + \frac{\partial m_P}{\partial y}\frac{\partial F}{\partial x}\right] \\ &- \frac{\partial^2 F}{\partial x \partial y}\frac{m_P}{F^2} + \frac{2m_P}{F^3}\frac{\partial F}{\partial x}\frac{\partial F}{\partial y}\end{aligned} \tag{6.28}$$

This expression must be evaluated for (x,y) equal to (x_0,x_0), (x_0,I_k) and (I_k,I_k). Terms involving second derivatives are calculated above. We only develop the products of first derivatives here :

$$\begin{aligned}\frac{\partial m_{\alpha\beta}^P}{\partial x_{0\gamma}} &= -2\delta_{\alpha\gamma}\sum_k x_\beta^k W_k I_k + M_{W^{\gamma\epsilon}}^{-1}\sum_k x_\alpha^k x_\beta^k x_\epsilon^k W_k I_k \\ \frac{\partial F}{\partial x_{0\gamma}} &= M_{W^{\gamma\epsilon}}^{-1}\sum_k x_\epsilon^k W_k I_k \\ \frac{\partial m_{\alpha\beta}^P}{\partial I_k} &= x_\alpha^k x_\beta^k W_k \\ \frac{\partial F}{\partial I_k} &= W_k\end{aligned} \tag{6.29}$$

The first two expressions are practically null : On the one hand, $\sum_k x^k W_k I_k = 0$ is the definition of the position x_0, and on the other hand, the expression of the 3rd-order

moment $\sum_k x^k x^k x^k W_k I_k$ is strictly null for an exactly even galaxy, and very weak in general.
Among the primary derivative products, we still have :

$$\frac{\partial m^P_{\alpha\beta}}{\partial I_k}\frac{\partial F}{\partial I_k} = x^k_\alpha x^k_\beta W^2_k$$
$$\frac{\partial F}{\partial I_k}\frac{\partial F}{\partial I_k} = W^2_k \tag{6.30}$$

After removing all canceling terms, the total bias on m_P/F is therefore :

$$B_{mF^{-1}} = \frac{B_M}{F} - \frac{B_F m_P}{F^2} - \frac{\sigma^2_{noise}}{F^2} M^2_{W^2} + \frac{\sigma^2_{noise}}{F^3} m_P \sum_k W^2_k \tag{6.31}$$

where B_F and B_M are the noise bias analytical predictions for the flux (see equation 6.13) and for the un-normalized second moments (see equation 6.18) respectively.

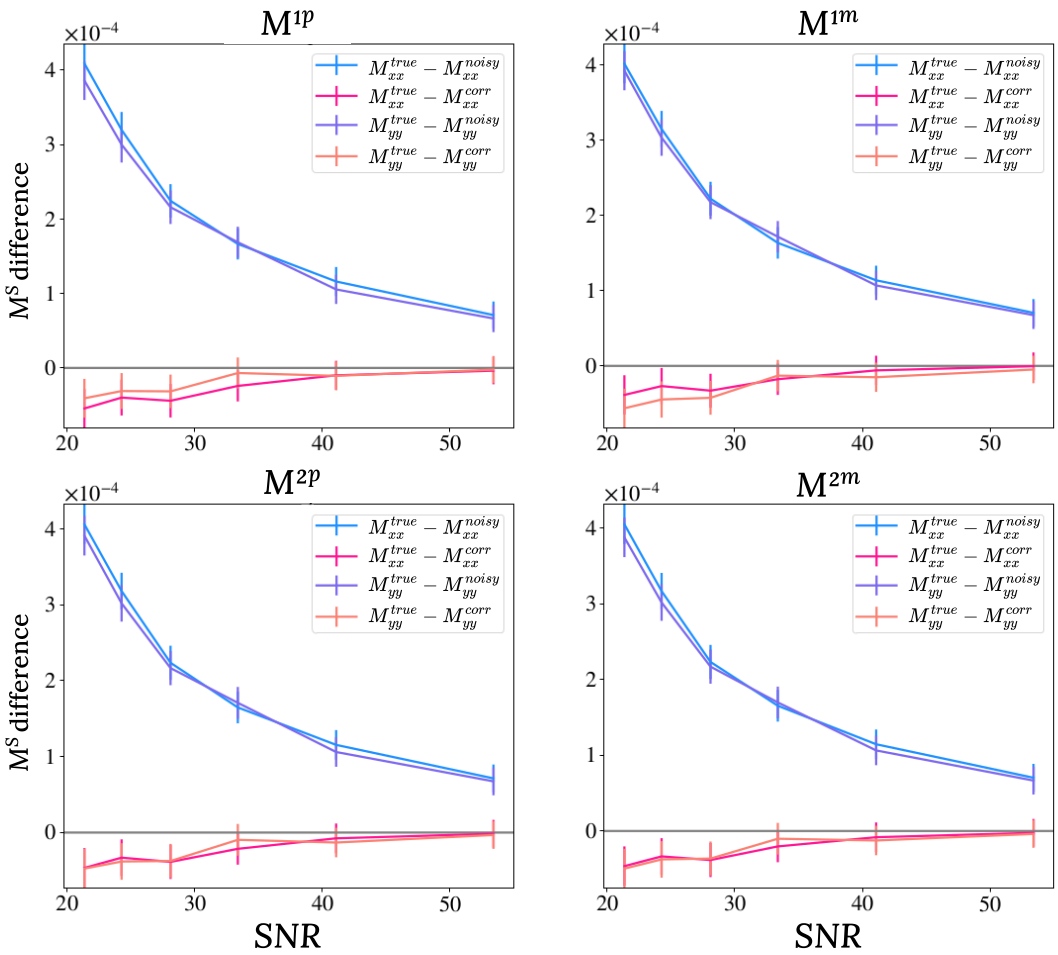

Figure 6.17: *Difference between the true M^S and the noisy one in blue/purple, and between the true M^S and the corrected one in pink/orange. The numerator (distorted second moments) and the denominator (flux) are corrected separately using formulas 6.18 and 6.13.*

Figure 6.17 shows the difference between the true and noisy distorted second moments (*xx* in blue and *yy* in purple), and the difference between the true and the corrected (*xx* in pink and *yy* in orange). In these plots, the second moments' numerator and denominator are corrected separately using formula 6.18 for the numerator and formula 6.13 for the denominator, as it was performed for the ellipticity. We see that even if the corrected moments components are less biased than the uncorrected ones, separate predictions for the un-normalized moments and the flux are no longer sufficient. A residual bias still affects the distorted second moments, especially at low SNR. For this reason, we use therefore the global correction, taking the moments already normalized by the flux.

The same analysis but using the global correction (formula 6.31) is shown in figure 6.18. We can see that prediction on the normalized moments corrects noise bias very well, unlike the separate predictions seen above.

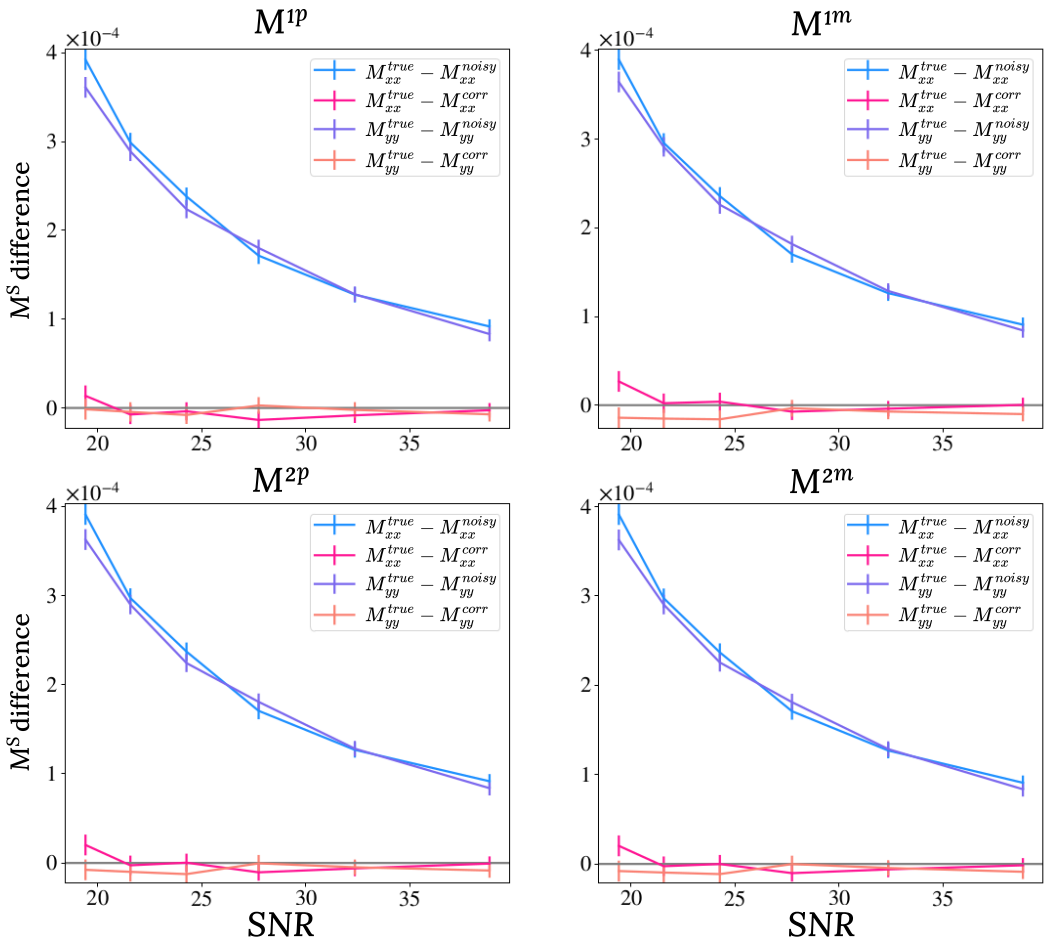

Figure 6.18: *Difference between the true M^S and the noisy one in blue/purple, and between the true M^S and the corrected one in pink/orange. The normalized distorted moments are corrected using equation 6.31. Each point is averaged over 5e5 galaxies.*

However, whatever the chosen convention for the correction (separated or global), we see that none of them correctly corrects the calibration factor R from the noise bias. Figure 6.19 shows R calculated from the M^S corrected with the separate prediction, and figure 6.20 R calculated from the M^S corrected with the global prediction. We see no big difference between these two analyses, and more than that, the correction in both cases is at least three times higher than expected. These results suggest that most of the biases affecting the M^S cancel each other out, but the difference always includes a bias (and/or is over-corrected), whatever the configuration chosen for the correction.

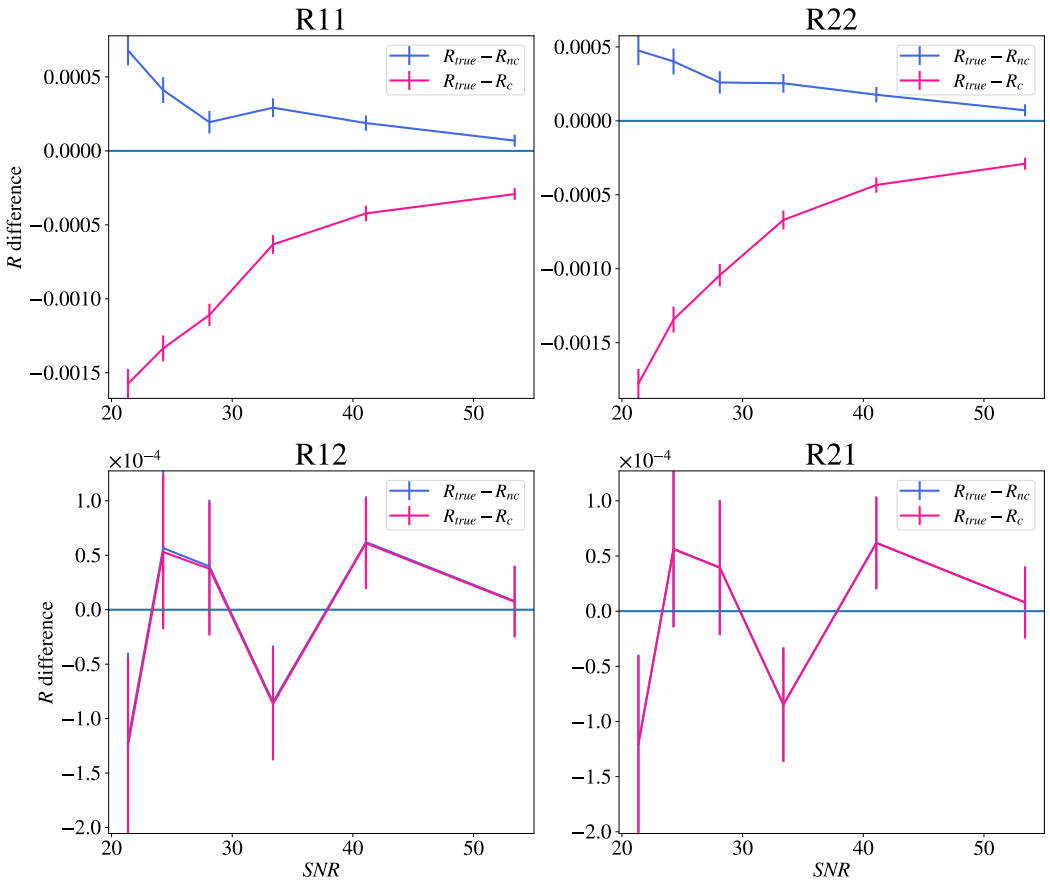

Figure 6.19: *Difference between the true R and the noisy one in blue, and between the true R and the corrected one in pink. The noise bias correction was done using equations 6.18 and 6.13. Each point is averaged over* $5e5$ *galaxies.*

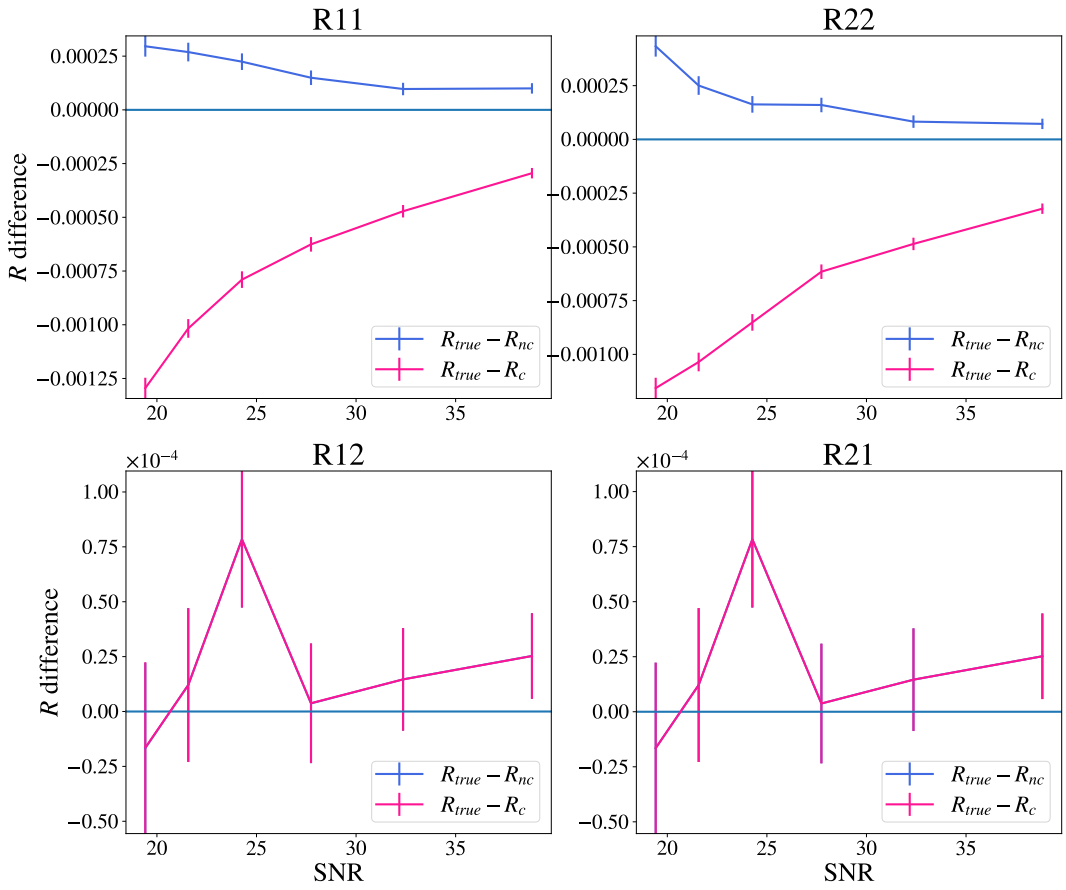

Figure 6.20: *Difference between the true R and the noisy one in blue, and between the true R and the corrected one in pink. The noise bias correction was done using 6.31. Each point is averaged over 5e5 galaxies.*

According to figures 6.19 and 6.20, we see that R_{12} and R_{21} are not biased. Figure 6.21 shows the differences between true ΔM^S, the noisy ΔM^S, and the corrected ΔM^S. Here we show only the ΔM^S involved in R_{11} and R_{22} :

$$\Delta^*_{xx} = M^{1+}_{xx} - M^{1-}_{xx} \tag{6.32}$$
$$\Delta^*_{yy} = M^{1+}_{yy} - M^{1-}_{yy} \tag{6.33}$$
$$\Delta^*_{xy} = M^{1+}_{xy} - M^{1-}_{xy} \tag{6.34}$$

We see that, in addition to $M^{2p}_{xy} - M^{2m}_{xy}$, the two differences involved in R_{11} are also biased, one positively and the other negatively. Since we subtract them, these biases add up instead of canceling each other out, as seen in the corrected R_{11}.

No solution has yet been found to explain this over-correction of the distorted second moments differences. As suggested in the conclusion of section 4, if we can manage

to perform the moments' derivatives with respect to the shear in Fourier space by developing the PSF on analytical functions, some covariances between flux and moments due to grid distortion may disappear, facilitating the calculation of noise bias prediction.

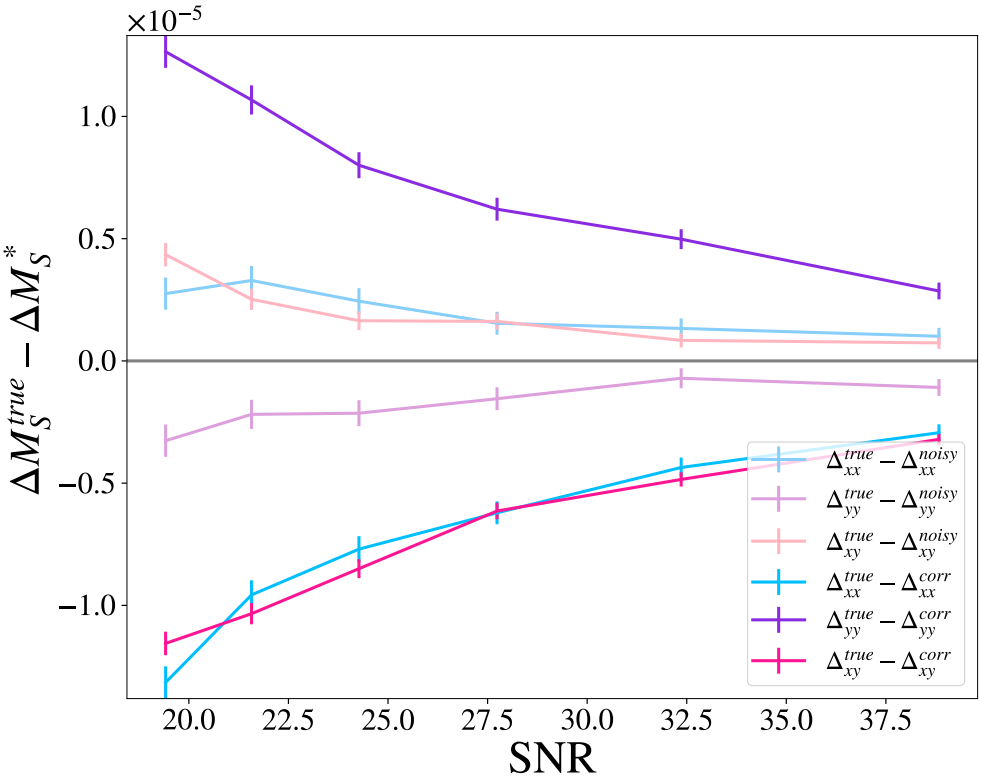

Figure 6.21: *Difference between the true ΔM^S and the noisy one in faded colors, and between the true ΔM^S and the corrected one in bright colors. The differences involving the xx terms are in blue, yy in purple and xy in pink. Each point is averaged over $5 \cdot 10^5$ galaxies.*

6.4 Conclusion and perspectives

In this section, we introduced the concept of noise bias, its origins and how it can affect shape and shear measurements.
The usual simulation-based methods used to correct this bias in shear analysis suffer from limitations, including dependence on modeling assumptions, difficulty in separating the main parameters involved in bias (galaxy size and SNR), or significant computation time.
To address this, we attempted to develop a new noise bias correction method based on analytically-calculated predictions. This method consists in calculating the second-order terms of the quantities affected by the noise bias, i.e. the un-normalized second moments, the flux, and the second moments normalized by the flux. We separate the

second derivatives with respect to x_0 and I, as these two variables can be uncorrelated in real conditions.

As the error in sources position measurement is causing the noise bias (because the second moments are quadratic functions of position), we first calculated the analytical position variance prediction. After comparison with simulations, this formula appears to accurately represent the variance measured numerically.
We then calculated the predictions for the un-normalized second moments and the flux in order to correct the ellipticity components. Both flux and moments predictions are correctly correcting their respective quantity, and so these predictions also successfully correct the ellipticity. This first result is very satisfying and promising, but it is just the first ingredient to perform a shear analysis.

We then need to perform the same kind of correction for the calibration factor R, probably because of the pixel grid distortion that correlates the moments and the flux. However, the separated flux and moments correction no longer works to predict the noise bias affecting the distorted second moments involved in R. We therefore used a global noise bias prediction where the second-order terms were calculated directly on the normalized moments. But even if this new prediction better corrects the distorted moments, their differences suffer from a residual bias, or an over-correction. Hence, the calibration factor is not well corrected from noise bias, and the prediction seems to be three times too high on R_{11} and R_{22}.
In addition to the possibility of calculating analytical derivatives with respect to shear, two areas for improvement are being considered to improve the R noise:

- The first one consists in calculating the real analytical second derivatives (maybe including higher-order terms that are non-trivial) using a Python software like *JAX* (Schoenholz and Cubuk, 2019), which allows to do differentiable physics simulations with primitive operations compiled on CPU, GPU or TPU.

- The second option is to calculate the predictions using numerical derivatives (similar to the shear derivatives described in section 4.2.1) by artificially inserting little position offsets before measuring the moments. The main challenge lies in finding a clever way to calculate the derivative with respect to the image.

The work on the R noise bias prediction is still a work in progress, but all the work done on developing this new analytical correction method has given very encouraging and promising results that are worth exploring further.

Conclusion

Since cosmic shear was first observed in 2000, it has become a key cosmological probe and promises to deliver exquisite dark energy constraints. Data from future-generation surveys like Vera C. Rubin Observatory (LSST) will pave the way for precision cosmology, with unprecedented coverage and galaxy density.

However, shear is inferred from coherent distortions of galaxy shapes, and the relation between galaxy ellipticities and gravitational shear is a serious potential source of bias. To perform precision cosmology analyses, and according to the statistics of future surveys like LSST, these biases should be tiny : the maximum multiplicative bias affecting the shear measurement is about 10^{-3}, and the additive one at 10^{-4}. These biases can have multiple sources, including a poorly calibrated shear estimator, or the pixel noise affecting the images.

To address the shear estimation method issue, we developed a shear estimator that makes no assumption on galaxy shapes, in order to avoid the shortcomings of a simulation-based shear calibration. We based our method on the galaxy images' weighted second moments to measure their ellipticities, and then rely on a perturbative procedure to relate these ellipticities to shear, given the local PSF. To perform such a calibration, the idea is to calculate the numerical derivatives of the second moments with respect to the shear by introducing shear variations into images. We reap several benefits from this method : (1), using second moments allows us to make no assumptions about galaxy profiles, (2) as opposed to the state of the art of shear measurement *Metacalibration*, the shear distortion are not applied on the original galaxy image deconvolved from the PSF (such procedure introduces correlated noise) but to the other terms of the estimator, i.e. the product of the pixel coordinates and the weight function convolved with the PSF. This global function is more extended and better resolved than the original image, allowing shear measurement to be performed on undersampled images (3).

During the development of this estimator, we noticed a bias in the shear measurement, especially affecting the first parameter g_1. Because we are working on sampled images, the measured second moments receive a contribution from the image sampling.

However, we distort the pixel grid in order to introduce the shear variations into the images that will be used to calculate the numerical derivatives of the second moments. This coordinate system's distortion is in fact the source of the observed bias, which is the result of a cross-effect between shear and sampling. By performing a limited development of the second moments as a function of shear and sampling, we were able to isolate the terms responsible for this bias and determine a correction depending on the galaxy size and PSF profile. One way of improving this method would be to develop the PSF on a set of eigenfunctions of the harmonic oscillator, in order to calculate the derivatives analytically in Fourier space. This would probably be a faster solution, and would perhaps make it possible to get rid of the shear and sampling bias.

We tested this method on different sets of simulations using the *GalSim* package, going from very basic galaxy models to realistic profiles from the *COSMOS* catalog. The conclusion of all these tests was that the bias affecting the shear estimations was controlled under the fixed limit of 10^{-3}, for all the tested profiles and with realistic size ratios values between the galaxy and the PSF. Nevertheless, these estimations were performed using noise-free simulations, which is another source of bias that we have to take into account.

Indeed, the pixel noise into the received images is introducing a bias, particularly for the low-SNR samples (which will dominate the LSST catalog because of their high redshift and faint surface brightness), and which increases with ellipticity. This bias comes from the noisy measurement of the galaxy position that we re-inject into the pixel coordinates of our system, and that we use to center the weight function. Usually corrected thanks to simulated-based calibrations, these methods suffer from the hypothesis made to generate the simulations and from heavy Monte Carlo procedure. Another part of this thesis was to try to develop an analytical correction to this noise bias by calculating the second order terms of the moments' Taylor expansion, which are affected by the noise. We achieved fairly satisfying results for the ellipticity calibration following this method, by calculating two separate corrections for the moments and for the flux (by which we normalize the moments). Although this is sufficient for ellipticity, this no longer works for the calibration factor because of its dependency on second moments calculated on a distorted pixel grid, which introduced a correlation between them and the flux. We calculated the noise bias directly on the normalized second moments, but we didn't achieved a correction as good as for the ellipticity. We investigated several hypothesis, including the distortion of some terms resulting from the cross derivative between the position and the image, but the results were not conclusive. This method is nonetheless promising, and prospects for further improvements are envisaged : either calculating the exact derivative maybe including higher order terms that we neglected using a Python software (like JAX), or to perform numerical derivatives for the noise bias prediction.

Despite the limitations we have faced and the prospects for improvements, the work carried out during this thesis is a step forward for future shear analyses on data from surveys such as LSST, enabling us to make per mil estimations and enter the era of precision cosmology.

Bibliography

Abbott, T. M. C. et al. (Jan. 2022). In: Phys. Rev. D 105.2, 023520, p. 023520. arXiv: 2105.13549 [astro-ph.CO] (page 26).

Akiyama, Kazunori and Event Horizon Telescope Collaboration (June 2022). In: *American Astronomical Society Meeting #240*. Vol. 240. American Astronomical Society Meeting Abstracts, 211.03, p. 211.03 (page 44).

Alpher, Ralph A. and Robert C. Herman (Apr. 1950). In: *Reviews of Modern Physics* 22.2, pp. 153–212 (page 18).

Amon, A. et al. (Jan. 2022). In: Phys. Rev. D 105.2, 023514, p. 023514. arXiv: 2105.13543 [astro-ph.CO] (pages x, xv, 25, 26).

Astier, P. et al. (Feb. 2006). In: A&A 447.1, pp. 31–48. arXiv: astro-ph/0510447 [astro-ph] (page 20).

Bacon, David J., Alexandre R. Refregier, and Richard S. Ellis (Oct. 2000). In: MNRAS 318.2, pp. 625–640. arXiv: astro-ph/0003008 [astro-ph] (pages 33, 64).

Bartelmann, M. and P. Schneider (Jan. 2001). In: Phys. Rep. 340.4-5, pp. 291–472. arXiv: astro-ph/9912508 [astro-ph] (pages x, 34).

Bellm, Eric C. et al. (Jan. 2019). In: PASP 131.995, p. 018002. arXiv: 1902.01932 [astro-ph.IM] (page 20).

Bernstein, G. M. and M. Jarvis (Feb. 2002). In: AJ 123.2, pp. 583–618. arXiv: astro-ph/0107431 [astro-ph] (pages 62, 73).

Bernstein, Gary M. (Aug. 2010). In: MNRAS 406.4, pp. 2793–2804. arXiv: 1001.2333 [astro-ph.IM] (page 61).

Bernstein, Gary M. and Robert Armstrong (Feb. 2014). In: MNRAS 438.2, pp. 1880–1893. arXiv: 1304.1843 [astro-ph.CO] (page 97).

Betoule, M. et al. (Aug. 2014). In: A&A 568, A22, A22. arXiv: 1401.4064 [astro-ph.CO] (page 20).

Bridle, Sarah et al. (Jan. 2009). In: *Annals of Applied Statistics* 3, pp. 6–37. arXiv: 0802.1214 [astro-ph] (pages x, 60).

Brout, Dillon et al. (Oct. 2022). In: ApJ 938.2, 110, p. 110. arXiv: 2202.04077 [astro-ph.CO] (page 24).

Cairós, Luz M. et al. (Aug. 2003). In: ApJ 593.1, pp. 312–332.
arXiv: astro-ph/0306307 [astro-ph] (pages x, 48).
Chang, C. et al. (Sept. 2013). In: MNRAS 434.3, pp. 2121–2135.
arXiv: 1305.0793 [astro-ph.CO] (page 54).
Chwolson, O. (June 1924). In: *Astronomische Nachrichten* 221, p. 329 (page 30).
Crittenden, Robert G. et al. (Mar. 2002). In: ApJ 568.1, pp. 20–27.
arXiv: astro-ph/0012336 [astro-ph] (page 40).
Cropper, Mark et al. (June 2013). In: MNRAS 431.4, pp. 3103–3126.
arXiv: 1210.7691 [astro-ph.IM] (page 56).
Davis, Tamara M. et al. (Nov. 2011). In: ApJ 741.1, 67, p. 67.
arXiv: 1012.2912 [astro-ph.CO] (page 7).
DES Collaboration et al. (Jan. 2024).
In: *arXiv e-prints*, arXiv:2401.02929, arXiv:2401.02929.
arXiv: 2401.02929 [astro-ph.CO] (page 24).
DESI Collaboration et al. (Apr. 2024).
In: *arXiv e-prints*, arXiv:2404.03002, arXiv:2404.03002.
arXiv: 2404.03002 [astro-ph.CO] (pages 12, 23).
Eddington, A. S. (Mar. 1919). In: *The Observatory* 42, pp. 119–122 (page 30).
Einstein, Albert (Jan. 1908).
In: *Jahrbuch der Radioaktivität und Elektronik* 4, pp. 411–462 (page 3).
— (Jan. 1915). In: *Sitzungsberichte der Königlich Preußischen Akademie der Wissenschaften*, pp. 844–847 (page 4).
Event Horizon Telescope Collaboration et al. (Apr. 2019). In: ApJ 875.1, L4, p. L4.
arXiv: 1906.11241 [astro-ph.GA] (page 44).
Fenech Conti, I. et al. (May 2017). In: MNRAS 467.2, pp. 1627–1651.
arXiv: 1606.05337 [astro-ph.CO] (pages 63, 97).
Fixsen, D. J. (Dec. 2009). In: ApJ 707.2, pp. 916–920.
arXiv: 0911.1955 [astro-ph.CO] (pages 16, 18).
Gamow, G. (Aug. 1948). In: *Physical Review* 74.4, pp. 505–506 (page 18).
Gavazzi, G. et al. (July 2010). In: A&A 517, A73, A73.
arXiv: 1003.3795 [astro-ph.CO] (page 45).
Guy, J. et al. (Apr. 2007). In: A&A 466.1, pp. 11–21.
arXiv: astro-ph/0701828 [astro-ph] (page 20).
Hamana, Takashi et al. (Feb. 2020). In: PASJ 72.1, 16, p. 16.
arXiv: 1906.06041 [astro-ph.CO] (pages xv, 26, 33).
Heymans, Catherine et al. (May 2006). In: MNRAS 368.3, pp. 1323–1339.
arXiv: astro-ph/0506112 [astro-ph] (page 64).
Heymans, Catherine et al. (Nov. 2012). In: MNRAS 427.1, pp. 146–166.
arXiv: 1210.0032 [astro-ph.CO] (page 56).
Heymans, Catherine et al. (Feb. 2021). In: A&A 646, A140, A140.
arXiv: 2007.15632 [astro-ph.CO] (pages x, 25).
Hildebrandt, H. et al. (Feb. 2017). In: MNRAS 465.2, pp. 1454–1498.
arXiv: 1606.05338 [astro-ph.CO] (page 33).
Hirata, Christopher and Uroš Seljak (Aug. 2003). In: MNRAS 343.2, pp. 459–480.
arXiv: astro-ph/0301054 [astro-ph] (pages 62, 76, 134).

Hoekstra, Henk, Massimo Viola, and Ricardo Herbonnet (July 2017).
In: MNRAS 468.3, pp. 3295–3311. arXiv: 1609.03281 [astro-ph.CO]
(pages 64, 97).
Hubble, E. P. (Dec. 1926). In: ApJ 64, pp. 321–369 (page 46).
Hubble, Edwin (Mar. 1929).
In: *Proceedings of the National Academy of Science* 15.3, pp. 168–173
(pages ix, 8).
Huterer, Dragan et al. (Feb. 2006). In: MNRAS 366.1, pp. 101–114.
arXiv: astro-ph/0506030 [astro-ph] (page 56).
Jarvis, Mike et al. (Feb. 2021).
Astrophysics Source Code Library, record ascl:2102.024 (page 26).
Jee, M. James and J. Anthony Tyson (May 2011). In: PASP 123.903, p. 596.
arXiv: 1011.1913 [astro-ph.IM] (page 52).
Kaiser, Nick (July 2000). In: ApJ 537.2, pp. 555–577.
arXiv: astro-ph/9904003 [astro-ph] (page 64).
Kaiser, Nick, Gordon Squires, and Tom Broadhurst (Aug. 1995). In: ApJ 449, p. 460.
arXiv: astro-ph/9411005 [astro-ph] (pages 62, 65).
Kaiser, Nick, Gillian Wilson, and Gerard A. Luppino (Mar. 2000).
In: *arXiv e-prints*, astro-ph/0003338, astro–ph/0003338.
arXiv: astro-ph/0003338 [astro-ph] (page 33).
Kilbinger, Martin (July 2015).
In: *Reports on Progress in Physics* 78.8, 086901, p. 086901.
arXiv: 1411.0115 [astro-ph.CO] (pages x, 38).
Klimov, Yu. G. (Aug. 1963). In: *Soviet Physics Doklady* 8, p. 119 (page 31).
Krause, E. and C. M. Hirata (Nov. 2010). In: A&A 523, A28, A28.
arXiv: 0910.3786 [astro-ph.CO] (page 40).
Leavitt, Henrietta S. and Edward C. Pickering (Mar. 1912).
In: *Harvard College Observatory Circular* 173, pp. 1–3 (page 8).
Léget, P. F. et al. (June 2021). In: A&A 650, A81, A81.
arXiv: 2103.09881 [astro-ph.IM] (page 57).
Lemaître, G. (Jan. 1927).
In: *Annales de la Société Scientifique de Bruxelles* 47, pp. 49–59
(page 8).
Lewis, Antony (Sept. 2009). In: MNRAS 398.1, pp. 471–476.
arXiv: 0901.0649 [astro-ph.GA] (page 62).
Li, Xiangchong and Rachel Mandelbaum (June 2023).
In: MNRAS 521.4, pp. 4904–4926. arXiv: 2208.10522 [astro-ph.CO]
(page 97).
Li, Xiangchong et al. (Apr. 2022). In: PASJ 74.2, pp. 421–459.
arXiv: 2107.00136 [astro-ph.CO] (page 25).
Li, Xiangchong et al. (Dec. 2023). In: Phys. Rev. D 108.12, 123518, p. 123518.
arXiv: 2304.00702 [astro-ph.CO] (page 41).
Li, Xiangchong et al. (Feb. 2024). In: MNRAS 527.4, pp. 10388–10396.
arXiv: 2309.06506 [astro-ph.CO] (page 97).
Liebes, Sidney (Feb. 1964). In: *Physical Review* 133.3B, pp. 835–844 (page 31).

Mandelbaum, Rachel et al. (May 2014). In: ApJS 212.1, 5, p. 5.
arXiv: 1308.4982 [astro-ph.CO] (page 97).
Mandelbaum, Rachel et al. (July 2015). In: MNRAS 450.3, pp. 2963–3007.
arXiv: 1412.1825 [astro-ph.CO] (page 76).
Mandelbaum, Rachel et al. (Jan. 2018). In: PASJ 70, S25, S25.
arXiv: 1705.06745 [astro-ph.CO] (pages 25, 79).
Massey, Richard et al. (Mar. 2007). In: MNRAS 376.1, pp. 13–38.
arXiv: astro-ph/0608643 [astro-ph] (page 64).
Mather, J. C. et al. (May 1990). In: ApJ 354, p. L37 (pages ix, 6, 17).
Melchior, P. and M. Viola (Aug. 2012). In: MNRAS 424.4, pp. 2757–2769.
arXiv: 1204.5147 [astro-ph.IM] (page 96).
Miller, L. et al. (Nov. 2007). In: MNRAS 382.1, pp. 315–324.
arXiv: 0708.2340 [astro-ph] (page 61).
Miller, L. et al. (Mar. 2013). In: MNRAS 429.4, pp. 2858–2880.
arXiv: 1210.8201 [astro-ph.CO] (pages 63, 96, 97).
Miyatake, Hironao et al. (Dec. 2023). In: Phys. Rev. D 108.12, 123517, p. 123517.
arXiv: 2304.00704 [astro-ph.CO] (pages x, 25).
Miyazaki, Satoshi et al. (Jan. 2018). In: PASJ 70, S1, S1 (page 95).
Paczynski, B. (May 1986). In: ApJ 304, p. 1 (page 16).
Peacock, John A. (1999) (page 11).
Penzias, A. A. and R. W. Wilson (July 1965). In: ApJ 142, pp. 419–421 (page 18).
Perlmutter, S. and B. P. Schmidt (2003). In: *Supernovae and Gamma-Ray Bursters*. Ed. by K. Weiler. Vol. 598, pp. 195–217 (pages ix, 10).
Perlmutter, S. et al. (June 1999). In: ApJ 517.2, pp. 565–586.
arXiv: astro-ph/9812133 [astro-ph] (page 9).
Planck Collaboration et al. (Nov. 2014). In: A&A 571, A1, A1.
arXiv: 1303.5062 [astro-ph.CO] (page 6).
Planck Collaboration et al. (Sept. 2020). In: A&A 641, A6, A6.
arXiv: 1807.06209 [astro-ph.CO] (pages x, xv, 9, 16, 25).
Pujol, Arnau et al. (Sept. 2020). In: A&A 641, A164, A164.
arXiv: 1707.01285 [astro-ph.CO] (page 58).
Refregier, Alexandre and Adam Amara (Apr. 2014).
In: *Physics of the Dark Universe* 3, pp. 1–3. arXiv: 1303.4739 [astro-ph.CO] (page 63).
Refregier, Alexandre and David Bacon (Jan. 2003). In: MNRAS 338.1, pp. 48–56.
arXiv: astro-ph/0105179 [astro-ph] (page 97).
Refregier, Alexandre et al. (Sept. 2012). In: MNRAS 425.3, pp. 1951–1957.
arXiv: 1203.5050 [astro-ph.CO] (page 96).
Refsdal, S. (Jan. 1964). In: MNRAS 128, p. 307 (page 31).
Riess, Adam G. et al. (Sept. 1998). In: AJ 116.3, pp. 1009–1038.
arXiv: astro-ph/9805201 [astro-ph] (page 9).
Riess, Adam G. et al. (July 2022). In: ApJ 934.1, L7, p. L7.
arXiv: 2112.04510 [astro-ph.CO] (page 9).
Roberts, Morton S. (May 1966). In: ApJ 144, p. 639 (page 46).
Roddier, F. (Jan. 1981). In: *Progess in Optics* 19, pp. 281–376 (page 50).

Rowe, B. T. P. et al. (Apr. 2015). In: *Astronomy and Computing* 10, pp. 121–150.
arXiv: 1407.7676 [astro-ph.IM] (pages 63, 76).
Rubin, David et al. (Nov. 2023).
In: *arXiv e-prints*, arXiv:2311.12098, arXiv:2311.12098.
arXiv: 2311.12098 [astro-ph.CO] (page 24).
Rubin, V. C. (June 1983). In: *Science* 220.4604, pp. 1339–1344 (page 46).
Sarkar, Prakash et al. (Oct. 2009). In: MNRAS 399.1, pp. L128–L131.
arXiv: 0906.3431 [astro-ph.CO] (page 5).
Schmidt, Brian P. et al. (Nov. 1998). In: ApJ 507.1, pp. 46–63.
arXiv: astro-ph/9805200 [astro-ph] (page 9).
Schoenholz, Samuel S. and Ekin D. Cubuk (Dec. 2019).
In: *arXiv e-prints*, arXiv:1912.04232, arXiv:1912.04232.
arXiv: 1912.04232 [physics.comp-ph] (pages 97, 120).
Scolnic, D. M. et al. (June 2018). In: ApJ 859.2, 101, p. 101.
arXiv: 1710.00845 [astro-ph.CO] (pages ix, 10, 20).
Scoville, N. et al. (Sept. 2007). In: ApJS 172.1, pp. 1–8.
arXiv: astro-ph/0612305 [astro-ph] (page 87).
Secco, L. F. et al. (Jan. 2022). In: Phys. Rev. D 105.2, 023515, p. 023515.
arXiv: 2105.13544 [astro-ph.CO] (pages xv, 26).
Sheldon, Erin S. and Eric M. Huff (May 2017). In: ApJ 841.1, 24, p. 24.
arXiv: 1702.02601 [astro-ph.CO] (page 64).
Sheldon, Erin S. et al. (Oct. 2020). In: ApJ 902.2, 138, p. 138.
arXiv: 1911.02505 [astro-ph.CO] (page 58).
Slipher, V. M. (Jan. 1914). In: *Lowell Observatory Bulletin* 2, pp. 66–66 (page 44).
Soldner, J. (Jan. 1921). In: *Annalen der Physik* 370.15, pp. 593–604 (page 30).
Soucail, G. et al. (Jan. 1987). In: A&A 172, pp. L14–L16 (page 31).
Spergel, D. N. et al. (June 2007). In: ApJS 170.2, pp. 377–408.
arXiv: astro-ph/0603449 [astro-ph] (page 6).
Sugiura, N., N. Sugiyama, and M. Sasaki (Jan. 1999).
In: *Cosmological Parameters and the Evolution of the Universe*.
Ed. by Katsuhiko Sato. Vol. 183. IAU Symposium, p. 269 (page 7).
Sugiyama, Sunao et al. (Dec. 2023). In: Phys. Rev. D 108.12, 123521, p. 123521.
arXiv: 2304.00705 [astro-ph.CO] (pages xv, 26).
Tisserand, P. et al. (July 2007). In: A&A 469.2, pp. 387–404.
arXiv: astro-ph/0607207 [astro-ph] (page 16).
Touboul, Pierre et al. (Sept. 2022). In: Phys. Rev. Lett. 129.12, 121102, p. 121102.
arXiv: 2209.15487 [gr-qc] (page 3).
Troxel, M. A. et al. (Aug. 2018). In: Phys. Rev. D 98.4, 043528, p. 043528.
arXiv: 1708.01538 [astro-ph.CO] (pages xv, 26, 33).
Tyson, J. A. (1990). In: *Gravitational Lensing*.
Ed. by Yannick Mellier, Bernard Fort, and Genevieve Soucail. Vol. 360, p. 230
(page 33).
Van Waerbeke, L. et al. (June 2000). In: A&A 358, pp. 30–44.
arXiv: astro-ph/0002500 [astro-ph] (pages 33, 64).
Voigt, L. M. and S. L. Bridle (May 2010). In: MNRAS 404.1, pp. 458–467.
arXiv: 0905.4801 [astro-ph.CO] (page 62).

Weinberg, Steven (1972) (page 3).
Wittman, David M. et al. (May 2000). In: Nature 405.6783, pp. 143–148.
arXiv: astro-ph/0003014 [astro-ph] (page 33).
Wyithe, J. Stuart B., Joshua N. Winn, and David Rusin (Jan. 2003).
In: ApJ 583.1, pp. 58–66. arXiv: astro-ph/0208532 [astro-ph] (page 40).
Zuntz, J. et al. (Nov. 2018). In: MNRAS 481.1, pp. 1149–1182.
arXiv: 1708.01533 [astro-ph.CO] (page 79).
Zwicky, F. (Jan. 1933). In: *Helvetica Physica Acta* 6, pp. 110–127 (pages 15, 46).
— (Feb. 1937). In: *Physical Review* 51.4, pp. 290–290 (page 31).

Appendices

A

Equivalence between adaptive moments and model fitting

We mentioned in section 4.1 that adaptive moments are mathematically equivalent to finding an elliptical Gaussian giving the best least-squares unweighted fit of the galaxy image. Here we will develop the mathematical proof for this equivalence.

The least-squares are expressed via the χ^2 :

$$\chi^2 = \sum_p \left(I - fe^{-\frac{1}{2}X^T M^{-1} X}\right)^2 \tag{A.1}$$

where I is the galaxy image, f the flux, X the pixel coordinates (equal to $x - x_0$) and M the elliptical Gaussian second moments we have to fit. We sum over the pixels p. The flux is defined as follows :

$$f = \sum_p W_p I_p \tag{A.2}$$

We define W as :

$$W(X) = e^{-\frac{1}{2}X^T M^{-1} X} \tag{A.3}$$

To find the best least-squares, we need to minimize $\partial\chi^2/\partial M^{-1}$:

$$\frac{\partial \chi^2}{\partial M^{-1}} = -\frac{f}{2} X^T X W \left(I - fW\right) = 0 \tag{A.4}$$

So we need to find W that satisfies :

$$x_0 = \frac{1}{f} \sum_p x W_p I_p \tag{A.5}$$

and :

$$\begin{aligned} \sum_p X^T X W_p I_p &= f \sum_p X^T X W_p^2 \\ M &= \frac{2}{f} \sum_p X^T X W_p I_p \end{aligned} \tag{A.6}$$

by posing $\sum_p X^T X W_p^2 = M/2$ (which is true for a well-sampled image).
This is exactly the same result as the one defined in the adaptive moments method (see Hirata and Seljak (2003)).

This solution was appreciated for its simplicity and ease of convergence, given reasonable assumptions on flux, centroid and moments values. It converges very quickly (less than a millisecond) for well-sampled images.
This moments' measurement method is also the one implemented in *Galsim*.

B

Optimal weight function size

In section 4.1.2, we introduced the importance of choosing the optimal weight function in our second moments formalism. This weight function is introduced to optimize the measurements at low SNR, avoiding infinite variance from divergent noise.
Here we detail the calculation of the optimal weight function for a round galaxy without seeing. A slightly different proof is provided in BJ02.

We define the image I as a function of $r^2 = x^2 + y^2$:

$$I(x, y) = f(r^2) \tag{B.1}$$

The shear matrix that defines the distortion applied on a galaxy (in other words to its coordinates system) is written :

$$S = \begin{pmatrix} 1+\gamma_1 & \gamma_2 \\ \gamma_2 & 1-\gamma_1 \end{pmatrix} \tag{B.2}$$

where γ_1 and γ_2 are the cosmic shear parameters. Its derivative with respect to γ_1 is therefore :

$$\frac{dS}{d\gamma_1} = \begin{pmatrix} 1 & 0 \\ 0 & -1 \end{pmatrix} \tag{B.3}$$

By defining :

$$\nabla I = \begin{pmatrix} \partial r^2/\partial x \\ \partial r^2/\partial y \end{pmatrix} f'(r^2) = 2 \begin{pmatrix} x \\ y \end{pmatrix} f'(r^2) \tag{B.4}$$

we can then write the derivative of $I(S, X)$ (the distorted image) with respect to γ_1 :

$$\begin{aligned} \frac{d}{d\gamma_1} I(S(\gamma_1), X) &= \left(\frac{dS}{d\gamma_1} X\right)^T . \nabla I \\ &= 2 \begin{pmatrix} x \\ y \end{pmatrix}^T \begin{pmatrix} x \\ y \end{pmatrix} f'(r^2) \\ &= 2(x^2 - y^2) f(r^2) \end{aligned} \tag{B.5}$$

We define M_1 as $M_{xx} - M_{yy}$ (equivalent to e_1) :

$$M_1 = \int (x^2 - y^2) W(x) I(x) d^2X \tag{B.6}$$

The derivative of M_1 with respect to γ_1 leads to :

$$\frac{\partial M_1}{\partial \gamma_1} = 2 \int (x^2 - y^2) W(x) (x^2 - y^2) f'(x^2 + y^2) dxdy \tag{B.7}$$

Because γ_1 is small, we can write the first term of M_1's Taylor expansion :

$$\begin{aligned} M_1 &\simeq \frac{\partial M_1}{\partial \gamma_1} \gamma_1 \\ &= 2\gamma_1 \int (x^2 - y^2)^2 W(x) f'(r^2) dxdy \end{aligned} \tag{B.8}$$

By posing the variance of I : $V(I) = n$, we can calculate the variance of M_1 :

$$V(M_1) = n \int (x^2 - y^2)^2 W^2(x) dx \tag{B.9}$$

Now we want to maximise $M_1/\sigma(M_1)$ with respect to W (with $\sigma(M_1)$ the standard deviation of M_1).
We define :

$$\begin{aligned} k_1(x) &\equiv (x^2 - y^2) W(x) \\ k_2(x) &\equiv (x^2 - y^2) f'(r^2) \end{aligned} \tag{B.10}$$

We then have :

$$\begin{aligned} M_1 &\propto \int k_1 k_2 \\ V(M_1) &\propto \int k_1^2 \end{aligned} \tag{B.11}$$

By invoking the Cauchy-Schwarz inequality, we find :

$$\int k_1 k_2 \leq \sqrt{\int k_1 k_2} \sqrt{\int k_1 k_2} \tag{B.12}$$

with equality if $k_1 \propto k_2$.
Thus, the maximum of $M_1/\sigma(M_1)$ is reached for $W \propto f'$.

If $f(r^2)$ is a Gaussian, it is proportional to an exponential, and so is $f'(r^2)$. In other words, we therefore have : $W(r^2) \propto f(r^2)$.

We can do the same analysis for M_2 (i.e. e_2), which is only sensitive to γ_2 in case of a round image. The optimization of M_2 with respect to γ_2 is obtained in the same way as above, by replacing the factors $(x^2 - y^2)$ by (xy). This leads to the same conclusion : $W \propto f$.

C

Full noise-free shear estimations

In this appendix, all the shear estimations performed on Gaussian, Sersic, Bulge+Disk and *COSMOS* galaxies for different TR values and galaxy profiles parameters are shown.

The conditions are similar to the ones detailed in chapter 5 : the PSF and W FWHM are fixed at 0.8 and 1.0 arcsec respectively, we look at random shear values between -0.03 and 0.03, and we average over 20 random (and opposite) pairs of intrinsic ellipticities from -0.3 to 0.3.

We see that at all TR, the multiplicative bias is limited at 0.5×10^{-3} for the Gaussian - Gaussian combination (see figure C.1). For Gaussian - Kolmogorov, the limit of $m \leq 10^{-3}$ is reached for TR=1.3 (see figure C.2). Finally, this limit is reached at TR=1.38 for Gaussian - Moffat (see figure C.3).

For the Sersic profiles, we only performed estimations with a Moffat PSF (which is the more realistic profile). When the Sersic index is $n = 1$ (i.e. exponential profile), we reach $m \leq 10^{-3}$ for TR=1.48 (see figure C.4). For $n = 1.5$, the limit is reached for TR=1.52 (see figure C.5), and for $n = 4$ (i.e. de Vaucouleurs profile) TR=1.6 (see figure C.6). Although all estimations made on Sersic profiles are quite acceptable, the progressive shift of the limit in TR as a function of the Sersic index argues for implementing a SSB correction that takes PSF profile into account, or performing analytical derivatives of second moments with respect to the shear in order to free ourselves from the SSB (and its dependence on the PSF model).

Other composite (bulge+disk) profiles have been tested, with different Sersic index values and disk half-light radius. We see that for a fixed n for the bulge, the estimations become better if the disk has a larger R_H (see figure C.7). All the estimations were performed with a Gaussian PSF.

Finally, we performed shear estimations on other *COSMOS* images than the one shown in 5.2.3. Here we only show estimates with a TR for which the limit on m is satisfied. We see that once again, $m \leq 10^{-3}$ is obtained at TR values around 1.6 (see figures C.8 and C.9), and we need to go to 1.82 for the last profile (see figure C.10).

C.1 Gaussian galaxies

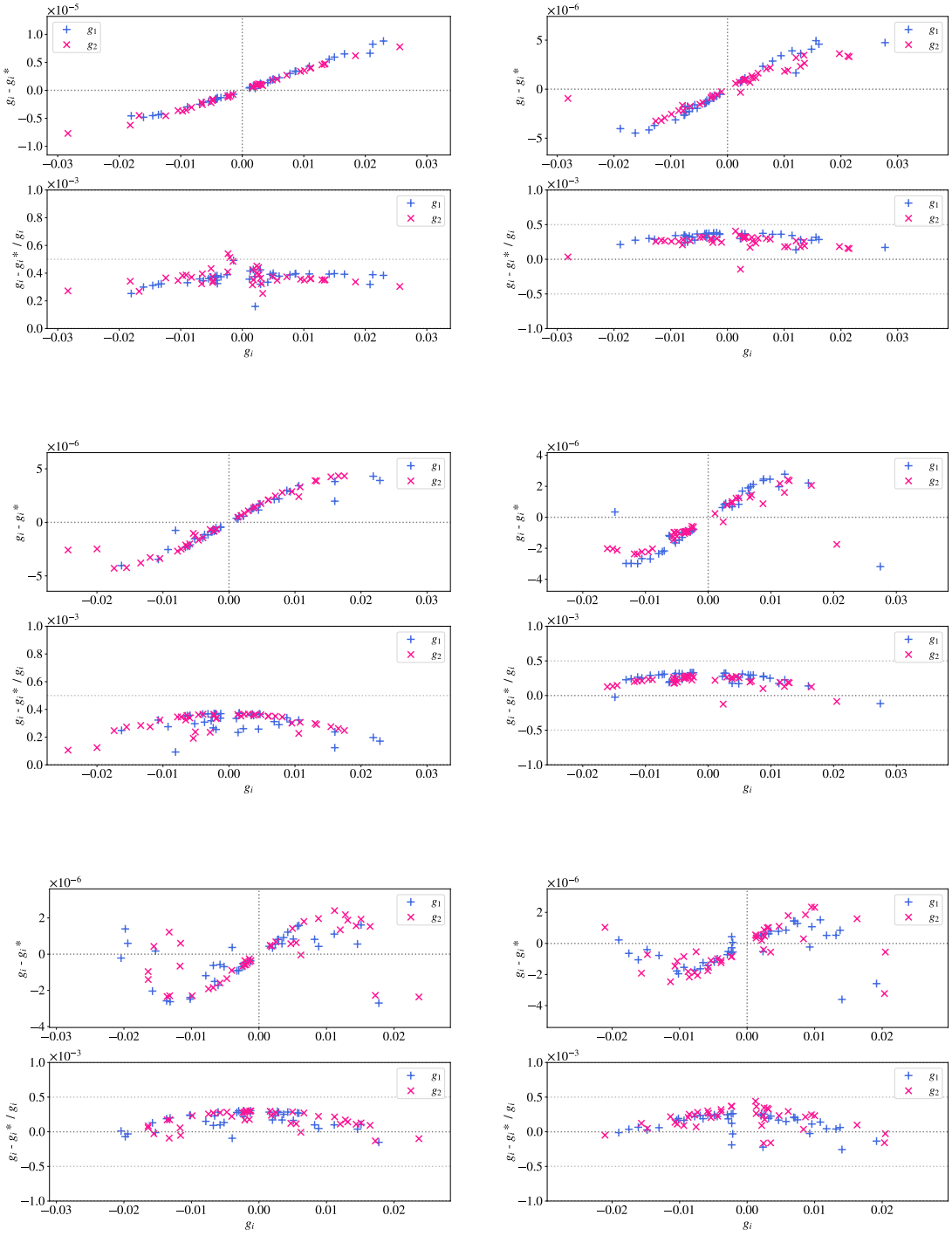

Figure C.1: *Gaussian galaxies - Gaussian PSF*
TR = [1.27 ; 1.56]

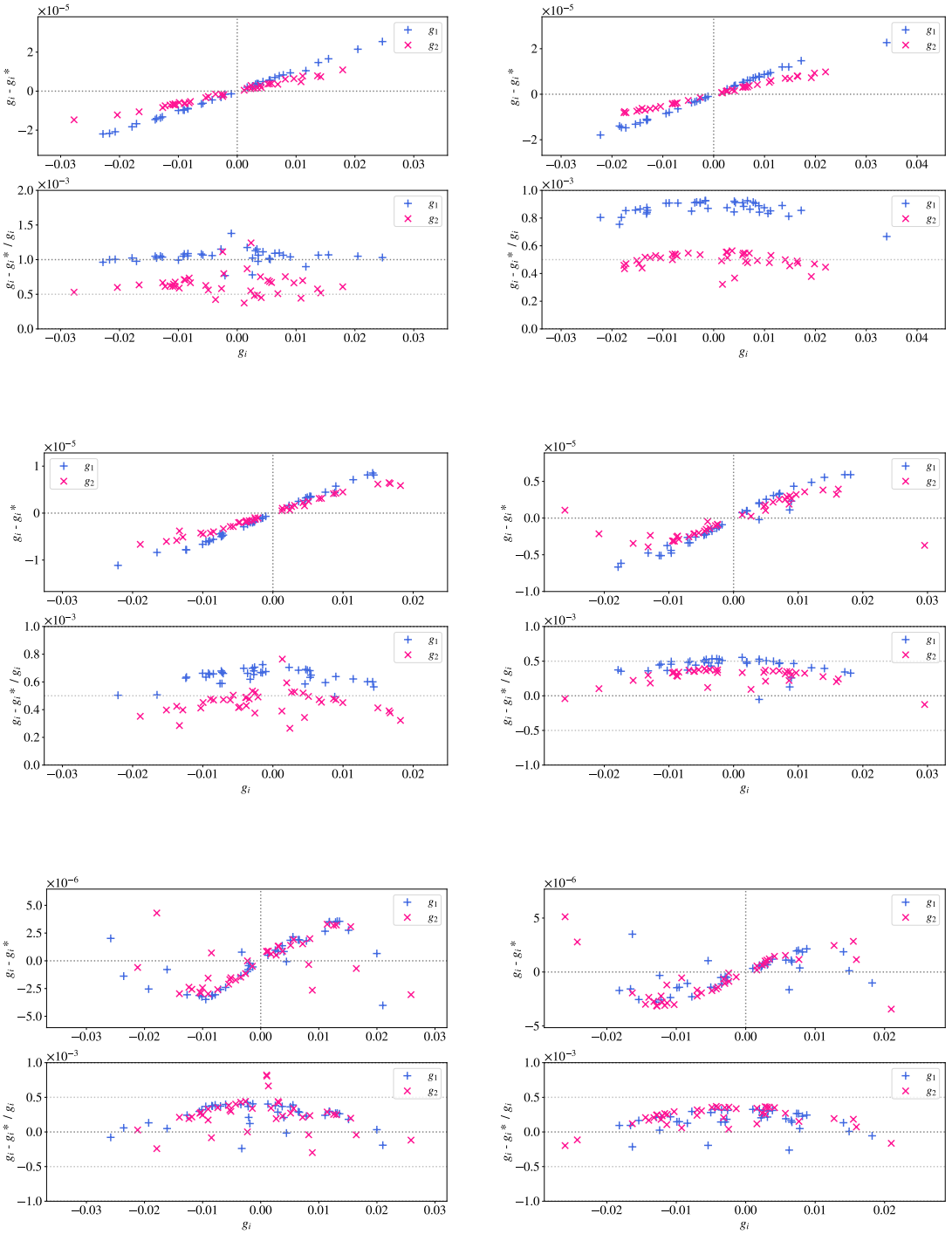

Figure C.2: *Gaussian galaxies - Kolmogorov PSF*
TR = [1.27 ; 1.57]

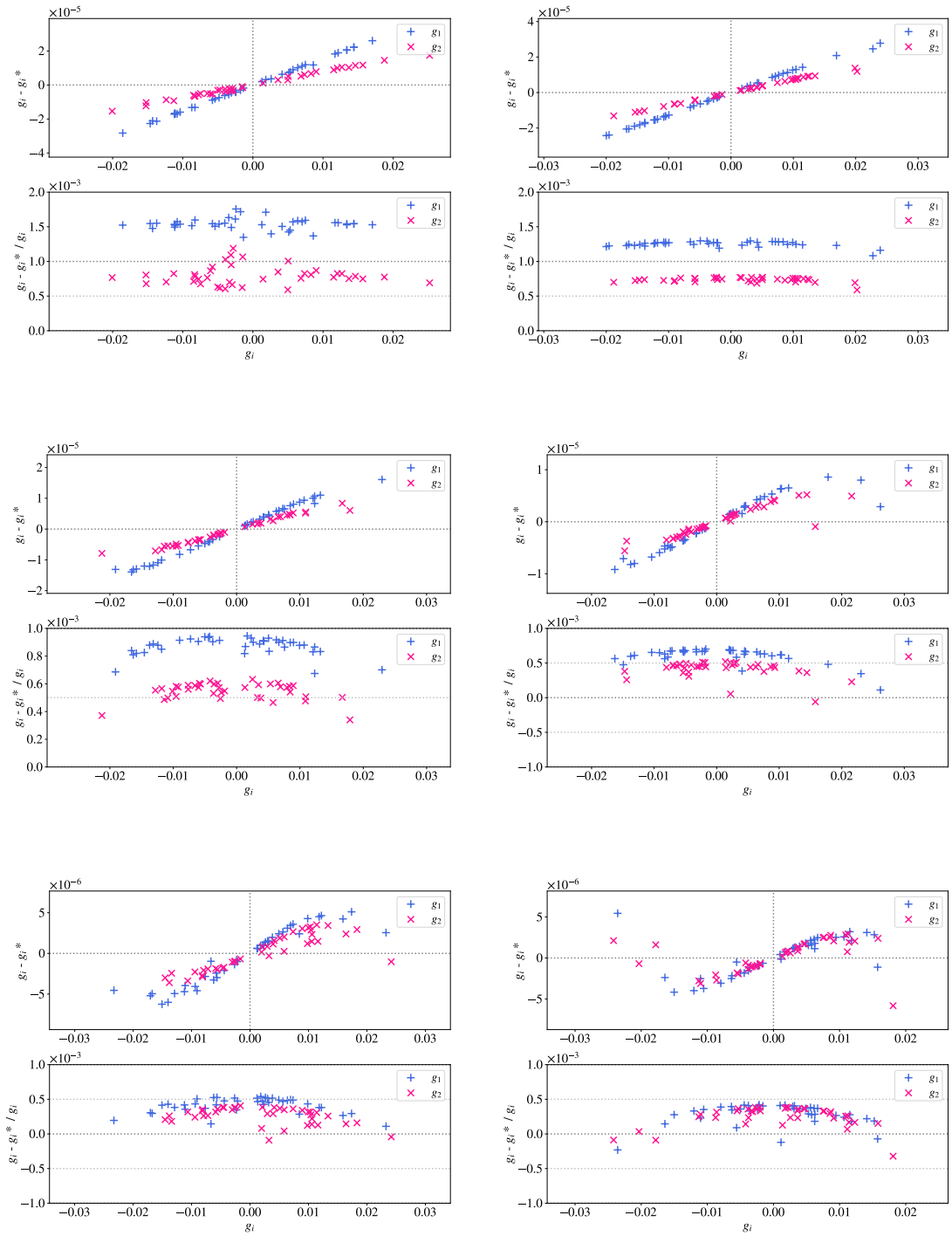

Figure C.3: *Gaussian galaxies - Moffat PSF*
TR = [1.28 ; 1.58]

C.2 Sersic galaxies

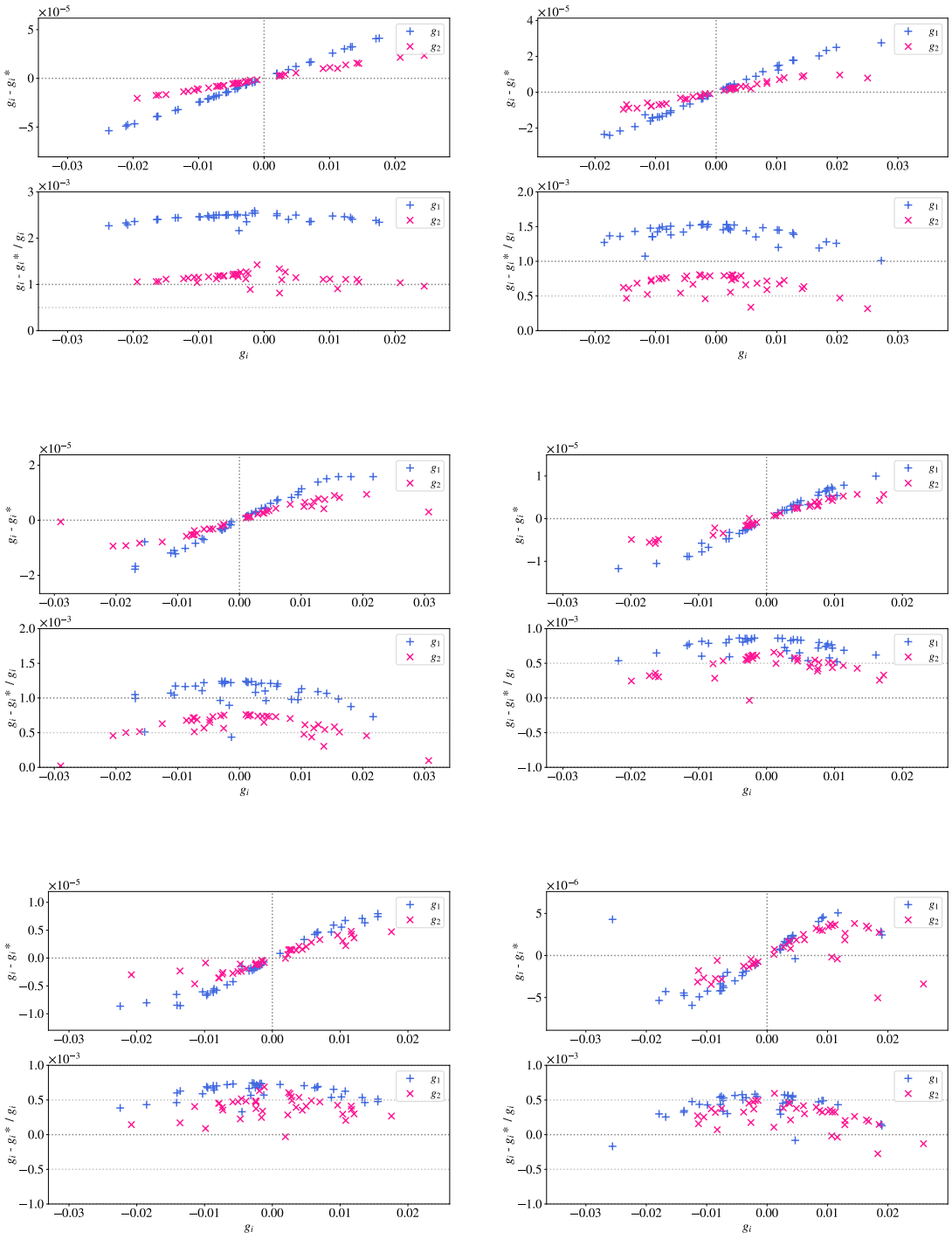

Figure C.4: *Sersic (n=1) galaxies - Moffat PSF*
TR = [1.25 ; 1.64]

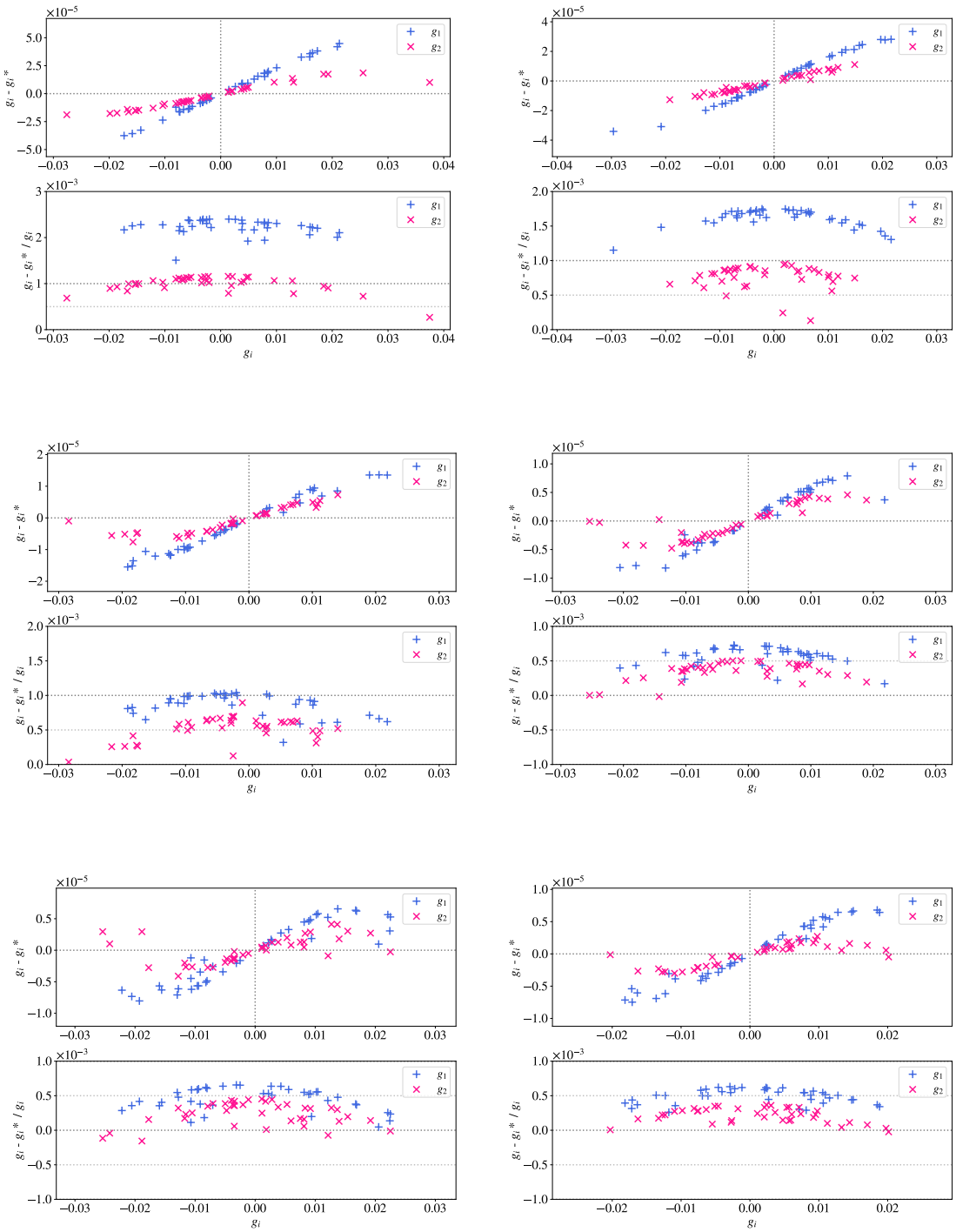

Figure C.5: *Sersic (n=1.5) galaxies - Moffat PSF*
TR = [1.3 ; 1.73]

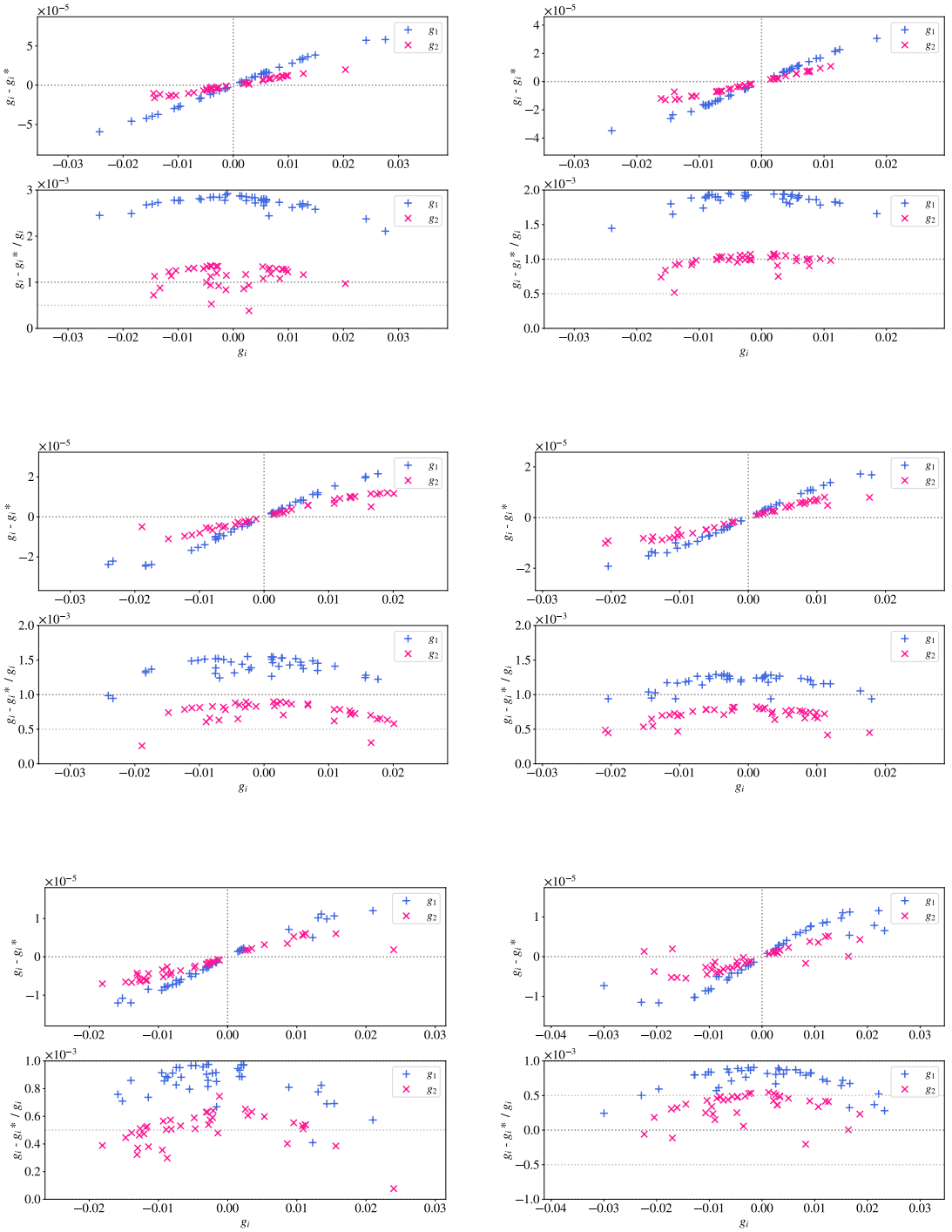

Figure C.6: *Sersic (n=4) galaxies - Moffat PSF*
TR = [1.34 ; 1.68]

C.3 Bulge + Disk galaxies

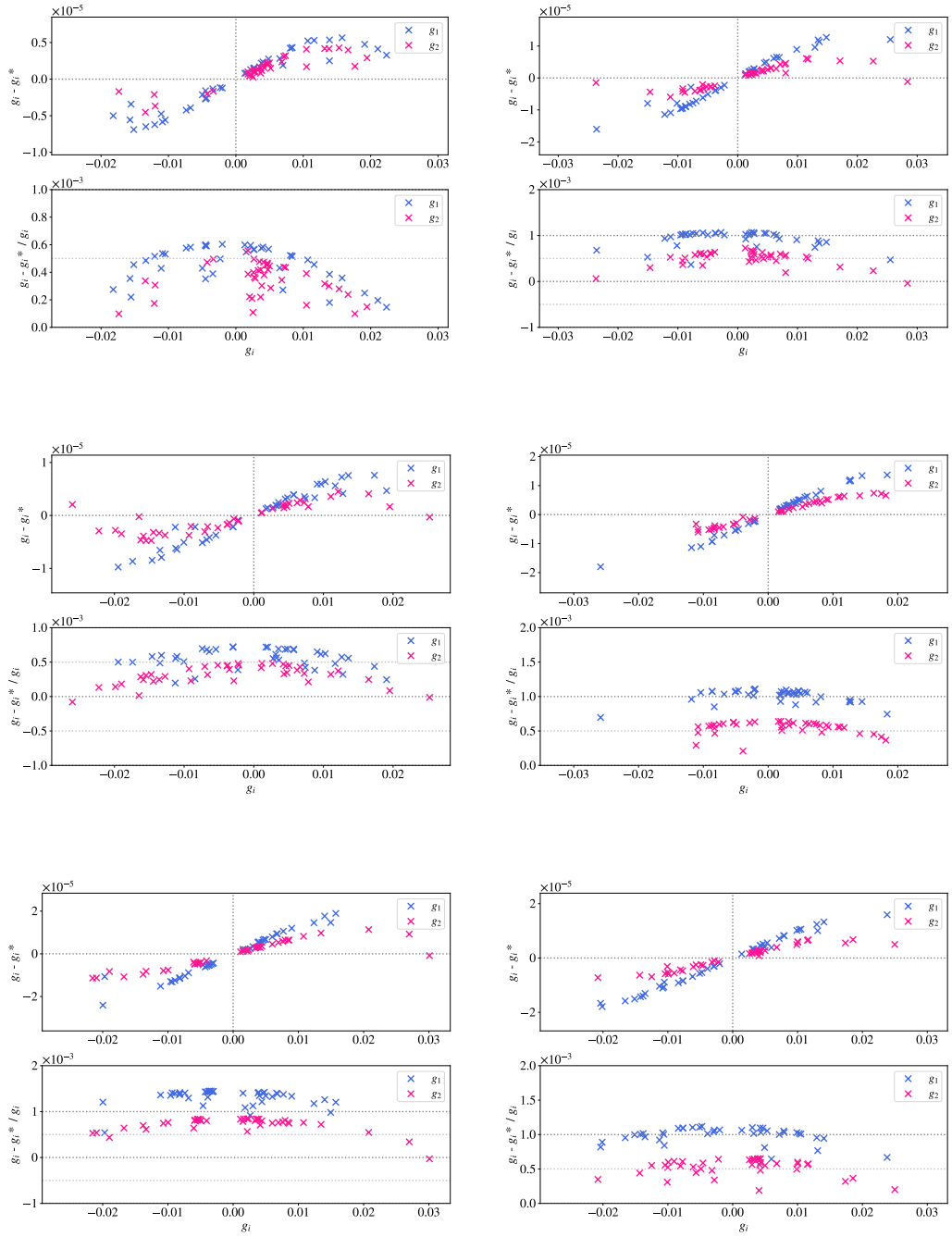

Figure C.7: *Bulge + disk galaxies - Gaussian PSF*
(a). bulge : $n = 1$, disk : $R_H = 0.8$, $TR = 1.57$
(b). bulge : $n = 2$, disk : $R_H = 0.8$, $TR = 1.5$
(c). bulge : $n = 2$, disk : $R_H = 1.6$, $TR = 1.63$
(d). bulge : $n = 3$, disk : $R_H = 1.4$, $TR = 1.55$
(e). bulge : $n = 4$, disk : $R_H = 1.4$, $TR = 1.5$
(f). bulge : $n = 4$, disk : $R_H = 1.6$, $TR = 1.57$

C.4 Cosmos galaxies

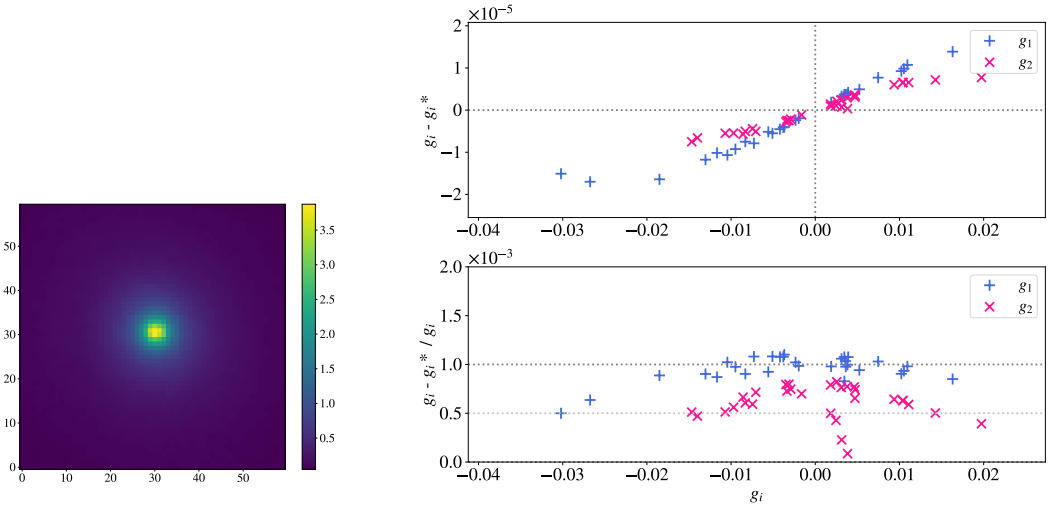

Figure C.8: *Left panel : COSMOS galaxy n°24966*
Right panel : Estimation with Gaussian PSF (TR=1.57)

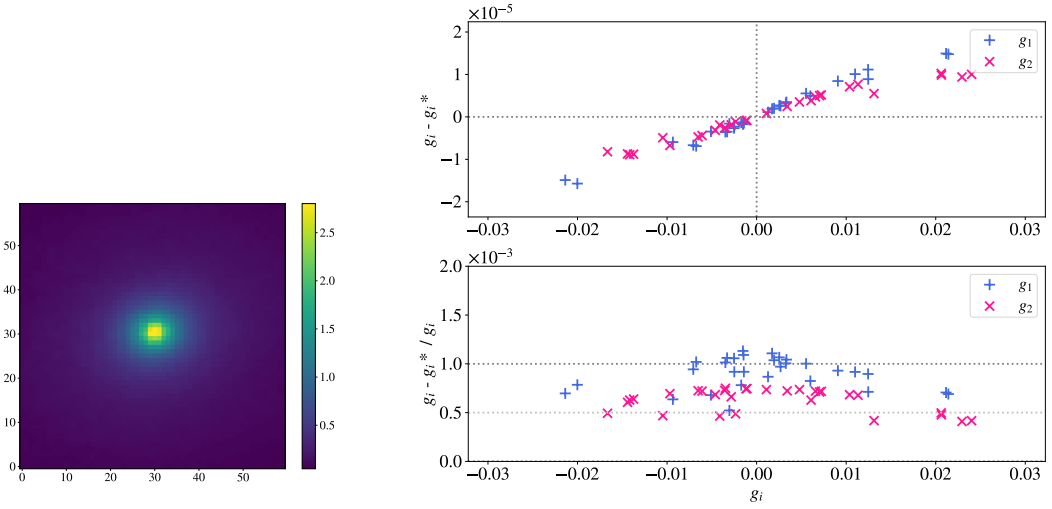

Figure C.9: *Left panel : COSMOS galaxy n°18884*
Right panel : Estimation with Gaussian PSF (TR=1.62)

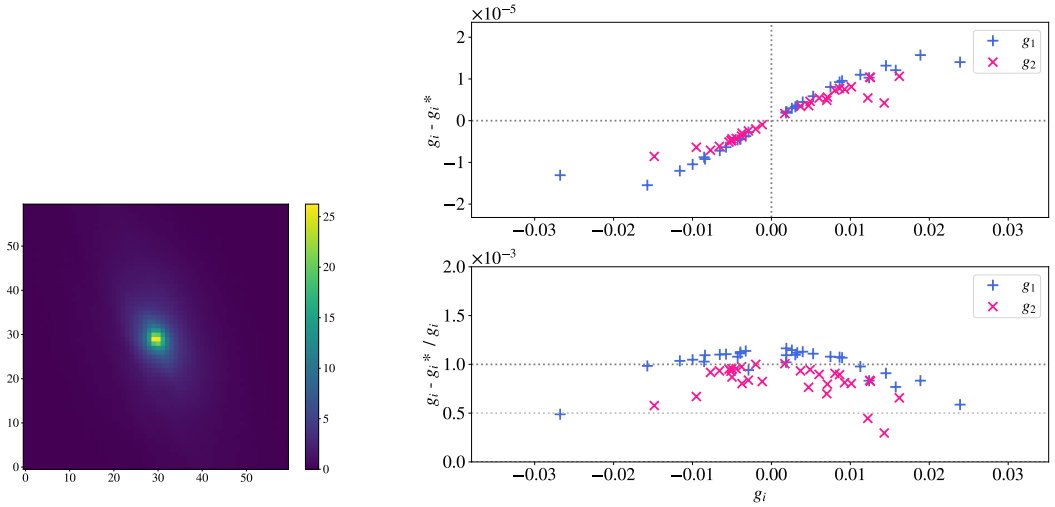

Figure C.10: *Left panel : COSMOS galaxy n°25630*
Right panel : Estimation with Gaussian PSF (TR=1.82)